Electromechanical Wave Imaging

Jean Provost

Submitted in partial fulfillment of the
requirements for the degree of
Doctor of Philosophy
in the Graduate School of Arts and Science

COLUMBIA UNIVERSITY
2012

ABSTRACT

Electromechanical Wave Imaging

Jean Provost

Cardiac conduction abnormalities and arrhythmias are associated with stroke, heart failure, and sudden cardiac death, and remain a major cause of death and disability. However, the imaging tools currently available to the physician to guide these treatments by mapping the activation sequence of the heart are invasive, ionizing, time-consuming, and costly.

In this dissertation, Electromechanical Wave Imaging (EWI) is described with an aim to characterize normal and abnormal rhythms noninvasively, transmurally, at the point of care, and in real time. More specifically, the methods to map the electromechanical wave (EW), i.e., the transient deformations occurring in response to the electrical activation of the heart, are developed and optimized. The correlation between EW and the electrical activation sequence during both normal and abnormal rhythms is demonstrated in canines *in vivo* and *in silico*. Finally, EWI is shown to noninvasively detect and characterize arrhythmias and conduction disorders in humans.

Novel ultrasound imaging methodologies were developed to track the EW. Radio-frequency (RF) frames acquired at high frame rates were used in conjunction with cross-correlation algorithms to map the onset of the small, localized, transient deformations resulting from the electrical activation and forming the EW. To validate the capability of the EW to characterize

cardiac rhythm, it was compared against the electrical activation *in vivo* and *in silico*. A high correlation between the electrical and electromechanical activations was obtained in normal canines *in vivo* during various pacing schemes and sinus rhythm. An *in vivo*-*in silico* framework was also developed to demonstrate that this correlation is maintained transmurally and independently of the imaging angle. EWI was also validated in abnormal canine hearts *in vivo* during ischemia, left bundle branch block, or atrio-ventricular dissociation.

In a clinical feasibility study, we demonstrated that EWI was capable of noninvasively mapping normal and abnormal activation patterns in all four cardiac chambers of human subjects using a readily available clinical ultrasound scanner. Specifically, EWI maps were generated for three heart failure patients with cardiac resynchronization therapy (CRT) devices and for three patients with atrial flutter who subsequently underwent catheter mapping and radiofrequency ablation. Preliminary validation of EWI maps against invasive transcutaneous electroanatomical cardiac mapping was also demonstrated.

EWI has the potential of becoming a noninvasive and highly translational technology that can serve as a unique imaging tool for the early detection, diagnosis and treatment monitoring and follow-up of arrhythmias and conduction disorders through ultrasound-based mapping of the transmural electromechanical activation sequence reliably, at the point of care, and in real time.

Table of Contents

List of Figures

segmented manually). Axial incremental strains are then estimated and overlaid onto the B-mode images to produce the EWI ciné-loop. (c) EWI isochrones are obtained by mapping the local zero-crossing time of the strains. (d) Bi-plane representations of the EWI ciné-loop can then be generated by synchronizing (using the ECG) and combining both views. The example shown here is from a 23-year old male healthy volunteer. (e) EWI isochrones are finally obtained by mapping the first zero-crossing time of incremental strains following the onset of the P-wave (in the atria) or the onset of the QRS (ventricles). The EW originates in the right atrium and propagates towards the left atrium during the P-wave of the ECG. In the ventricles, activation originates from multiple endocardial breaking points located, for instance, at the mid-septum and mid-anterior-wall, near the right-ventricular apex and near the base on the lateral wall. . 133

Figure 7-2 EWI isochrones of three normal subjects (a-c) The atrial activation sequence originates from the RA and propagates in the LA. In the two chamber view, propagation from the top of the LA is observed. In the ventricles, arrows indicate the sites of early activation, located in the septum at the mid-level, in the anterior wall near the base and in the posterior wall near the apex. (d-e) EWI isochrones of the normal subject (a) in the two and four-chamber views with different colorbars to highlight the atrial and ventricular activation sequences. The atrial activation sequence originates from the RA and propagates in the LA. In the two chamber view, propagation from the superior wall of the LA is observed. In the ventricles, arrows indicate the sites of early activation, located in the septum at the mid-level, in the anterior wall near the base and in the posterior wall near the apex, in the left ventricle, and near the apex of the right

List of Tables

List of Acronyms

ACT: Automated composite technique

AF: Atrial fibrillation

BB: Barankin bound

CRLB: Cramér-Rao lower bound

ECG: Electrocardiogram

ECGI: Electrocardiographic Imaging

EW: Electromechanical wave

EWI: Electromechanical Wave Imaging

LA: Left atrium

LAD: left anterior descending

LBBB: left bundle branch block

LV: Left ventricle

LVa: Left-ventricular, apical

LVar: Left-ventricular, apical region

LVb: Left-ventricular, basal region of the lateral wall

MRI: Magnetic Resonance Imaging

pdf: probability density function

PVC: Premature ventricular contractions

RA: Right atrium

RBBB: right bundle branch block

RF: Radio-frequency

RV: Right ventricle

RVa: Right-ventricular, apex

SNR_e: Elastographic signal-to-noise ratio

SRI: Strain Rate Imaging

TGC: Time gain compensation

TUAS: Temporally-unequispaced acquisition sequence

WPW: Wolff-Parkinson-White syndrome

ZZLB: Ziv-Zakai lower bound

Note: When the word ‘strain’ is used alone, it refers to axial incremental strain.

Acknowledgements

I had a tremendous time working toward this dissertation, and the discussions, debates, collaborations, arguments, and disagreements were the most enjoyable part of it. I would like to thank the many great people I had the opportunity and pleasure to work with over the years.

First and foremost, I would like to thank my advisor, Prof. Elisa Konofagou, for letting me work on the most exciting project available (arguably). It was always possible to speak and argue freely – even vehemently – and have the pleasure of losing to her on the basis of scientific arguments alone. She has created a work environment with a healthy dose of positive pressure to channel the talents of everyone to do good science effectively. I hope I will be able, one day, to recreate such an environment.

This project required the skills of many people, who helped me out with various tasks, including writing algorithms, designing circuit boards, and programming ultrasound scanners to perform or simulate canine experiments and clinical studies. In no particular order I would like to thank Dr. Edward Ciaccio, Dr. Molly Flexman, Vu Thanh-Hieu Nguyen, Stanley Okrasinski, and Dr. Deepak Saluja for helping me design and build circuits and understand how to map the electrical activation of the heart; Dr. Eiichi Hyodo, Dr. Shinichi Iwata, and Dr. Yukiko Oe for gratefully helping me with the scanning of patients and dogs, with the greatly appreciated support of Dr. Shunichi Homma; Dr. Kana Fujikura, Dr. Alok Gambhir, Dr. John Vest, Dr. James Coromilas, and Dr. Hasan Garan for helping me design and conduct the clinical studies; Eugene Bobkov, Dr. Gerard Boink, Dr. Peter Danilo, Dr. Heather S. Duffy, Dr. Alexander Romanov, Dr.

Iryna N. Shlapakova, and Dr. Jie Wang, for their advice and help during animal experiments; Dr. Viatcheslav Gurev for conducting simulations; and Gaurav Agarwal, Diégo Legrand, Dr. Jianwen Luo, Kevin Mu, Vu Thanh-Hieu Nguyen, Stéphane Thiébaut, and Dr. Shougang Wang for helping with the programming of the ultrasound scanners and algorithms.

I would like to thank my dissertation committee, Dr. Andreas Hielscher, Dr. Gerard Ateshian, Dr. Natalia Trayanova, and Dr. Hasan Garan. I would like to thank especially Dr. Trayanova for having me into her lab at Johns Hopkins on my first day, and for helping me throughout with questions concerning the heart and simulations. I would also like to thank Dr. Garan for his inestimable help when the time came to try out my work in the clinic.

On a more personal level, I would like to mention how great it was to work with the always positive and patient Dr. Wei-Ning Lee and Dr. Kana Fujikura, the incredibly resourceful Stanley J. Okrasinski The Third, the encyclopedic Dr. Jianwen Luo, and the inexhaustible Dr. Alok Gambhir. Special thanks to Gaurav Agarwal, Donald Chang, Diégo Legrand, Kevin Mu, Vu Thanh-Hieu Nguyen, and Stéphane Thiébaut, who all did impressive work during their internships and contributed to this dissertation a lot more than they might think. Finally, I had the opportunity to work with Alexandre Costet, Ethan Bunting, and Dr. Julien Grondin, and would like to thank them for their help over the last few months.

I had the chance to share my experience with great co-workers and friends who made the daily life in the lab enjoyable. I'd like to mention them here: Jaimie Lee, Dr. Caroline Maleke, Dr.

James Choi, Dr. Yao-Sheng Tung, Yi Hou, Dr. Asawinee Danpinid, Babak Baseri, Dr. Thomas Deffieux, Dr. Fotis Vlachos, Gesthimani Samiotaki, Kirsten Selert, Viktor Gamarnik, Bharat Ramachandran, Jennifer Hui, Oluyemi Olumolade, Julio Herrera Estrada, Dr. Sacha Nandlall, Dr. Danial Shahmirzadi, Dr. Jiangang Chen, Ronny Li, Dr. Émilie Franceschini, Tianzhu Liang, Anna Wong, Dr. Cherry Chen, Dr. Shutao Wang, Shih-Ying Wu, Matthew Downs, Noé Jiménez, Nikhil Chandra, William Qaqish and, with special mention, Dr. Jonathan Vappou and Dr. Fabrice Marquet.

Finally, I would like to thank my parents, Hélène and Luc, my siblings, Marie-Jeanne and Marc, and Grace Kiser, for their love and support.

Dedication

À mes parents

Chapter 1 Introduction

1.1 Motivation

The heart is an electromechanical pump that must be first electrically activated under a specific sequence in order to contract efficiently. Cardiac muscle cells, or myocytes, fill the dual role of conducting action potentials and contracting in response to them. In the normal heart, the cumulative effect of the successive contraction of individual myocytes leads to the periodic global contraction and relaxation of the heart that drives the pulmonary and systemic circulations. Cardiac disease can stem from various causes, including inefficient electrical propagation patterns, corrupted electromechanical coupling mechanism, and insufficient contraction.

Electrical and electromechanical dysfunctions of the heart are among the greatest current healthcare challenges, both in terms of extent and quality of life and expenditure. Cardiac arrhythmias and conduction abnormalities have been linked to stroke (Wolf et al., 1991), heart failure (Carson et al., 2005) and sudden cardiac death (Zheng et al., 2001). Arrhythmias led to 881,000 hospital admissions in the United States in 2011 (Roger et al., 2011). Heart failure, a condition linked to dyssynchronous electrical activation of the ventricles and altered electromechanical coupling, is the leading cause of hospitalization in people older than 65 (Alla et al., 2007).

New therapies are being developed to treat and even cure these conditions. They are based on the modification of the electrical activation sequence and the electromechanical response of the heart via ablation, pacing, and drug therapies. However, no established imaging modality can noninvasively map the electrical activation sequence or the electromechanical activity of the heart, which is essential for accurate patient selection, monitoring and follow-up of

treatments and to further the understanding of conditions such as heart failure. The only noninvasive tool currently available to the physician is the 12-lead electrocardiogram (ECG), which provides information on the conduction and global activation properties of the heart. The 12-lead ECG does, however, have limitations in reliably determining the site of origin or specific underlying mechanism of arrhythmias. Detailed mapping of cardiac electrical activity during arrhythmias can be achieved with intracardiac electroanatomical mapping, a procedure that consists of introducing electrode-catheters into the heart chambers to obtain a series of local intracardiac electrograms. However, this approach is costly, time-consuming, ionizing, carries some degree of risk, and has limited utility for monitoring response to therapy over an extended period of time.

1.2 General Goal and Specific Aims

Electromechanical Wave Imaging (EWI) is an ultrasound-based imaging modality that maps the electromechanical wave (EW), i.e., the transient deformations occurring in response to the electrical activation. This dissertation aims at developing and optimizing EWI to map the electromechanics of the heart, demonstrating that the EW is closely correlated with the electrical activation and, finally, showing that EWI can be used to noninvasively detect and characterize arrhythmias and conduction disorders in humans. To achieve this goal, new ultrasound imaging methodologies were developed to track the EW, the relationship between the electrical activation and the EW was established in canine hearts *in silico* and *in vivo*, and several potential clinical applications of EWI were explored in patients with arrhythmia and heart failure. EWI has the potential to become a noninvasive and highly translational technology that can serve as a unique imaging tool for the early detection, diagnosis and

treatment monitoring and follow-up of arrhythmias and conduction disorders through ultrasound-based mapping of the transmural electromechanical activation sequence reliably and noninvasively, at the point of care and in real time. The **specific aims** are described as follows:

1) Develop novel imaging sequences and processing techniques to map the EW in a full view of the heart, with optimal accuracy, and at high temporal resolution and spatial resolution.

Hypothesis: EWI can be performed at high beam density and at high frame rate, over a large field of view.

Challenge: To circumvent the trade-off between temporal resolution, beam density and field of view in conventional ultrasound imaging.

Approach: Three different ultrasound imaging sequences were developed to map the EWI: automatic composite technique, temporally unequispaced acquisition sequence, and parallel beamforming.

Impact: These imaging sequences allowed clinical ultrasound scanners to resolve, both spatially and temporally, the EW for the first time.

2) Establish the relationship between the electromechanical wave and the electrical activation in canines *in silico* and *in vivo*, both in normal and diseased hearts.

Hypothesis: The EW is closely correlated to the electrical activation sequence and can be used as a surrogate for direct noninvasive measurement of electrical activation.

Challenge: To simultaneously measure the EW and the electrical activation sequence in large sections of the myocardium.

Approach: *In vivo* and *in silico* validation was undertaken in normal and abnormal canine hearts, first using a small number of sutured electrodes in one plane to limit imaging artifacts, then using a 64-electrodes basket catheter to increase resolution, and finally using an anatomically realistic, three-dimensional electromechanical simulation model of the canine heart.

Impact: The capability of EWI to characterize the electrical function of the heart was established.

3) Demonstrate that EWI can detect and characterize arrhythmias for treatment guidance in humans.

Hypothesis: The relationship between the EW and the electrical activation is maintained in normal and pathological human hearts and can be used for diagnosis, monitoring and follow-up treatment.

Challenge: To establish whether EWI can distinguish different types of arrhythmias.

Approach: EWI was performed in normal human subjects and in patients during sinus rhythm, left bundle branch block, cardiac resynchronization therapy, and atrial flutter. EWI maps were then compared with the location of pacing and ablation sites, and against cardiac mapping.

Impact: The completion of this aim established the clinical significance of EWI.

1.3 Overview and Significance

Achieving the specific aims described in the previous section led to significant contributions in ultrasound imaging, in physiology, and for the development of new clinical procedures. The first aim consists in developing novel imaging sequences and processing techniques to map the

EW in a full view of the heart, with optimal accuracy, and at high temporal and spatial resolutions. As of today, the transient deformations occurring during the isovolumetric phases of the cardiac cycle are poorly understood. By achieving higher frame rates it becomes possible to distinguish the effect of the electrical activation from the mechanical waves generated by the valves' activity. Novel empirical techniques to measure the elastographic signal-to-noise ratio (SNR_e) within a probabilistic framework were developed in order to determine the optimal frame rates for EWI. Higher frame rates were achieved using novel imaging strategies, including techniques based on diverging ultrasound beams emanating from a virtual 2-D point-source used in human hearts for the first time.

The second aim consists in establishing the relationship between the EW and the electrical activation. In order to perform such evaluation, the propagation of the EW needs to be compared to the 3-D electrical activation in the ventricles, preferably in a large animal heart, such as the canine one. Different approaches were developed to perform this comparison in this dissertation and used to show, for the first time, the correlation between the electrical and electromechanical activation in both normal and pathological canine hearts, *in vivo*. However, experimental methods suffer from imperfect co-registration and interference and do not allow for simultaneous mapping of both the EW and the transmural electrical activation sequence. Indeed, the spatial resolution of plunge needle recordings is insufficient for the adequate comparison with the EW sequence. More importantly, since the strains associated with the EW are minute, the insertion of needle electrodes is likely to significantly alter the normal EW. An anatomically realistic modeling approach to cardiac function was therefore used to obtain 3-D

electrical activation sequence in the ventricles, using a high-resolution dynamic model of coupled cardiac electromechanics in the canine heart developed by Dr. Trayanova's group (Gurev, Lee, et al., 2010). Our approach consisted in a reciprocity study, in which the information lacking from the model (i.e., the EW, pressure) was provided by *in vivo* experiment and the information that cannot be obtained experimentally (i.e., the 3-D transmural activation sequence) was provided by simulations. This resulted in a novel framework that can be used to test various hypotheses and further the understanding of the heart physiology (Zlochiver, 2011).

The third aim consisted in demonstrating that EWI can detect and characterize arrhythmias and conduction disorders for treatment guidance. Arrhythmias such as atrial flutters and conduction disorders such as left bundle branch block can now be treated, e.g., by neutralizing the arrhythmogenic zones through ablation or by resynchronizing the contraction of both ventricles through cardiac resynchronization therapy (CRT). While both ablation and biventricular pacing therapies are routinely used, they are yet to be fully understood and optimized, mostly because of the challenges associated with mapping the electrical activity of the heart. Over the past several decades, efforts have been aimed at the development of technologies to map the cardiac electrical activation. Minimally invasive procedures, in which a catheter containing one or several electrodes is inserted into the heart chambers, are now frequently used in the clinic. These clinical procedures are, however, limited to conditions where ablation therapy is indicated. Effectively, they are not used routinely for diagnosis or to optimize the lead placement and timings of pacing therapies. They are also limited to the

endocardium, hence requiring an additional procedure when the region to be ablated is located on the epicardium. EWI could constitute a pivotal alternative or complementary approach to those technologies, as it can be used in real time, at the point of care and can be easily integrated into existent ultrasound systems and current clinical protocols at no or low additional cost.

This dissertation is organized as follows: Chapter 2 covers the basics of cardiac physiology and imaging; Chapter 3 describes the basic concepts of ultrasound imaging and motion estimation used in EWI; Chapter 4 details three different EWI methods; Chapters 5 and 6 cover studies of the correlation between the electrical and electromechanical activation in both normal and pathological hearts, respectively; and Chapter 7 explores the clinical feasibility of EWI. Finally, Chapter 8 summarizes the dissertation and proposes avenues of future work.

Chapter 2 Cardiac Mechanics, Electrophysiology, and Electromechanics

2.1 Introduction

This chapter provides an overview of the concepts of anatomy and physiology necessary to understand the relationship between the electrical and mechanical functions of the heart, followed by a description of the imaging state of the art for the characterization of the cardiac mechanics, electrophysiology, and electromechanics.

2.2 Cardiac anatomy

The mammalian heart is composed of four chambers, i.e., the right and left atria (RA and LA, respectively), and the right and left ventricles (RV and LV, respectively) (**Figure 2-1**). The heart walls are composed of the endocardium (i.e., inner surface), the myocardium (i.e., middle layer), and the epicardium (i.e., outer layer). The myocardium is the major functional tissue layer to contract for the ejection action and is composed of cardiac muscle cells, or myocytes, arranged into fibers and embedded in an extracellular matrix. Individual myocytes, which are cells of irregular cylindrical shape 50 to 120 μm in length and 5 to 25 μm in diameter (Sachse, 2004), fill the dual role of conducting action potentials and contracting in response to them. More specifically, the electrical conduction in myocytes can be modeled by adapted versions of the Hodgkin-Huxley model of the squid axon (Hodgkin and Huxley, 1952; Noble, 1960), i.e., by modeling sodium, potassium, and other cell membrane ion channels and the propagation of action potential through gap junctions. The cardiac cell action potential has, however, unique characteristics due to the crucial role of the calcium channels that result, for example, in long action potentials, i.e., approximately 200-400 ms, in comparison with 1 ms for a neural action potential. More importantly, the calcium ion is the direct activator of myofilaments, which are chains of proteins found in the myocytes that cause contraction.

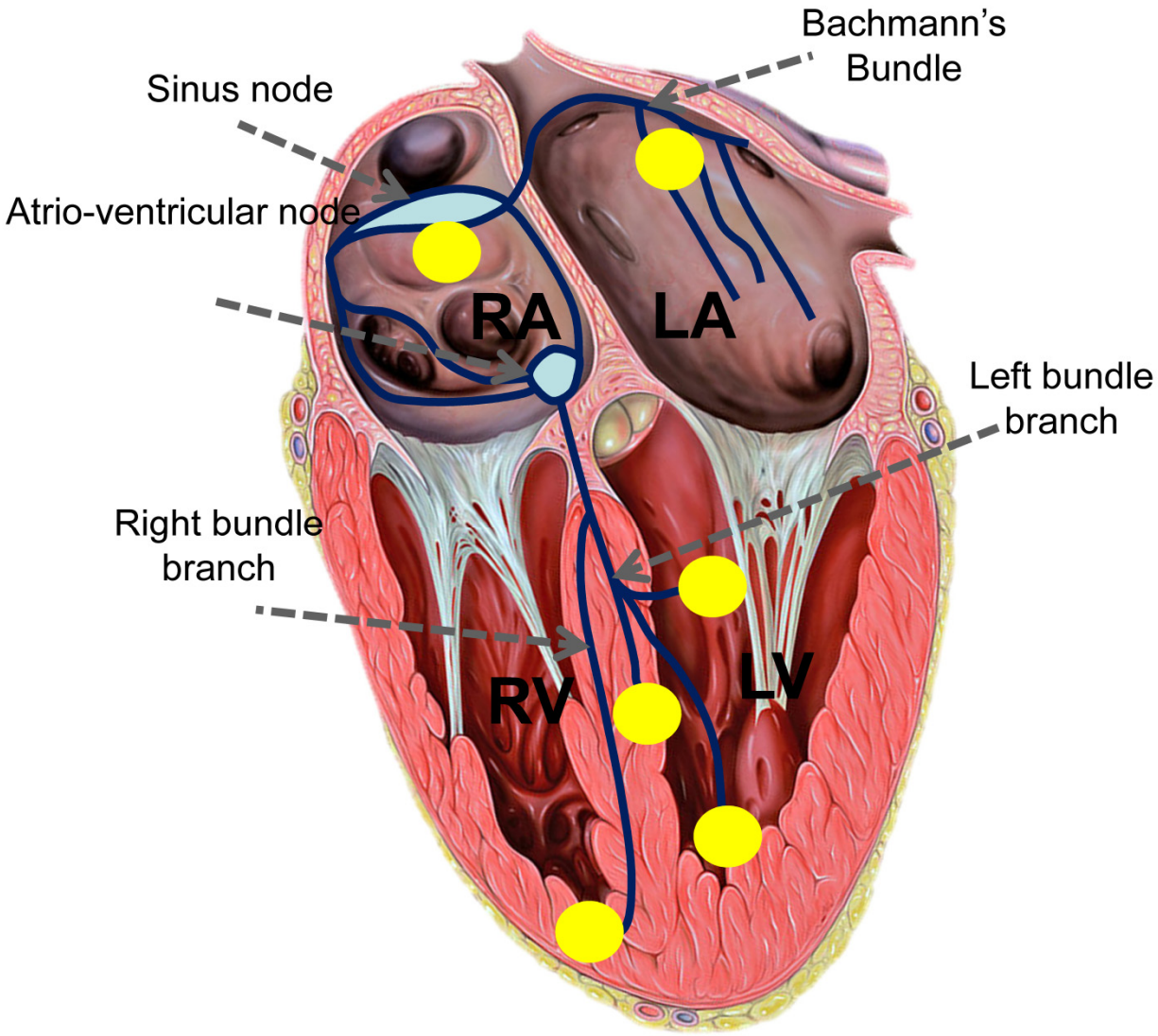

Figure 2-1 Specialized conduction system of the heart. Activation is initiated in the sinus node located in the right atrium and propagates in the left atrium via the Bachmann's bundle and towards the atrio-ventricular node. Conduction then reaches the ventricles via the left and right bundle branches. The left bundle branch splits into three fascicles in the anterior, posterior and septal walls of the left ventricle (Tawara, 1906). Yellow areas indicate regions of early myocardium activation (Durrer et al., 1970), following propagation in the specialized conduction system. Heart diagram source: Wikimedia.org.

Different types of myocytes exist, usually defined by their function (Sachse, 2004): for example, myocytes assigned to the working myocardium produce primarily mechanical tension while specialized myocytes have the task of initiating (pacemaker cells) and conducting action potentials. In the normal human heart, the initiator of the physiologic electrical excitation, i.e., the sinus node, is located in the RA at the orifice of the superior vena cava (Koch, 1909) and is formed of specialized myocytes that spontaneously generate action potentials. Note that other myocytes also display such automaticity. However, because the intrinsic rate of the sinus node myocytes is higher, they are considered latent, i.e., they take over the function of initiating excitation when the sinus node cannot produce impulses or when these impulses fail to propagate. The myocytes of the sinus node are connected via gap junctions to the myocytes of the atrial contracting myocardium. They are also connected to the atrioventricular node via the crista terminalis and to the left atrium via the Bachmann bundle, both of which are specialized conduction pathways. The atrioventricular node is connected to the bundle of His, which is insulated by sheaths of fibrous tissue and penetrates the heart skeleton between the atria and ventricles (Sachse, 2004). In the normal heart, action potentials can only traverse from the atria to the ventricles through the bundle of His. The bundle of His is the root of the Tawara bundle branches (Tawara, 1906), which are themselves connected to the Purkinje fibers. The Purkinje fibers are connected to the subendocardium of both ventricles. The electrical activation of the myocardium results, after an electromechanical delay of a few tens of milliseconds (Bers, 2002; Cordeiro et al., 2004) to the shortening of cells (**Figure 2-2**), and to the global contraction of the heart leading to blood ejection. The mechanical properties of the heart resulting from its anatomy and most importantly the arrangement of myocytes into fibers

can be complex. An important body of literature as reviewed in Hunter and Smaill (1988) allows us to approximate the heart as orthotropic, incompressible, non-linear, visco-elastic, and undergoing large deformations so that the infinitesimal strain theory applies only over short durations.

2.3 The heart cycle

2.3.1 Normal electrical activity

Three main electrical events are observed on the surface electrocardiogram (ECG) (**Figure 2-2**): the P-wave, the QRS complex and the T-wave. In the normal heart, action potentials are spontaneously generated by the sinus node located in the RA (onset of P-wave); propagate in the RA and subsequently in the LA via the Bachmann's bundle, which is connecting the superior walls of the right and left atria. Activation further propagates toward the inferior region of the RA and the anterolateral and posterior wall of the LA with the latest activated region being the posterolateral wall of the LA (Ponti et al., 2002; Kojodjojo et al., 2006). After propagating in the slow-conducting, atrio-ventricular node connecting the ventricles to the atria (PR segment), the action potentials enter the Tawara bundles and the Purkinje fiber network, which is a collection of fast-conducting specialized cells that connect at their terminals different endocardial regions of the ventricles that typically include an area high on the anterior paraseptal wall immediately below the mitral valve, and an area at half the distance from the apex to the base in the left side of the interventricular septum, and the posterior paraseptal area at approximately one third of the distance from apex to base (onset of the QRS complex) (Durrer et al., 1970; Cassidy et al., 1984).

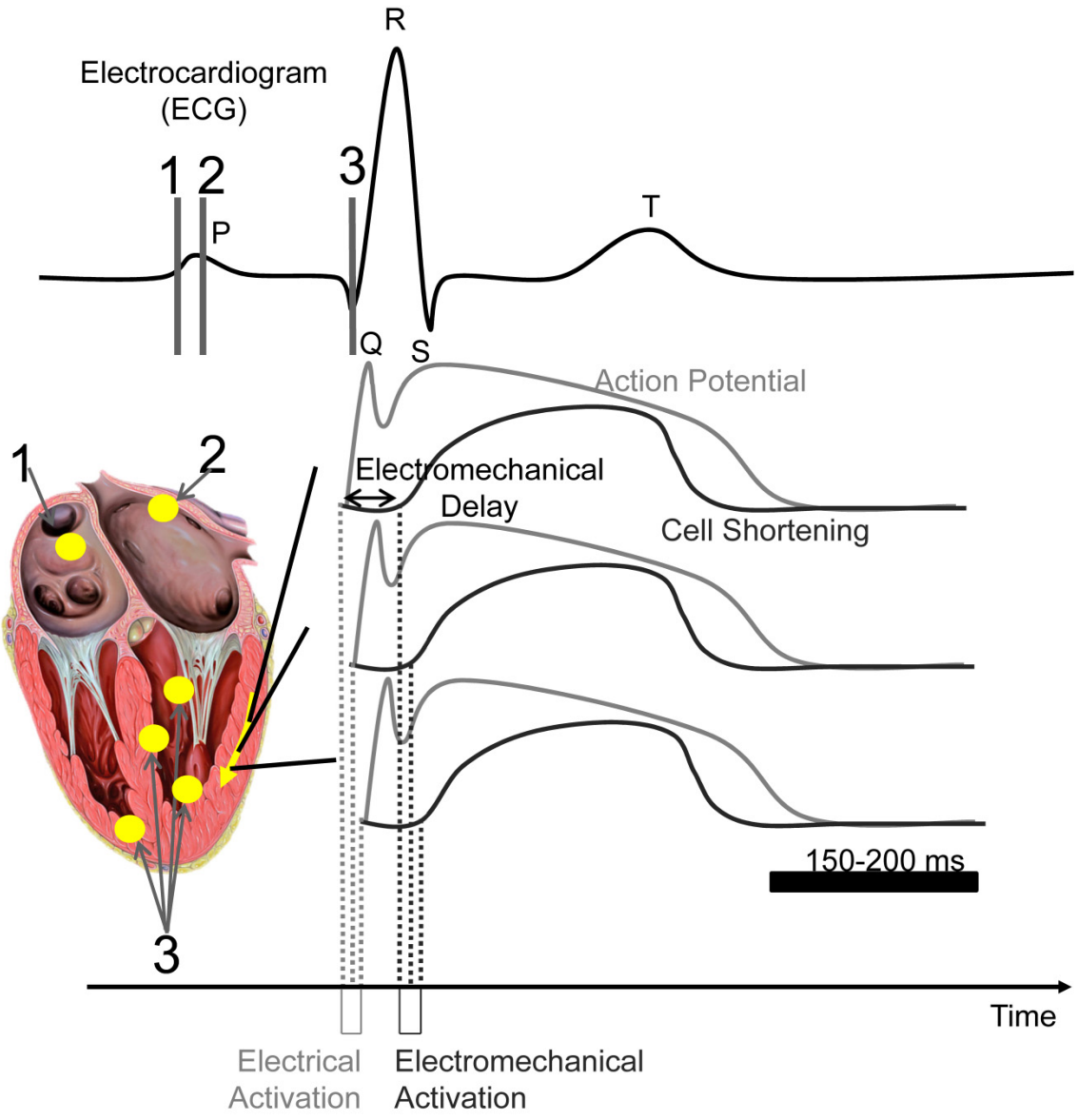

Figure 2-2 Schematic representation of the electrical activity of the heart and its electromechanical response. The surface ECG provides global information about the electrical activity; the normal electrical activation sequence is represented by three events marked on the ECG. At the microscopic level, cells in the myocardium undergo action potentials followed by cell shortening after the electromechanical delay, e.g., along a given propagation direction (yellow arrow). The propagation of the electrical and electromechanical activations is much shorter than the duration of an action potential and of the duration of the cardiac contraction.

Action potentials then propagate into the myocardium (QRS complex). The electromechanical activation, i.e., the onset of contraction, stems from the electrical activation and occurs in the cardiac muscle after an electromechanical delay of a few milliseconds (Bers, 2002; Cordeiro et

al., 2004). This activation leads to a rise in pressure which reaches a maximum approximately a few hundreds of milliseconds later. Following this maximum, the heart repolarizes (T-wave) and actively relaxes before becoming passive during diastole. The left ventricle is connected to the aorta and the left atrium via two valves, i.e., the aortic valve and the mitral valve, respectively. Immediately following (and in some cases during) the ventricular electrical activation (QRS complex), the mitral valve closes and the heart enters an isovolumetric phase during which the heart contracts but no blood is ejected, leading to an increase in pressure. When the left-ventricular pressure reaches the aortic pressure, the aortic valve opens, allowing the rapid ejection of the blood with continued left ventricular pressure increase followed by a decrease during the reduced ejection phase. When the aortic valve closes, diastole begins and the isovolumetric relaxation phase (repolarization) is initiated until the pressure in the left ventricle decreases below the left atrial pressure, which results in the opening of the mitral valve. The LV then enters the filling phase (Fuster and O'Rourke, 2008).

Note that while the electrical and mechanical activity of one cell occurs over 300-400 ms, the spatial propagation from cell to cell of the onset of these electrical and mechanical activities occurs much faster: e.g., 60 ms are necessary to activate the entire left ventricle while its contraction occurs over 300-400 ms. Imaging the mechanical activity thus requires lower frame rates than imaging the propagation of the onset of the mechanical activity, i.e., the electromechanical wave.

2.3.2 Arrhythmias

Conduction disorders or arrhythmic activity can be categorized as passive or active. Passive

arrhythmias occur when cardiac stimuli formation and/or conduction are below the normal range due to a depression of the automatism and/or a stimulus conduction block in the atria, atrioventricular junction, or the specific ventricular conduction system (Luna, 2011). The mechanisms responsible for active arrhythmias can be divided into two major categories: enhanced or abnormal pulse formation, and reentry. Reentry occurs when a propagating impulse fails to die out after normal activation of the heart and persists to reexcite the heart after expiration of the refractory period (Fuster and O'Rourke, 2008). Along with the pharmacological therapy, it is possible to treat these conditions with pacing, ablation or a combination of both. For example, the ventricle of a patient with an atrioventricular block will be driven by latent pacemakers at low rates (bradycardia); this condition can be corrected by inserting an artificial pacemaker that will drive the ventricle at a higher rate. Ablation therapy, on the other hand, can be used to "disconnect" a source of abnormal rhythm occurring in active arrhythmia.

2.4 Imaging the cardiac mechanics

Typically, imaging the cardiac mechanics consists mainly in mapping cardiac kinematics, i.e., displacements and strains, and usually at the time scale of the cardiac cycle. For example, techniques to estimate or map the end-systolic strains or peak-systolic strains have been developed to detect ischemic regions of the heart with varying degrees of accuracy (Edvardsen et al., 2001; Lee et al., 2011). While new techniques are being developed to map other parameters such as the Young's modulus (Bouchard et al., 2009; Couade et al., 2011; Pernot et al., 2011) and fiber orientation (Lee et al., 2012) by applying external forces, there is currently no methodology to map cardiac stress to eventually obtain other measurements such as

constitutive relationships and boundary conditions.

In the general case, the displacement vector field is a quantity that assigns to every location in space a three-dimensional vector describing a change in the configuration of a body. The displacement of a body has two components: a rigid-body displacement (translation, rotation) and a deformation. The strain tensor field is a nine-dimensional quantity that describes how a material segment deforms from a reference to a deformed configuration, including normal and shear strains. In this thesis, we limit our analysis to the classical linear elasticity theory, given that the inter-frame deformations to be estimated are very small (i.e., typically less than 1% and often as low as one tenth or even one hundredth of a percent (**Figure 3-3**)), as they occur between two frames acquired in rapid succession. The myocardium can be safely assumed to be linear within that range. In that case the strain tensor ε is symmetric and is given in Cartesian coordinates by

$$\varepsilon = \begin{bmatrix} \frac{\partial u_x}{\partial x} & \frac{1}{2}\left(\frac{\partial u_x}{\partial y} + \frac{\partial u_y}{\partial x}\right) & \frac{1}{2}\left(\frac{\partial u_x}{\partial z} + \frac{\partial u_z}{\partial x}\right) \\ \cdots & \frac{\partial u_y}{\partial y} & \frac{1}{2}\left(\frac{\partial u_y}{\partial z} + \frac{\partial u_z}{\partial y}\right) \\ \cdots & \cdots & \frac{\partial u_z}{\partial z} \end{bmatrix}, \quad \textbf{(2-1)}$$

Several techniques, such as X-ray, sonomicrometry, echocardiography and magnetic resonance imaging (MRI), have been developed and clinical systems have been manufactured in order to follow cardiac displacement and strain. Invasive techniques usually require the implantation of a small number of beads directly into the myocardium. X-ray techniques use implanted metal beads that serve as markers indicating how different cardiac structures move during a

heartbeat (Waldman et al., 1985). Sonomicrometry systems rely on small (~1 mm) implanted ultrasound transducers emitting and receiving signals giving their positions (Ellis et al., 1956; Lee et al., 2011). These methods usually provide high temporal resolution, but since the number of beads that can be implanted without significantly damaging the heart is limited, the resulting trade-off between spatial resolution and the size of the region of interest strongly limits studies.

Noninvasive approaches include imaging based on MRI and echocardiography. In MRI, myocardial tagging (Pai and Axel, 2006), harmonic phase (HARP) (Osman et al., 1999), and displacement encoding using stimulated echoes (DENSE) (Aletras et al., 1999) imaging methods have been shown capable of estimating all principal components of the strain tensor. However, as of today, these methods are not routinely used in the clinic despite the fact that MRI is becoming increasingly familiar to cardiologists. In addition, these techniques can be time-consuming due to the large efforts required to segment the heart walls, and MRI is hindered in its myocardial applications due to safety restrictions in its patient population that may exclude children, patients with old stents, pacemakers, claustrophobia, obesity or breath-holding issues.

Echocardiography is the predominant imaging modality in diagnostic cardiology due to its real-time feedback, noninvasive application, low cost, high temporal resolution, and multitude of complementary methods that can be used for a complete and accurate diagnosis. To avoid the strong reflections generated by the ribs, transthoracic echocardiography is performed using an ultrasound probe with a footprint (and thus aperture) small enough to fit in the intercostal

space. Center frequencies used are typically in the 1-5 MHz range to achieve sufficient depths, which can reach more than 20 cm. The proximity of the ribs and lungs, the small aperture of the probe, the relatively low frequency used, and the rapid motion of the heart limit the image quality and patient recruitment – depending on the application and the scanner used, it is not unusual to have exclusion rates of ten percent due to bad acoustic windows, see, e.g., (Sicari et al., 2008). Due to the presence of the ribs and lungs, only a limited number of views can be imaged and are categorized as follows: parasternal, apical, subcostal, and suprasternal views (Henry et al., 1980).

Ultrasound-based elasticity imaging deals with the estimation and imaging of mechanically related responses and properties for detection of pathological diseases, most notably cancer (Parker et al., 1990; Ophir et al., 1991; O'Donnell et al., 1994). More recently, similar methods were applied to cardiac applications (Heimdal et al., 1998; D'hooge et al., 2002; Konofagou et al., 2002) and encompass imaging of several kinds of mechanical functions, such as displacement, strain, strain rate, velocity, shear strain, rotation angle, etc., that can highlight the mechanical properties of the myocardium and their changes in the presence of disease. Ultrasound-based, high-resolution motion estimation can be achieved with time-shift-based or Doppler-effect-based motion estimation techniques. For example, Strain Rate Imaging (SRI) and Tissue Doppler Imaging (TDI) are mainly based on the use of the Doppler Effect for measuring velocity and strain rate. Drawbacks associated with the use of frequency domain techniques include low signal-to-noise ratio, poor resolution and aliasing. Time-shift-based methods based on the radio-frequency (RF) ultrasound signals provide higher accuracy (Walker

and Trahey, 1994) at high imaging frame rates. Therefore, recent efforts to improve quantitative displacement and strain estimations led to a temporal resolution at the scale of the electrical propagation time (Kanai et al., 1993; Pernot and Konofagou, 2005; Pernot et al., 2007), i.e., 2-3 ms per frame. Ultrasound is inherently directional and as such provides much higher accuracy in mapping motion and deformation along the ultrasound propagation axis.

2.5 Imaging the cardiac electrophysiology

Imaging the cardiac electrophysiology consists in mapping properties of the action potentials propagating in the tissue at a local level. Traditional approaches to mapping the electrical activity of the heart consist in putting one or an array of electrodes in contact with the myocardial tissue. Unipolar or bipolar techniques can be used: in the former, biopotentials are measured using single electrodes with respect to a common ground; in the latter, the difference in potential between two adjacent electrodes is measured. From such measurements, depolarization and repolarization times can be determined. For example, depolarization is defined as the time of occurrence of the maximum slope in unipolar mode and as the time of occurrence of the maximum potential in bipolar mode. Both unipolar and bipolar measures are similar (Kimber et al., 1996) and are believed to be correlated with the local time of cellular activation. Currently available clinical methods to map the electrical activation are all catheter-based, and are thus limited to mapping the endocardial or epicardial activation sequence; they are also time-consuming and costly. Even in a laboratory setting, mapping the 3-D electrical activation sequence of the heart can be a daunting task (Nash and Pullan, 2005). Studies of transmural electrical activation usually require usage of a large number of plunge electrodes to attain sufficient resolution (Durrer et al., 1970; Chattipakorn et al., 2003;

Sutherland et al., 2008), or are applied to small regions of interest *in vivo* (Ashikaga et al., 2007).

More recently, non-contact methods to map the electrical activation sequence have emerged. These methods typically provide the full action potential shape locally, and can even, in the case of optical imaging, characterize individual ions. Optical imaging techniques use voltage-sensitive dyes that bind to cardiac cell membranes and, following illumination, fluoresce if the cell undergoes electrical activation. Optical imaging methods can map the activation sequence of *ex vivo* tissue on endo- and epicardial surfaces (Kay et al., 2004; Qu et al., 2007; Ripplinger et al., 2009) and transmurally (Hooks et al., 2001; Hillman et al., 2007; Kong et al., 2009). However, because optical imaging techniques are affected by mechanical artifacts, they require the use of an electromechanical decoupler that inhibits cardiac contraction during imaging. Other newly developed methods to map the local electrical activity of the heart based on inverse problems are available: electrocardiographic imaging (ECGI) (Ramanathan et al., 2004, 2006; Zhang et al., 2005) and non-contact mapping (Taccardi et al., 1987; Schilling et al., 1998; Tai et al., 2004). The former is based on body-surface potentials and CT or MRI scans and provides reconstructed epicardial action potentials, including the atria (Wang et al., 2007). The latter consists in reconstructing the transmural potentials from potentials measured in the heart chamber. Although both methods are promising and have shown clinical relevance, they are based on the assumption that potentials can be accurately reconstructed through a severely ill-posed inverse problem, i.e., a problem very sensitive to modelization errors (Messinger-Rapport and Rudy, 1989; Belgacem, 2007). As of today, they remain to be validated

against robust, independent measurements across different patient populations (Lux, 2008; Olshansky, 2011).

2.6 Imaging the cardiac electromechanics

Imaging the electromechanics consists in mapping the transient deformations that occur in immediate response to the electrical activation. More specifically, we define the time at which a region of the heart transitions from a relaxing to a contracting state as the electromechanical activation. Spatially, this electromechanical activation forms a propagating wave front, i.e., the electromechanical wave (EW), which follows the electrical activation sequence. The electromechanical activation was found to be directly correlated to the electrical activation at the tissue level using invasive and noninvasive methods. Therefore, the EW propagation is similar to the electrical one, which can be modeled by, e.g., a reaction-diffusion equation (but not by the hyperbolic-wave equation).

Badke et al. used implanted ultrasonic crystals and electrodes in canines during atrial, RV, left-ventricular-apical (LVa) and left-ventricular-basal (LVb) pacing, and found a slope of 1.1 ($r = 0.91$) between the electrical activation time and the onset of shortening (Badke et al., 1980). Wyman et al. used high temporal resolution magnetic resonance taggingand bipolar electrodes during right-ventricular apical (RVa) and LVb pacing in canines and found a slope of 1.06 between the electrical activation and the first minimum circumferential strain following stimulation (Wyman et al., 1999). Using a similar approach, Faris et al. found a slope of 0.87 and 1.05 during right-ventricular pacing in four canines (Faris et al., 2003). These results

indicate that the electrical activation sequence could be deduced from the electromechanics.

As of today, no imaging method currently used in the clinic has been capable of mapping the EW. The electrical activation lasts approximately 60 to 100 ms and requires a resolution of a few milliseconds (e.g., 2-5 ms) to generate precise activation maps. Moreover, the regional inter-frame deformation that occurs at these frame rates is very small (~0.025-1% at a 2-ms temporal resolution) and requires a highly accurate strain estimator. Modalities such as standard echocardiography or MR tagging cannot detect the EW, since the time required to acquire a single image is similar to the duration of the entire ventricular depolarization. Effectively, since standard echocardiography was originally designed to assess the overall mechanics of specific cardiac segments over the entire heart cycle, images are typically acquired every 20-30 ms. Full-view speckle tracking techniques such as Tissue Doppler Imaging or Strain Rate Imaging have achieved motion estimation with high spatial resolution but require relatively low frame rates. Higher temporal resolution can be achieved using, e.g., M-mode, but at the expense of a very narrow field of view that does not allow spatial assessment of the propagation. Strain-mapping methods based on MRI in humans are not in real time, and their frame rates are typically smaller than in echocardiography, although temporal resolution on the order of 15-20 ms has been achieved in humans (Zwanenburg et al., 2004; Shehata et al., 2009).

Ultrasound was used more recently to map the electromechanics of the heart. Indeed, the first application of Electromechanical Wave Imaging (EWI) was to measure the displacements occurring during the electrical activation (Pernot and Konofagou, 2005; Pernot et al., 2007) and

led to the estimation of conduction-relevant velocities *in vivo* (Konofagou et al., 2010). Other groups have also used frequency analysis to determine the direction of propagation of displacements occurring during the electrical activation (Kanai, 2009). However, none of these studies succeeded in establishing a direct correlation between the measured displacement or phase maps with electrical activation times. In this dissertation, different imaging methods are developed and optimized to map strains, which are then directly correlated with activation times in normal and abnormal canines and in human hearts *in vivo* and *in silico*. Strains are independent of rigid motion, and result directly, unlike displacements, from the physiological response to the electrical activation.

2.7 Conclusion

There is no imaging modality that allows the noninvasive mapping of the electrical activation sequence available to the clinician. Electrical mapping techniques most commonly used rely on lengthy, minimally invasive procedures and require complex and costly infrastructure to generate activation maps. Newly developed methods such as ECGI are promising, but their reliance on patient-specific models, ill-posed inverse problems, and high-resolution imaging compromise their broad application. Electromechanical approaches show a promising link between the electrical and electromechanical activations of the ventricles but rely on methodologies that are either invasive or not applicable clinically. In Chapter 3, we show how high-frame-rate ultrasound imaging can be used to track the electromechanical activity of the heart using optimally estimated axial incremental strains.

Chapter 3 Motion and Strain Estimation with Ultrasound

3.1 Introduction

This chapter describes the concepts pertaining to image formation using ultrasound and to ultrasound-based motion and deformation estimation. The electromechanical wave (EW) is then defined within the context of ultrasound-based motion estimation and three criteria are established to optimize its estimation.

3.2 Image formation

Diagnostic ultrasound imaging is now almost exclusively based on the use of arrays of piezoelectric elements, which, when electrically excited, produce a vibration (1-10 MHz for cardiac applications) that is transmitted in soft tissue as mostly an ultrasound longitudinal compression wave. In conventional imaging sequences, arrays of piezoelectric transducers sequentially emit and receive ultrasound waves into focused beams, which are then concatenated to form images. Short pulses are emitted by the ultrasound probe, reflected by the object being imaged, and the returning echoes are recorded by the same probe. The times at which the reflected pulses reach the probe indicate their location, assuming a constant sound velocity (typically 1540 m/s in tissue). The duration (bandwidth) and center frequency of the electric pulses used to excite the piezoelectric elements define the axial resolution, i.e., along the beam, while the aperture defines the lateral resolution.

Delaying the pulses from element to element can be used to mimic the effect of a lens in order to generate a focus at a desired distance from the probe and steer it at different angles. Because of the small footprint of phased-array probes, echocardiography produces angular images typically spanning 90 degrees. It can be shown that the pressure field emitted is

approximately given at the focus by the Fourier transform of the aperture function, typically defined by its spatial extent and by delays and weights applied to the pulses (Wright, 1997). Two quantities linked by a Fourier transform are bound by the uncertainty principle, i.e., the larger the aperture, the finer the focus (and the lateral resolution), and vice versa. Once the beam is emitted, it will interact with the object to image in two major types of reflections: specular reflections and speckle. Specular reflections appear at the boundary of two sufficiently large structures with different acoustic properties (e.g., impedance). These types of reflection allow the visualization of anatomic structures such as the heart walls. Speckle occurs when the ultrasound signal propagates through a structure composed of elements of size similar or smaller than the wavelength, e.g., cardiac fibers. These reflections propagate back to the ultrasound probe whose elements piezoelectric responses are typically beamformed, sampled, processed, and displayed as an image. The beamforming process is symmetric in transmit and in receive modes, i.e., that the aperture function used in transmit mode can be applied in receive mode to improve the quality of the focus. By varying those aperture functions it is also possible to develop innovative imaging sequences. For example, a focus at a fixed distance can be used in transmit mode, while the receive mode focus can be dynamically modified to track the propagation of the ultrasound pulse. Following beamformation, a Hilbert transform is applied onto the radio-frequency (RF) lines to perform envelope detection, i.e., eliminate the rapidly varying, small-scale ultrasound oscillations to produce a readable image showing the large-scale anatomy. The speckle detected can be used as the signature of a specific region of the heart, the size of which depends on the wavelength. These speckle signatures can then be tracked from frame to frame to obtain the displacement vector and

strain tensor fields.

We hereby describe the process of image formation in pulse-echo ultrasound in more detail. Functions are represented in space and time by their temporal Fourier transform, i.e., (x,y,z,f). The entire image formation process can be described (approximately) by a series of spatial convolutions (denoted by $*$), where i(x,y) is one pixel resulting from beamforming (Wright, 1997):

$$i(x,y) = \int df\ H^2(f) \iiint dxdydz\ o(x,y,z,f)s(x,y,z,f) \quad \textbf{(3-1)}$$

where $s(x,y,z,f) = [w_r(x,y,z,f) * g(x,y,z,f)][w_t(x,y,z,f) * g(x,y,z,f)]$

The emitted pressure field from a transducer array located at x = 0 depends on the aperture function $w_t(x,y,z,f)$, often defined by the product of an apodization function $a(x,y,z,f)$ with a delay $\tau(x,y,z,f)$. For 2-D imaging, the apodization and delay functions are fixed in the z dimension but can be modified dynamically in the y dimension. For example, to focus the emmited pressure field to the location (x_c,y_c), with y_c corresponding to the middle of the transducer array, the delay function will be given by

$$\tau_n = \frac{R_n}{c} - \min_n\left\{\frac{R_n}{c}\right\} \quad \textbf{(3-2)}$$

where c is the speed of sound and R_n is the distance from of an element n of the transducer array to the desired focus (**Figure 3-1**). Electrical impulses are converted to pressure waves through a transfer function $H(f)$. The propagation of the pressure wave can be modeled by the sum of the Green functions $g(x,y,z,f)$ of propagation in free space (Huygens' principle) and will be reflected by the object to image o(x,y,z,f). This reflection can also be modeled by the Huygens principle as it travels towards the probe. In receive mode, each element of the probe

will convert incoming pressure waves into electric signals following the same transfer function H(*f*). These signals will be referred to throughout this dissertation as 'element data.'

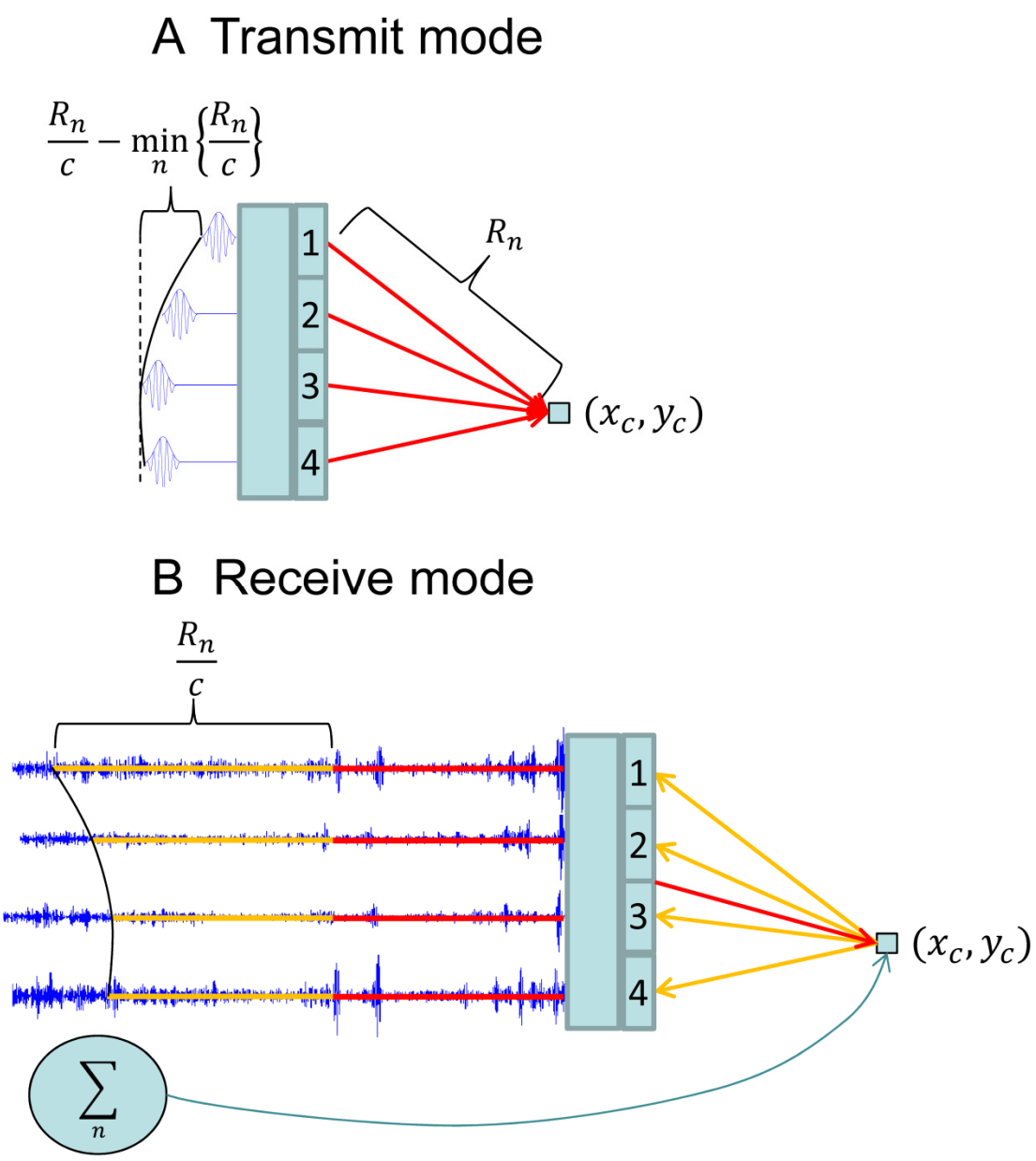

Figure 3-1 (A) Transmit and (B) receive modes in ultrasound imaging. (A) Delays corresponding to the travel time difference to reach a focal point (x_c,y_c) are applied in transmit mode. (B) In receive mode, data sample corresponding to the travel time of the ultrasound wave are summed to reconstruct individual pixels.

To reconstruct a pixel, the element data are delayed and summed. For example, to reconstruct

a pixel located at (x_c,y_c) (**Figure 3-1**B), the data samples corresponding to the time (**Figure 3-1**B) needed for the ultrasound wave to reach the receive focus (red line) and come back to the element (yellow lines) are summed to form a pixel at (x_c,y_c). This process can be repeated for each pixel to form a full image.

In conventional scanners, element data are not sampled and saved given the high computational power required to do so. They are instead immediately beamformed. For example, when using a probe with 64 elements, beamforming will convert 64 high frequency signals into one RF line. A simple (and approximate) way to do this is to apply the transmit mode delays as a beamforming function, in which case the output signal RF(t) can be related to the spatial location of the echo with the relationship $t = 2x/c$. Using dynamic focusing can improve the image quality. This requires more advanced electronics that allow time-varying delays; e.g., one could set a moving receive mode focus with time, e.g., $x_c = ct/2$. Similarly, the attenuation of the ultrasound wave can be accounted for with a time-varying gain function called the time gain compensation (TGC) that adjusts the gain (similar to the apodization function) as a function of time. Finally, because of their high frequency content, RF signals are not digitized and stored in most conventional scanners. Instead, a Hilbert transform is applied to the RF line, which has the effect of reducing significantly the frequency content, hence facilitating the sampling process. The output is one line of the final B-mode image, also called an 'A-line.' To produce a B-mode image with 64 lines, the process needs to be repeated 64 times. In modern ultrasound scanners, it is possible to sample the element data; in that case, the beamformation process is not limited by one operation per time step and can be performed

in software. This has multiple advantages; for example, the delay function in receive mode can not only vary with time but can also be changed for each point in space. In other words, it is possible to reconstruct an entire image for each transmit by varying the focus location in two dimensions.

3.3 Motion and strain estimation

To map the transient motion and deformation during the electrical activation with accuracy, inter-frame displacement fields are estimated axially via cross-correlation of consecutive RF frames (Ophir et al., 1991; Konofagou and Ophir, 1998), a motion-estimation method that can be up to ten times more accurate than B-mode-based speckle tracking (Walker and Trahey, 1994). Briefly, this method consists in dividing every ultrasound RF beam into a large number of overlapping, one-dimensional, mm-long windows. Reference windows are then compared with sliding windows in the following RF frame. More specifically, the normalized 1-D cross-correlation function $R(x,T)$ is given by

$$R(x,T) = \frac{\sum_{m=x}^{x+W-1} f(m)g(m+T)}{\sqrt{\sum_{m=x}^{x+W-1} f^2(m) \sum_{m=x}^{x+W-1} g^2(m+T)}} \qquad (T_1 \le T \le T_2) \qquad \textbf{(3-3)}$$

where x is the axial location of the origin of the reference window, W is the window size, T is the shift between the comparison and reference windows, and $[T_1,T_2]$ is the search range determined by the range of physiologic displacements. The location of the sliding window providing the maximum correlation determines the axial displacement between two consecutive sampled times. Sub-sample resolution is obtained by interpolating the correlation function (Céspedes et al., 1995). In this thesis, a fast table-sum implementation of RF cross-correlation with cosine interpolation is used (Luo and Konofagou, 2010). To limit the

computational cost, motion estimation is not typically performed for every RF sample. Instead, an overlap parameter is defined (typically 80-95%). After repeating this process for every window and every RF frame, we obtain axial displacements at multiple locations along the ultrasound beams and for every sampled time. From the displacements, one can then obtain the axial incremental strain (or 'strain' for brevity) depicting the EW by applying gradient operators on the displacement field. More specifically, a least-squares method (Kallel and Ophir, 1997) is applied using a Savitzky-Golay digital to reduce the noise amplification (Luo et al., 2004). In this thesis, only the axial component of strains is used for Electromechanical Wave Imaging (EWI), as it can be shown that the method is approximately angle independent (Chapter 5).

3.4 Contrast in Electromechanical Wave Imaging

The EW is the wave front of the electromechanical activation, i.e., the transition of a region of the heart from relaxation to contraction. To represent the EW in EWI, we use the strains or, in other words, the variation in cumulative strain between two frames. We define the electromechanical activation in EWI as the time at which the strain at a given point (x_o, y_0), $\varepsilon_{aa}(x_o, y_o, t)$ departs from or crosses zero for the first time following the electrical activation onset (t = 0) typically defined on the electrocardiogram (ECG). Formally, the electromechanical activation is given by the smallest t_a such that

$$\begin{cases} |\varepsilon_{aa}(x_0, y_0, t_a)| & < & \beta \\ |\varepsilon_{aa}(x_0, y_0, t_a + \delta t)| & > & \beta \\ sgn\{\varepsilon'_{aa}(x_0, y_0, t_a)\} & = & \gamma(x_0, y_0) \end{cases} \quad \textbf{(3-4)}$$

where ε'_{aa} is the first temporal partial derivative of incremental strains, β is a positive threshold (in absence of noise, one could set β=0), δt is a small time increment (infinitesimal in the

absence of noise and aliasing), and *sgn* is the signum function, which is equal to 1 or -1 when the non-zero variable it is applied to is positive or negative, respectively (**Figure 3-2**). $\gamma(x_0,y_0)$ depends on the angle between the heart wall and the axial direction of the ultrasound and is defined mostly empirically. For example, it is well known that in the ventricles, contraction of the heart results in radial thickening and circumferential and longitudinal shortening (Waldman et al., 1985; Villarreal et al., 1991; Lee et al., 2007, 2011). Therefore, during the electromechanical activation, the radial component of the strain tensor will transition from a negative to a positive value ($\gamma(x_0,y_0)$ = 1), while the circumferential and longitudinal components will transition from a positive to a negative value ($\gamma(x_0,y_0)$ = -1).

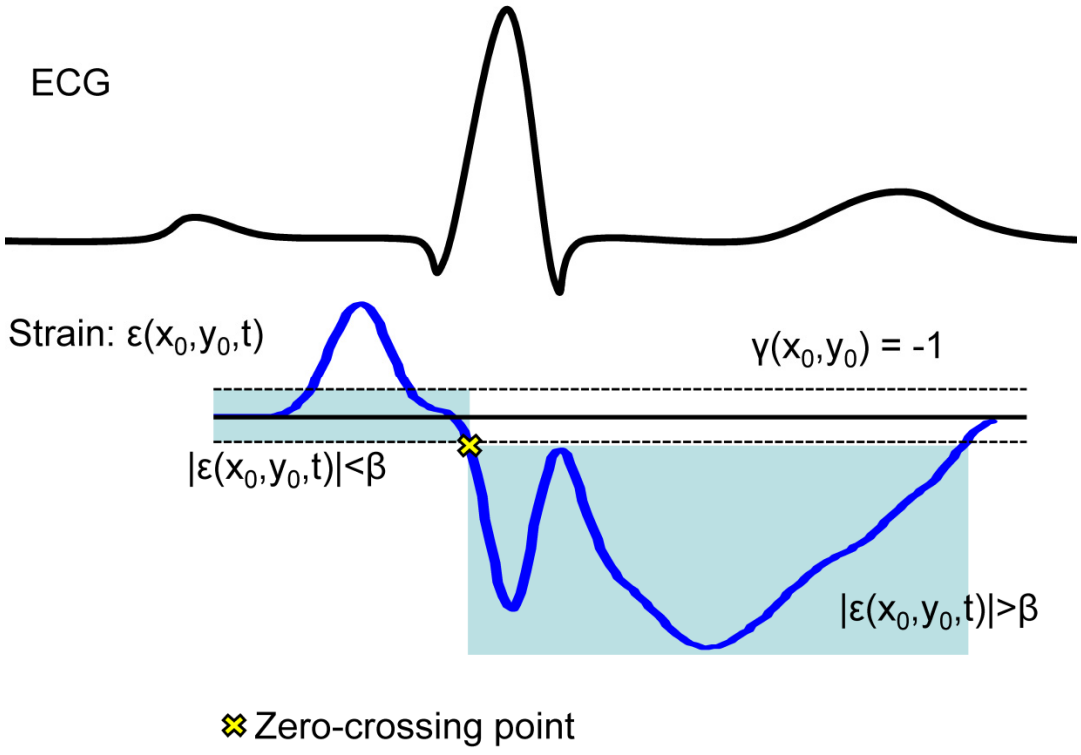

Figure 3-2 Electromechanical activation time as defined in EWI in a ventricular wall in an apical view ($\gamma(x_0,y_0)$ = -1). The zero-crossing point corresponds to a transition from positive strains (in this case caused by the atrial kick) to negative strains. Regions below and above the threshold value β are indicated. The zero-crossing time correspond to the time at which the transition between the two regions occurs.

To better interpret this definition of the electromechanical activation, consider the cumulative strain function at a given point (x_o, y_0), $e(x_0,y_0,t) = e(t)$. Then, the strain at a time t_0 can be defined as

$$\varepsilon(t_0) = e(t_0 + T_{me}) - e(t_0) \quad \textbf{(3-5)}$$

where T_{me} is the time separating two frames used for motion and strain estimation. When expanding $e(t)$ in Taylor series around t_0, we obtain

$$\begin{aligned} \varepsilon(t_0) &= e(t_0) + e'(t_0)(T_{me} + t_0 - t_0) - [e(t_0) + e'(t_0)(t_0 - t_0)] + O(T_{me}^2) \\ &= e'(t_0)(T_{me}) + O(T_{me}^2) \\ &\sim \frac{e'(t_0)}{r_{me}} \end{aligned} \quad \textbf{(3-6)}$$

where $e'(t_0)$ is the partial temporal derivative of cumulative strains, or strain rate, and is independent of the motion-estimation rate r_{me}. In other words, the incremental and cumulative strains are linked through a temporal derivative. Therefore, when the incremental strain is equal to zero, the cumulative strain reaches a minimum or a maximum. In other words, when the incremental strain departs from or crosses zero the corresponding heart region changes its behavior, i.e., it transitions from relaxation to contraction or from contraction to relaxation. Finally, the sign of the second temporal derivative of the cumulative strain (i.e, ε'_{aa}) indicates if this change corresponds to the former (contraction) or the latter (relaxation).

Mapping the EW can thus be accomplished by mapping the incremental strains for every point in the heart in a given echocardiographic view, and saturate the incremental strain values (e.g.,

at β or higher). The time when the strain departs or crosses zero (**Figure 3-2**), i.e., the EW, will thus appear as a sharp transition. The sign of the resulting saturated strain also reflects the sign of ε'_{aa}, and allows to distinguish electromechanical activation from relaxation.

3.5 Motion-sampling and motion-estimation rates

3.5.1 Motivation

The time required to form a conventional ultrasound image is dictated by the speed of sound, the imaging depth and the number of lines composing the image. For example, typical parameters to image a human heart are 128 lines at an 18-cm depth. Since the speed of sound in soft tissues is approximately 1540 m/s, the time required to form an image is 30 ms, i.e., the time required for an ultrasound wave to travel back and forth 18 cm of tissue, 128 times. As previously indicated, 30 ms between consecutive images are insufficient to track the electromechanics: the electrical activation of the ventricles lasts approximately 60 to 100 ms and thus requires a resolution of a few milliseconds (e.g., 2-5 ms) to generate precise activation maps. The first challenge in mapping the EW is thus to sample motion at sufficient rates (i.e., the motion-sampling rate). Moreover, the heart is an organ that undergoes significant three-dimensional motion and large deformations, which both lead to the decorrelation of the RF signals and thus to the degradation of the motion and deformation estimation accuracy. Consequently, the time lapse between the two frames used to estimate motion becomes a critical optimization parameter (Luo et al., 2007; Chen et al., 2009; Lee, 2010). If the interval becomes too long (at lower frame rates), decorrelation will corrupt the motion estimates. Conversely, if this interval becomes too short (at higher frame rates), the resulting smaller

motion may lie below the sensitivity of the motion estimator. The second challenge in mapping the EW is thus to estimate motion at an optimal rate (i.e., the motion-estimation rate).

In summary, it is expected that a higher motion-sampling rate will improve the strain estimation up to a maximum level after which increasing the motion-sampling rate further will provide negligible improvements. On the other hand, the motion-estimation rate that maximizes the strain estimation quality must be carefully optimized so that it is neither too high nor too low.

3.6 Optimal motion-estimation rate

3.6.1 Introduction

This section describes a framework to determine the optimal motion-estimation rate, which will then allow for the design of imaging sequences tailored for EWI in Chapter 4 . This framework is based on experimental data obtained from an open-chest canine, which is described in Chapter 5 . Determining a minimum motion-sampling rate is straightforward: the motion measured over time at a given pixel had a bandwidth of approximately 50 Hz at -20dB, corresponding to a minimum motion-sampling rate of 100 Hz. Other studies where the electromechanics of the heart were imaged also used similar or lower motion-sampling rates using other imaging methodologies (Prinzen et al., 1992; Wyman et al., 1999; Faris et al., 2003).

3.6.2 Methods

To assess the accuracy of a strain measurement, the elastographic signal-to-noise ratio (SNR_e)is

typically used, defined as:

$$SNR_e = \frac{\mu}{\sigma}, \quad \textbf{(3-7)}$$

where μ is the local average of strains ε at a given time, and σ the corresponding standard deviation. Previous literature (Varghese and Ophir, 1997) on the 'strain filter' indicates that the SNR_e will depend mostly on the magnitude of the strains measured, when the imaging parameters are fixed. This theoretical framework allows the derivation of an upper limit on the SNR_e as a function of the strain amplitude (a.k.a., the strain-filter) using a correlation model (Meunier and Bertrand, 1995). The strain filter corresponds, in this case, to the Ziv-Zakai Lower Bound (ZZLB) on the variance. The ZZLB is a combination of the Cramér-Rao Lower Bound (CRLB) and the Barankin bound (BB). The ZZLB transitions from the CRLB to the BB when decorrelation becomes important to the point that only the envelope of the signal contains information on the motion (Weinstein and Weiss, 1984). Measuring the SNR_e in the heart is a challenging task since the strains change rapidly both in time and space. To palliate this issue, we used an empirical approach to determine not only an upper limit on the SNR_e but the probability of obtaining any given SNR_e at any given strain amplitude. Strains measured in an open-chest paced canine obtained during separate acquisitions at different motion-estimation rates, i.e., {41, 82, 163, 350, 452, 855, 1100, 1283, 1540} Hz were used. The SNR_e at different motion-estimation rates was computed by averaging and calculating the standard deviation of the incremental strains within overlapping small axial windows (4.85 mm) over multiple frames, corresponding to up to five heart cycles, after segmenting the heart (Chapter 5). This approach provides the *SNRe* as a function of space and time, $SNR_e(x,y,t)$, where *x* and *y* are the axial and lateral directions, respectively, and *t* is the time. Data from every location are then combined

and, as a result, hundreds of thousands of SNR_e values for each motion-estimation rate were measured (the exact number depends on the motion-sampling rate, see Chapter 5). The theoretical strain filter was also calculated for the imaging parameters used in this study as a reference. For that purpose, an SNR of 1500 (60 dB) was assumed for the RF data, similar to what was previously considered in prior literature (Lee et al., 2007).

Let us consider the same heart with two strain distributions within $\varepsilon_1 \pm \Delta\varepsilon_1$ and $\varepsilon_2 \pm \Delta\varepsilon_2$ acquired at a rate r_{me1} and r_{me2}, respectively. According to eq. (3-6), we have

$$\varepsilon_2 \pm \Delta\varepsilon_2 = \frac{r_{me1}}{r_{me2}}(\varepsilon_1 \pm \Delta\varepsilon_1) = \frac{r_{me1}}{r_{me2}}\varepsilon_1 \pm \frac{r_{me1}}{r_{me2}}\Delta\varepsilon_1 \ . \qquad \textbf{(3-8)}$$

Therefore, if $r_{me2} = 2r_{me1}$, $\varepsilon_2 \pm \Delta\varepsilon_2 = \varepsilon_1/2 \pm \Delta\varepsilon_1/2$. In other words, when doubling the motion-estimation rate, both the center and width of the strain distribution are halved. Finding the optimal motion-estimation rate is thus equivalent to finding the optimal strain distribution.

To perform this optimization, we determine the probability of obtaining an SNRe value within a given interval, e.g., $[s_1, s_2]$, for a given strain ε_0, i.e., in a probabilistic framework, $P(s_1 < SNR_e < s_2 \mid \varepsilon = \varepsilon_0)$. Since we simultaneously measure SNR_e and ε, their two-dimensional histogram can be constructed and used to determine their joint probability density function (pdf), i.e., $f(SNR_e, \varepsilon)$. The individual pdf of SNR_e and ε can also be obtained from 1-D histograms. Finally, the conditional pdf $f(SNR_e \mid \varepsilon)$ can be obtained through the following relationship:

$$f(SNR_e|\varepsilon) \ = \frac{f(SNR_e, \varepsilon)}{f(\varepsilon)} \qquad \textbf{(3-9)}$$

Note that $f(SNRe)$, $f(SNRe, \varepsilon)$ and $f(SNRe \mid \varepsilon)$ also depend on the motion-estimation rate, r_{me}, and on the temporal portion of the heart cycle of interest, Δt_c, i.e.,

$$f(SNR_e|\varepsilon; r_{me}, \Delta t_c) = \frac{f(SNR_e, \varepsilon; r_{me}, \Delta t_c)}{f(\varepsilon)} \quad \textbf{(3-10)}$$

For simplification, we will use the two following assumptions:

a) f(SNR_e | ε ; r_{me}, Δt_c) = f(SNR_e | ε ; r_{me}), i.e., the relationship linking *SNRe* and ε does not explicitly depend on the cardiac phase. For example, a 1% strain occurring during systole will lead to the same *SNRe* distribution as a 1% strain occurring during diastole.

b) f(*SNRe* | ε ; r_{me}) = f(SNR_e | ε), i.e., the relationship linking *SNRe* and ε does not explicitly depend on the motion-estimation rate. For example, a 1% strain measured with a motion-estimation rate of 1500 Hz will lead to the same SNRe distribution as a 1% strain measured at 400 Hz. This assumption is stronger than (a). Effectively, in the heart, the decorrelation effect due to out-of-beam motion might be important and is not taken into account in our model. In such a case, a high motion-estimation rate would reduce decorrelation caused by out-of-beam motion in comparison with a lower motion-estimation rate and thus modify the relationship between SNR_e and ε.

Finally, the expected value of the *SNRe* was obtained as follows:

$$E\{SNR_e; r_{me}, \Delta t_c\} = \int_0^{+\infty} E\{SNR_e|\varepsilon; r_{me}\} f(\varepsilon; r_{me}, \Delta t_c) d\varepsilon \quad \textbf{(3-11)}$$

where the conditional expected value is given by

$$E\{SNR_e|\varepsilon; r_{me}\} = \int_0^{+\infty} SNR_e f(SNR_e|\varepsilon; r_{me}) dSNR_e \quad \textbf{(3-12)}$$

under assumption (a).

This implies that the expected value of SNR_e will vary during the cardiac cycle, i.e. as a function of Δt_c, as indicated in eq. (3-11). Therefore, two strain distributions were constructed: $f(\varepsilon; r_{me}$,

Δt_t) and $f(\varepsilon; r_{me}, \Delta t_a)$ where Δt_t and Δt_a correspond to five cardiac cycles (approx. 3000 ms) and the 20 frames following the R-wave (approx. 100-170 ms), respectively. $f(\varepsilon; r_{me}, \Delta t_t)$ was used to construct a robust conditional pdf, i.e., $f(SNR_e | \varepsilon; r_{me})$, based on a large enough number of samples (approx. 300,000) under assumption (a). By averaging $f(SNR_e | \varepsilon; r_{me})$ over all the motion-estimation rates, $f(SNR_e | \varepsilon)$ was obtained under assumption (b).

3.6.3 Results

The strain distribution varied both during the cardiac cycle and at different motion-estimation rates. **Figure 3-3** shows the variation of the strain distribution as a function of the motion-estimation rate when acquired over five cardiac cycles (**Figure 3-3**(a)) and during activation only (**Figure 3-3**(b)). At high motion-estimation rates, a bimodal distribution is obtained. A local minimum consistently occurs at an approximately 4% strain. This is in contradiction with eq. (3-6), which predicts a shift of that minimum. However, as the motion-estimation rate increases, the distribution translates towards lower strain values, narrows and becomes unimodal. This phenomenon is clearly depicted in **Figure 3-3**(c): As predicted by (3-8), the center and width of the strain distribution decreases in $(r_{me})^{-1}$. Finally, **Figure 3-3**(d) and (e) show the highly variable strain distribution as a function of time, during the cardiac cycle both during pacing and during sinus rhythm (for the sinus rhythm case only, data was acquired in a different canine using the automatic composite technique (Chapter 5.2)). For example, in **Figure 3-3**(e), high strain values are observed during the electrical activation (0-100 ms) and following repolarization (350-450 ms). During diastole, strain amplitudes vary greatly, i.e., from very high values (500-600 ms) to very low values (600-700 ms).

The probability of measuring a SNRe value simultaneously with a given strain value (i.e., the joint pdf) is shown in **Figure 3-4** (a),(c),(e). For low motion-estimation rates (41 Hz) (**Figure 3-4** (a)), the joint pdf spreads towards larger strain values and is associated with low values of SNRe. At 452 Hz (**Figure 3-4**(c)), the probability of higher SNRe values is higher, and located between 0.01% and 1% strains. At large motion-estimation rates (1540 Hz) (**Figure 3-4**(e)), the pdf is concentrated in lower strain values and lower SNRe values are more probable. These joint pdf's are, however, difficult to interpret as they directly depend on the probability of measuring strain; therefore, if, for a given motion-estimation rate, the probability of measuring a given strain was low, the probability of measuring the SNRe associated with that strain value was also low. To normalize this effect, we used the conditional pdf instead, shown in **Figure 3-4** (b),(d),(f). In that case, the probability is normalized for each individual strain value (eq. (3-10)).

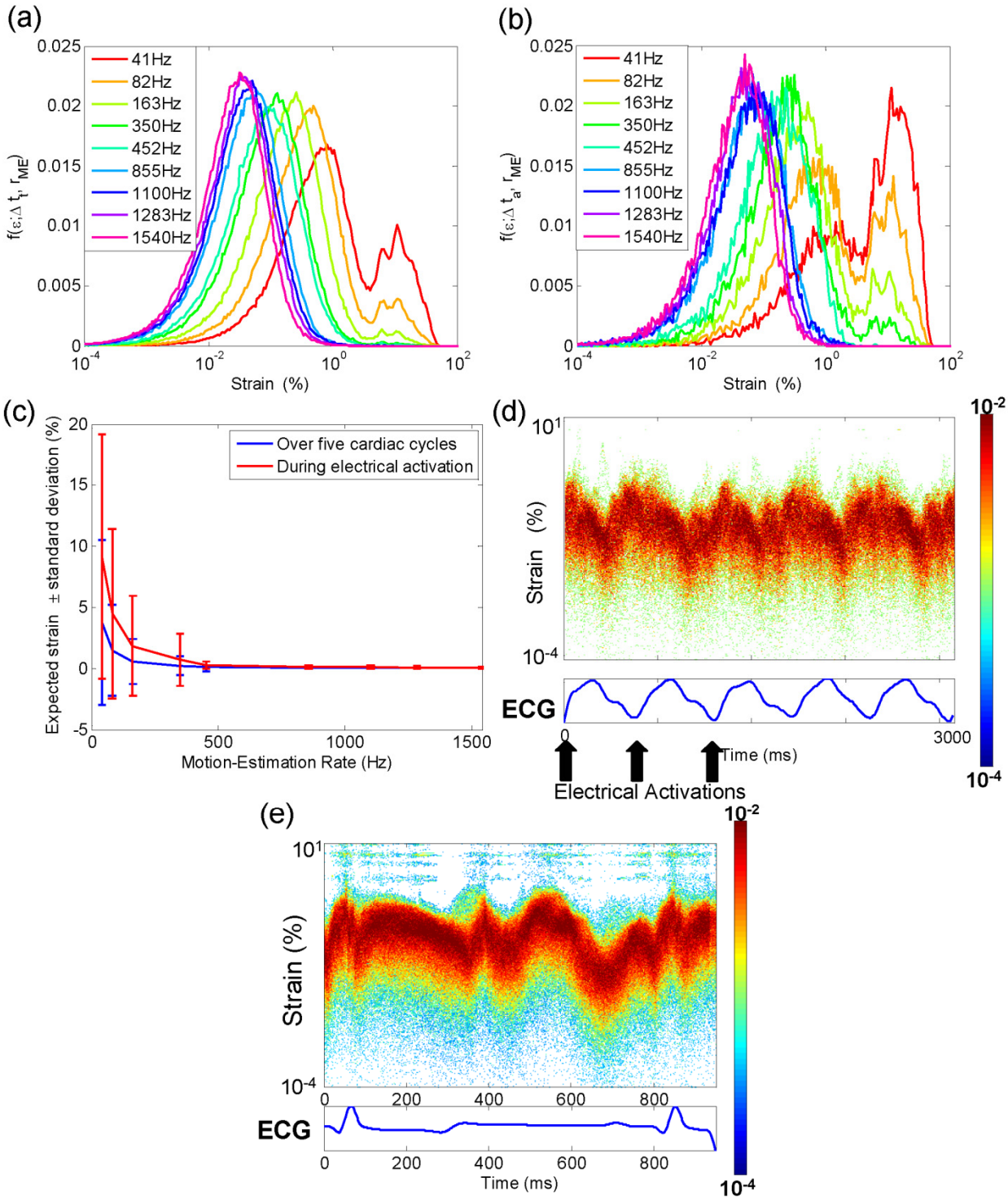

Figure 3-3 Strain distribution during (a) 5 cardiac cycles and (b) during activation only. (c) Center of the strains distribution for varying motion-estimation rates. (d) Strains distribution in a paced heart, motion-estimation rate: 855 Hz. (e) Strains distribution during sinus rhythm, motion-estimation rate: 520 Hz. (Provost et al., 2012)

However, it remains that, if a strain value was not measured in the experiment, it was impossible to obtain the conditional pdf for that strain value and thus it did not appear on these graphs. The different conditional pdfs obtained for different motion-estimation rates are very similar in overlapping domains at different motion-estimation rates; therefore indicating that assumption b) can be used: To obtain a complete representation of the conditional pdf, it was averaged over nine different motion-estimation rates (**Figure 3-5**(a)). The theoretical CRLB and BB are also shown. The SNRe achieved remained below the CRLB (red curve), with the conditional expected SNRe value being approximately one order of magnitude lower. An experimental transition zone corresponding to the minimum observed in **Figure 3-3**(a)-(b) at 4% strain was also added and corresponded to a sharp transition in the conditional pdf. For strains higher than 4%, the conditional pdf remained limited by the BB (blue curve). The motion-estimation rates corresponding to the center of the strain distribution over 5 cardiac cycles and during activation only are also shown, by computing $e'(t_0)$ in eq. (3-6). The average value of $e'(t_0)$ over five cardiac cycles, i.e., $e'(\Delta t_c)$, and during activation only, i.e., $e'(\Delta t_a)$, was 155.5 s^{-1} and 389.1 s^{-1}, respectively. **Figure 3-5**(b) shows the same conditional pdf with the conditional expected value of the SNRe. The peak conditional expected value of the SNRe is located between approximately 0.1% and 1% strain, which corresponds to 1555 and 155 Hz over 5 cardiac cycles, and to 3891 and 389 Hz during activation only, respectively.

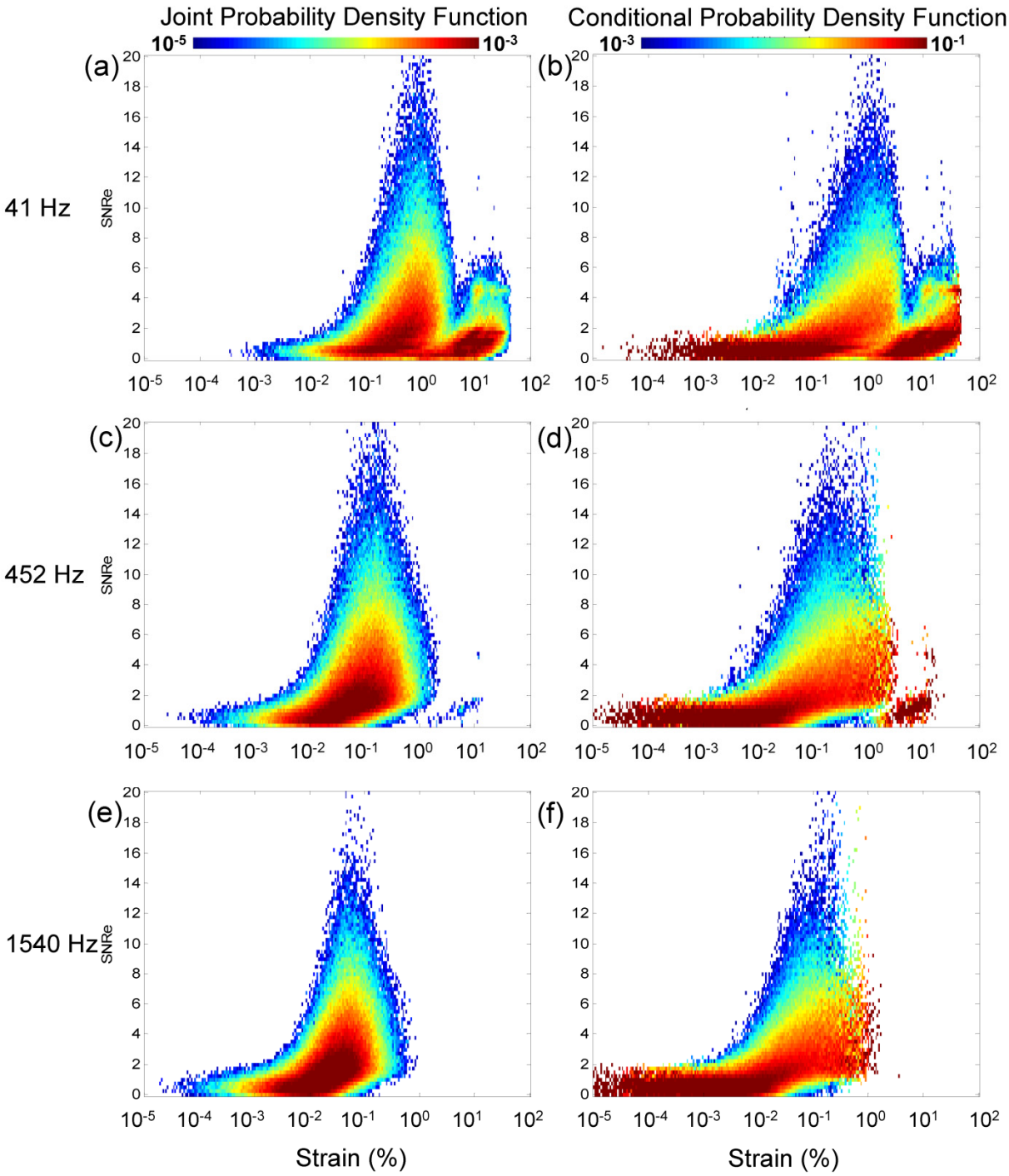

Figure 3-4 Joint and conditional pdf for a motion-estimation rate of (a-b) 41 Hz, (c-d) 452 Hz and (e-f) 1540 Hz, respectively. (Provost et al., 2012)

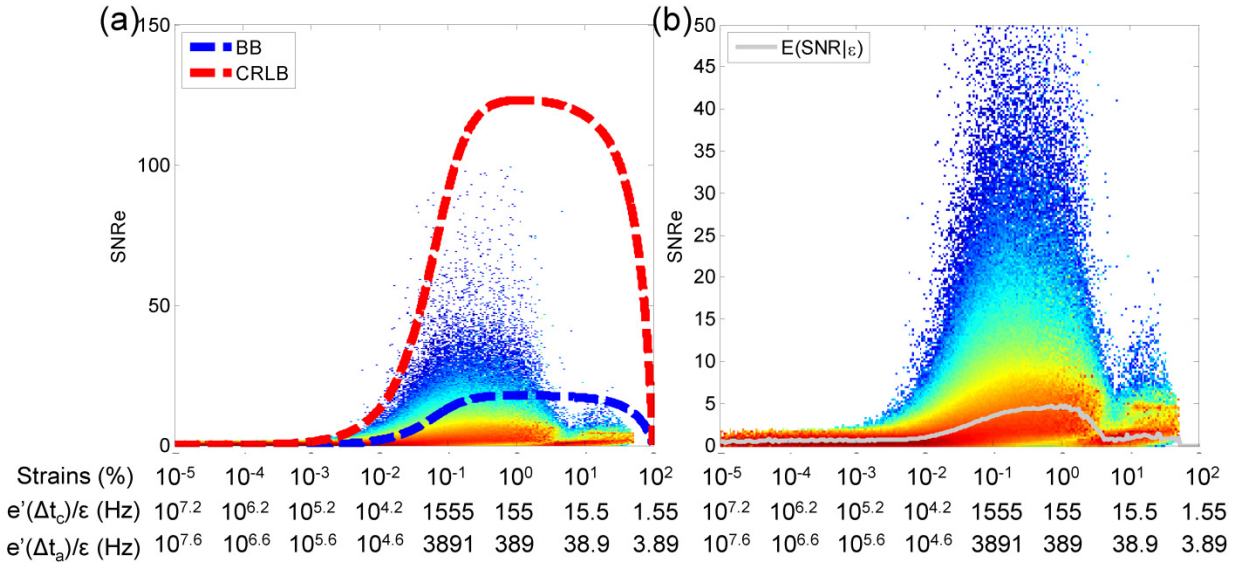

Figure 3-5 Conditional pdf constructed using acquisitions at different motion-estimation rates. (a) The BB, the CRLB and the experimental transition zone corresponding to the minimum observed in the strain distribution, and (b) the conditional expectation value of SNRe are also displayed. The motion-estimation rates corresponding to the strains amplitude are also indicated when averaging over five cardiac cycles and during activation only. Δt_t and Δt_a correspond to five cardiac cycle and the 20 frames following the R-wave, respectively. (Provost et al., 2012)

The expected value of the SNRe as a function of the motion-estimation rate was then obtained following eq. (3-11) for five cardiac cycles and during activation only (**Figure 3-6**(a)). Note that unlike the conditional expected value shown in **Figure 3-5**, the expected value encompasses an entire strain distribution. A sharp increase in the expected value of the SNRe is observed as the motion-estimation rate transitions from low values up to a maximum at 163 Hz and 350 Hz over five cardiac cycles and during activation only, respectively. The expected value of the SNRe then slowly decays with the motion-estimation rate. A similar behavior is observed in the variance of the SNRe (**Figure 3-6**(b)): a maximum is achieved at 350 Hz that decays at higher motion-estimation rates. Finally, the probability of obtaining a SNRe value higher than 3, 5 and

10 was also studied (**Figure 3-6**(c)). A maximum value also occurred at 350 Hz. For example, it is approximately twice as likely to obtain a SNRe higher than 3 at 350 Hz than at 41 Hz during activation.

3.6.4 Discussion

The strain magnitudes vary greatly throughout the cardiac cycle (**Figure 3-3**(d),(e)). Since the quality (i.e., the SNRe) of the strain estimation depends mostly on the strain magnitude and that the motion-estimation rate can be used as a means to translate and narrow the strain distribution (**Figure 3-3**), the motion-estimation rates used should be adapted to the cardiac phase of interest, e.g., the electrical activation of the ventricles. To find the optimal motion-estimation rate for EWI, the SNRe distribution was estimated in a paced canine *in vivo*, with a wide range of motion-estimation rates available with the temporally unequispaced acquisition sequence (TUAS) both during the electrical activation of the ventricles and over five cardiac cycles. By constructing first the joint pdf of the SNRe and the strain, the conditional pdf was obtained for every motion-estimation rate (**Figure 3-4**). By averaging these conditional pdfs, a combined conditional pdf spanning a large range of strain values was obtained (**Figure 3-5**). From this distribution, one can then compute a number of measurements (**Figure 3-6**) to characterize the distribution.

The combined pdf was in agreement with the strain-filter theory, which provides a higher bound on the SNRe (**Figure 3-5**). Electronic noise at very low strain values and decorrelation at very high strain magnitudes prevented high SNRe values in these ranges. The ZZLB predicts a sharp transition between the CRLB and the BB when decorrelation becomes important to the

point that the phase of the signal does not contain information about motion. Our findings suggest that this transition occurs in the vicinity of 4% strain (**Figure 3-3**(a), (b), **Figure 3-5**). **Figure 3-5** confirms that the combined conditional pdf is comprised within the CRLB up to approximately 4% before it becomes comprised within the BB. A sharp decrease in the expected value of the SNR_e is also observed at 4% strain and above, underlining the importance of using the phase information of the RF signal for accurate strain measurements. It was also observed that the strain distribution lacked values around this transition. A distortion in the strain distribution may indicate that while a high SNR_e can be maintained, the accuracy of the strain estimator is strongly impaired at low motion-estimation rates, i.e., less than 452 Hz in this case (**Figure 3-3**(b)).

To accurately map the EW, it is crucial to measure with high accuracy the strains occurring during the electrical activation. During the electrical activation, the strains mapped will vary from very small to very large values (**Figure 3-3**(b)): very small, i.e., close to zero, strains occur when the heart transitions from a relaxing to a contracting state and large strains occur when the heart undergoes rapid changes in cumulative strains, i.e., large incremental strains - see eq. (3-6). To achieve this goal, the strain distribution should be maintained below the transition zone, i.e., at motion-estimation rates equal to or above 452 Hz. Note that the common measure to establish the quality of strain estimation, i.e., the expected value of the SNRe, fails at depicting this fact: both the expected value of the SNRe and the probability of obtaining a SNRe value larger than 3, 5, and 10 point to an optimal motion-estimation rate of 350 Hz (**Figure 3-6**). This is due to the fact that these measures do not reflect the distribution of strains, e.g., the

expected SNRe cannot distinguish a case where all strains result in a similar SNRe from a case where half the strain values results in a high SNRe while the other half results in a very low SNRe. This effect is also illustrated by the fact that the highest expected SNRe also corresponds to the highest SNRe variance (**Figure 3-6**(b)).

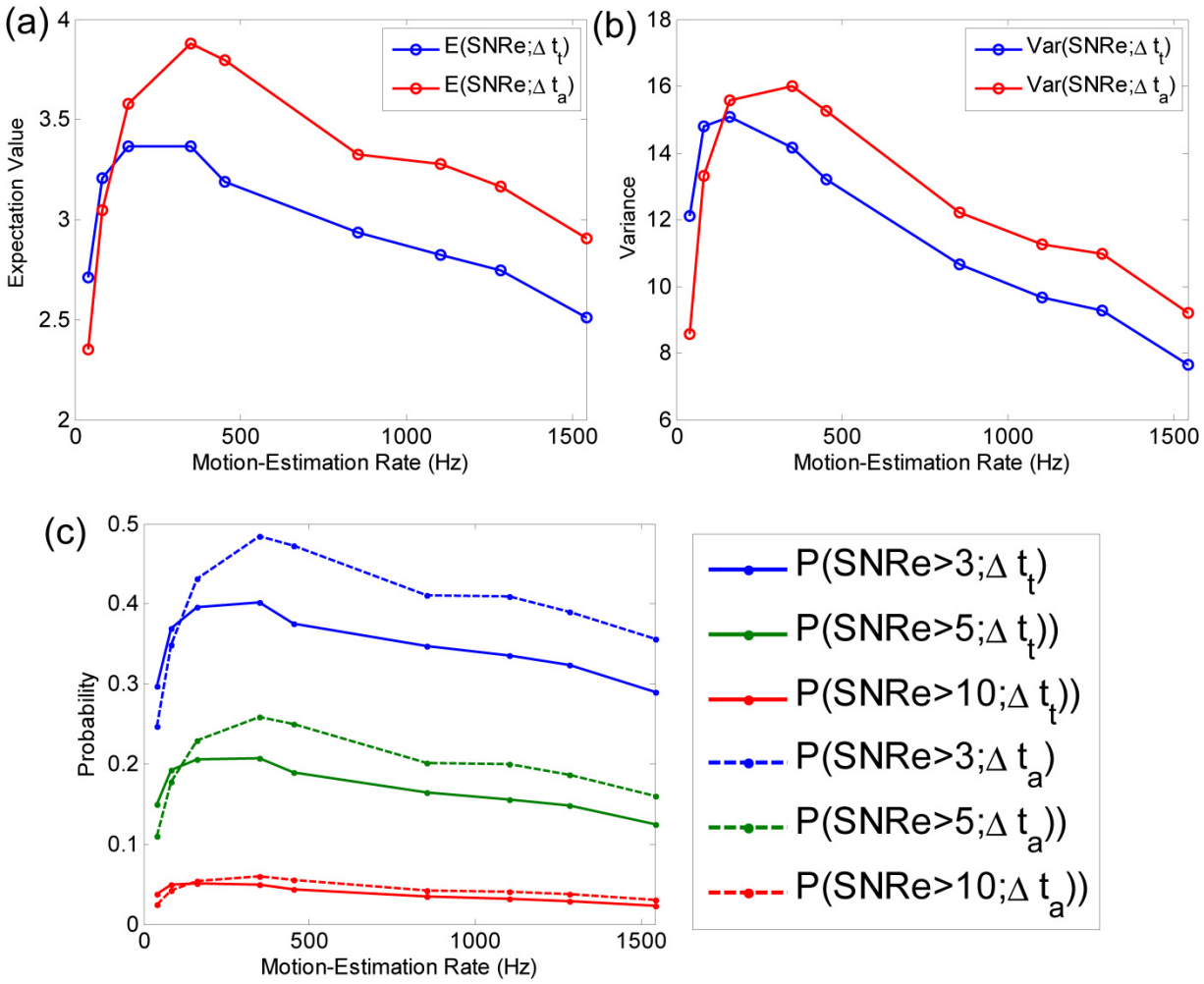

Figure 3-6 (a) Expectation value and (b) variance of SNR_e as a function of the motion-estimation rate. (c) Probability of measuring SNRe for different thresholds. Δt_t and Δt_a correspond to five cardiac cycles and the 20 frames following the R-wave, respectively. (Provost et al., 2012)

3.7 Conclusion

This chapter introduced concepts regarding image formation in ultrasound and how such images can be used for motion and deformation estimation. The electromechanical activation was defined as the time at which the axial incremental strain departs from or crosses zero. Moreover, the properties of strains occurring during the electromechanical wave were characterized: a minimum motion-sampling rate and an appropriate motion-estimation rate are necessary to avoid aliasing and to optimize the signal-to-noise ratio. Additionally, the spatial resolution must be adapted to the propagation velocity of the electrical activation. While this is easily achieved axially, the lateral sampling will depend on the number of beams emitted, which determines the frame rate. The electrical activation propagates at approximately 1 m/s in the myocardium; therefore, at a motion-sampling rate of 200-500 Hz (i.e., a temporal resolution of 2-5 ms) the lateral sampling should be on the order of 2-5 mm. This leads to a relatively high beam density: e.g., to achieve a lateral sampling of 5 mm at a 15-cm depth in a full field of view (90^{o}), 53 beams are necessary. This value is only indicative of the order of magnitude of the beam density; a smaller number of beams can be sufficient in some cases, while a larger number of beams can improve the resulting images, especially at large motion-sampling rates. In summary, the following criteria are required to perform EWI in all types of cardiac rhythms:

1. High-beam-density full-view RF imaging (>30 beams/90^{0})
2. Optimal motion estimation rate (500-2000 Hz)
3. High motion-sampling rate (>100 Hz)

Chapter 4 Methods

4.1 Introduction

None of the criteria established in Chapter 3 to capture the electromechanical wave (EW) are met by standard imaging sequences, although strategies to increase the frame rate have been developed in the literature. In standard echocardiography, the frame rate is determined by the number of beams acquired per frame. High beam density therefore leads to low frame rates and vice versa. For example, one can reduce the number of ultrasound beams used, which consequently results either in a smaller field of view (D'hooge et al., 2002; Konofagou et al., 2002) or in sparse-sector scans (Kanai et al., 1993). To avoid this trade-off, prior knowledge or changes in hardware can be used to increase the frame rate. One type of prior knowledge is the periodicity of the heart motion. In that case, the full field of view can be divided into multiple sectors acquired during different heartbeats, which are then reassembled in post-processing. Such composite imaging techniques can achieve very high effective frame rates, where the motion-sampling and motion-estimation rates are identical, in a full field of view with high beam density (Pernot and Konofagou, 2005; Pernot et al., 2007; Wang et al., 2008). However, composite techniques are difficult to use on arrhythmic cases or in patients who are unable to hold their breath. Another instance of prior knowledge is the largest frequency of the motion (i.e., the Nyquist limit). For example, sector-based sequencing consists of dividing the image into sectors, which are then acquired multiple times at a high rate for a short period of time before acquiring the next sector. However, if the time required to re-acquire the same sector location is too long, aliasing occurs. In sector-based sequencing, the motion-sampling rate is minimized (but remains sufficiently high to avoid aliasing), while very high motion-estimation rates can be achieved. This method is widely used for blood flow estimation, Strain

Rate Imaging (Heimdal et al., 1998) and for the estimation of the tissue motion for steady-state periodic excitations (Azar et al., 2010; Baghani et al., 2010). In modern scanners, individual piezo-electric elements of an array can be sampled. Such a feature allows the use of unfocused transmit approaches to increase the frame rate without the use of prior information. To increase the frame rate, approaches used in the literature consist thus in widening the transmit beam (Shattuck et al., 1984), sending multiple beams (Madore et al., 2009) or by sending plane waves (Tanter et al., 2002). Wide beams and multi-beam approaches are mostly used in the reconstruction of three-dimensional B-modes images and are currently available in clinical systems. Plane waves are mostly known for their use in supersonic shear imaging (Bercoff et al., 2004; Montaldo et al., 2009) where they are used for the estimation of one-dimensional (Montaldo et al., 2009) and two-dimensional motion (Tanter et al., 2002), but have not been used for transthoracic cardiac applications. In the heart, motion estimation was performed only recently using wide beams (Honjo et al., 2010). Although remarkable, this study was limited to a small field of view in humans, and did not report displacement maps or the measurement of strains at high frame rates. Modulated-Excitation and synthetic-aperture methods, which use advanced transmit mode strategies, have also been developed (Misaridis and Jensen, 2005), but have not been applied to the heart.

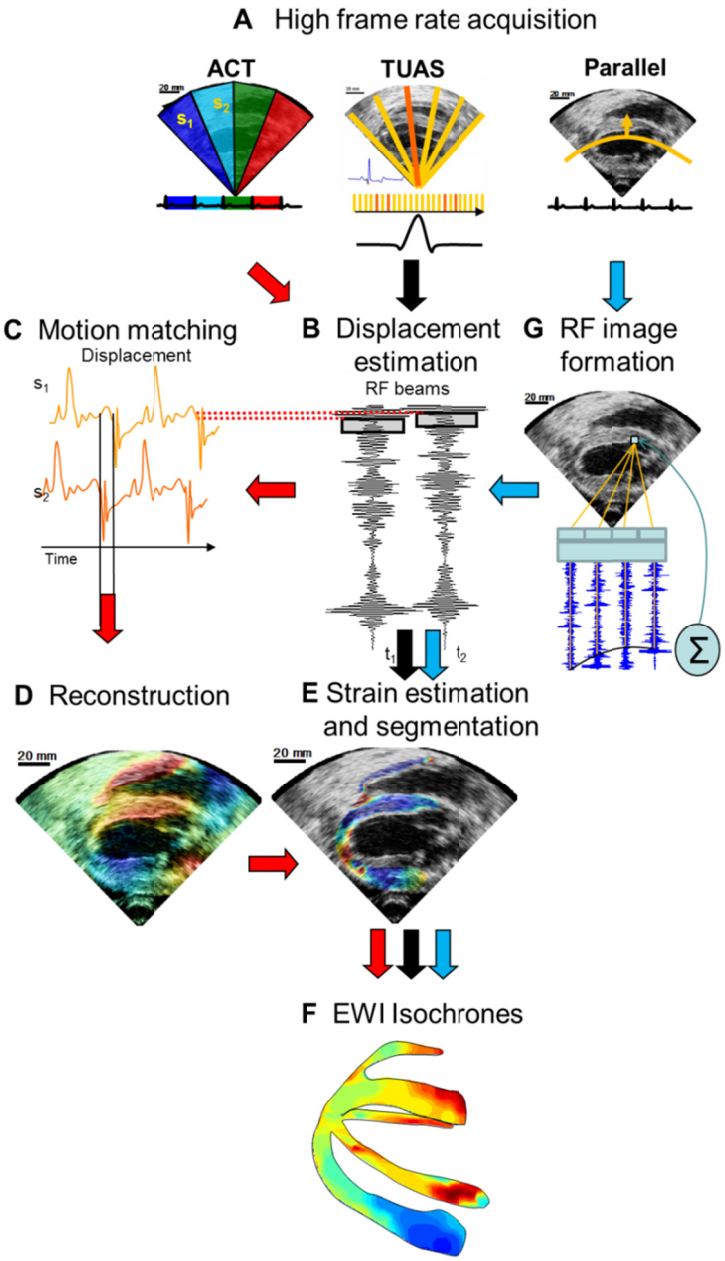

Figure 4-1 Block diagram of the EWI technique. (A) High frame-rate acquisition is first performed using either ACT (follow red arrows), TUAS (black arrows) or parallel acquisition (blue arrows). (B) High precision displacement estimation between two consecutively acquired RF beams (t1, t2) is then performed using very high frame rate RF speckle tracking. (C) In ACT only, a region of the heart muscle, common to two neighboring sectors, is then selected. By comparing the temporally varying displacements measured in neighboring sectors (s1, s2) via a cross-correlation technique, the delay between them is estimated. (D) In ACT only, a full-view ciné-loop of the displacement overlaid onto the B-mode can then be reconstructed with all the sectors in the composite image synchronized. (E) In ACT and TUAS, the heart walls are then segmented, and incremental strains are computed to depict the EW. (F) By tracking the onset of the EW, isochrones of the sequence of activation are generated. (G) In the case of parallel acquisitions it is necessary to perform image formation in order to obtain RF frames.

This chapter describes three implementations of Electromechanical Wave Imaging (EWI). They all require similar steps, i.e., radio-frequency (RF) image formation and reconstruction, motion and strain estimation, segmentation, overlay, and isochrones generation (**Figure 4-1**), and differ only in the strategy used to obtain RF frames. The following three sections describe these acquisition techniques, i.e., the automated composite technique (ACT) (**Figure 4-1**A,B,C,D, red arrows), the temporally unequispaced acquisition sequence (TUAS) (**Figure 4-1**A,B black arrows) and parallel acquisition (**Figure 4-1**A,G, blue arrows), and are followed by a section describing the processing necessary to generate the EWI ciné-loops and EWI isochrones.

4.2 Automated composite technique (ACT)

4.2.1 Rationale

The ACT technique relies on the periodicity of the heart rhythm to increase the imaging frame rate (**Figure 4-1**). It was implemented in both the Ultrasonix RP and MDP systems (Ultrasonix, Burnaby, BC, Canada) using the Ulterius package, with a 3.3-MHz phased-array probe and a sampling frequency of 20 MHz. More specifically, RF data from a full view of the heart is divided in multiple overlapping sectors (typically 5 or 7) that are acquired in a conventional manner during 2.5s each (Wang et al., 2008) (**Figure 4-1**A). Separate heart cycles are acquired in each sector. For example, an image that is composed of 65 RF lines can be divided in 7 sectors of 12 lines each with a three-line overlap between them. For an 18-cm depth, 12 lines can be acquired at 389 Hz; therefore, after reconstruction, the resulting effective frame rate is 389 Hz. The maximum frame rate that can be achieved with the Ultrasonix systems is 520 Hz. Note that in ACT the motion-sampling and motion-estimation rate are equal. After the sectors

are acquired, it is necessary to realign them temporally: this reconstruction is achieved using motion estimated in each sector (**Figure 4-1**B) and the motion-matching algorithm (**Figure 4-1**C,D).

4.2.2 Implementation

The motion-matching algorithm is illustrated in **Figure 4-2**. Five to seven sectors of 16 to 12 RF focused beams each were acquired consecutively. **Figure 4-2**(a) shows how two of those sectors can be realigned temporally to reconstruct a complete image. Three RF beams (in purple) on both sides of each sector overlapped for a full-view image containing 65 beams. Acquisition of each sector did not start at the same instant in the heart cycle. Therefore, to reconstruct a full-view ciné-loop, it is necessary to identify, and correct for, the temporal offset between sectors.

A conventional approach to solving this problem would be to acquire ECG signals along with each sector (Wang et al., 2008). The temporal offset between sectors could then be estimated by the offsets between the R-peaks of the ECG signals corresponding to each sector. As the method is also aimed for detection of conduction abnormalities, it is essential that the technique used here does not depend on the repeatability of the ECG. For example, during atrio-ventricular dissociation, the ventricles and the atria follow two distinct rhythms. The ECG will thus encompass both rhythms and the P- and R-waves may coincidentally have the same time occurrence, occasionally generating a fused waveform. An ECG-based method in that case might be difficult to implement, although the mechanics of the ventricles may still be periodic.

The alternative proposed here is to use the temporal evolution of the incremental displacements measured in the overlapping RF beams. This also simplifies the instrumentation by not requiring simultaneous ECG acquisition.

More precisely, if we assume the heart has a periodic motion, the same information is acquired twice in the overlapping regions. The periodicity of the heart implies that the following equation holds for all sectors *k*, depths *r*, angles (beams) ϑ, and times *t*

$$D_k(r,\theta,t) = D_k(r,\theta,t+nT) \quad \textbf{(4-1)}$$

where *D* denotes the displacement estimate, *T* denotes one heart cycle duration and *n* is an integer. Each sector is delayed with respect to the preceding by an unknown amount of time. This delay can be written as $n_k T + t_k$, with $t_k < T$. For the overlapping RF beams, denoted by a prime (ϑ'), the following equation holds:

$$\begin{aligned} D_{k+1}(r,\theta',t) &= D_k(r,\theta',t+n_kT+t_k) \\ &= D_k(r,\theta',t+t_k) \end{aligned} \quad \textbf{(4-2)}$$

Reconstructing the full-view image is equivalent to estimating t_k for all *k*. This is achieved by finding the time associated with the peak of the cross-correlation function:

$$t_k = \underset{r,t'}{\operatorname{argmax}} \int D_{k+1}(r,\theta',t) D_k(r,\theta',t+t')dt \quad \textbf{(4-3)}$$

This approach is illustrated in **Figure 4-2**(a). (4-3) was implemented numerically and the true peak was approximated using cosine interpolation (Céspedes et al., 1995). One of the main advantages of the motion-matching technique is that the cross-correlation method also provided a correlation coefficient that indicated the quality of the sector matching. A high correlation coefficient will ensure continuity of the reconstructed B-mode, and of the

reconstructed displacement and strain maps and cine-loops across the sectors. As the experiment conducted in this study usually comprises two to three heart cycles per sector, it was then possible to select the best combination out of multiple heart cycles. For example, if two heartbeats were acquired per sector over seven sectors, it would be possible to choose among 128 combinations of heart cycles. **Figure 4-2**(b) indicates good matching between the temporal profile of incremental displacements obtained in overlapping RF beams during two different heartbeats in a normal, open-chest, canine heart. **Figure 4-2**(c) displays the temporal correlation coefficient along the same RF beam.

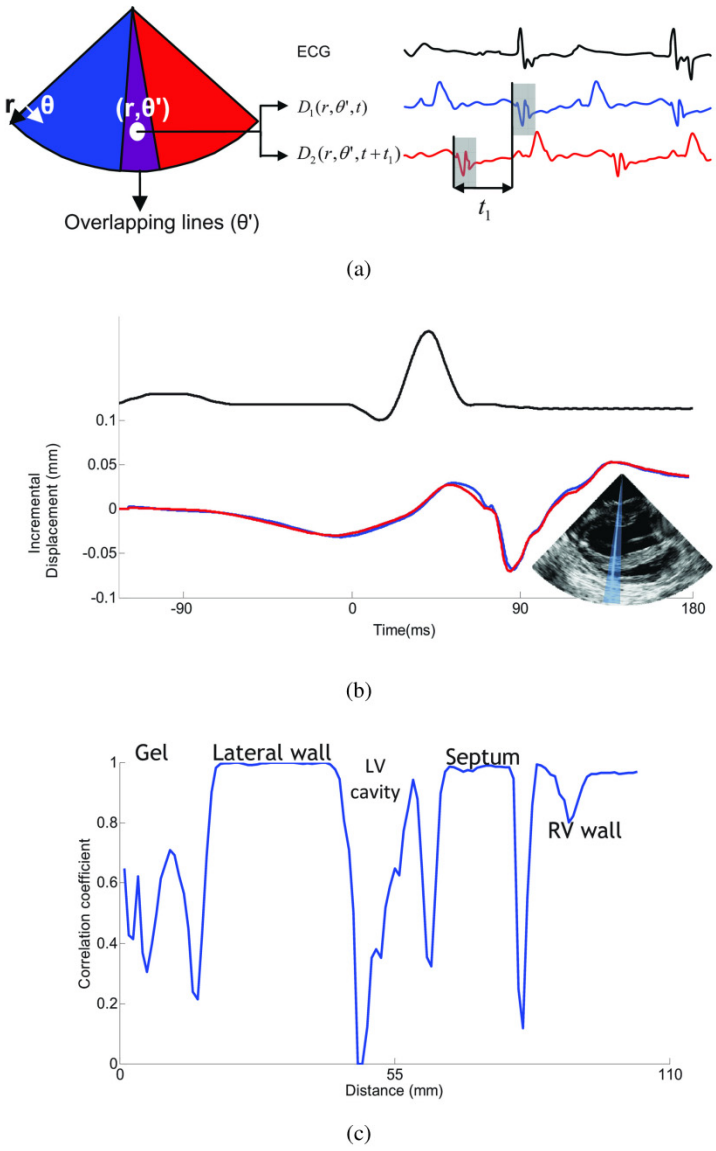

Figure 4-2 Illustration of the motion matching algorithm. (a) Axial incremental displacement is estimated twice in the overlapping RF-beams: once when sector 1 is acquired, and once when sector 2 is acquired. Assuming the periodicity of the heart, cross-correlation between those two independent acquisitions provides the time delay between the two sectors. (b) Incremental axial displacement over time of a sample located in the lateral wall acquired from an overlapping RF-beam. The blue line was acquired with sector 1 and the red line, with sector 2. One can observe the similarity between the two curves and the experimental periodicity of the heart's incremental displacements. (c) Cross-correlation coefficients of the incremental axial displacement over time along an overlapping RF-beam. These coefficients are close to 1 in the myocardial tissue, and dramatically drop in the cavity and in the ultrasound gel. (Provost et al., 2010)

A correlation coefficient close to 1 is obtained at the level of the myocardium, while the correlation was low in the blood cavities (due to blood flow and low scattering) and in the surrounding ultrasound gel (which does not undergo periodic motion). The final output of the motion-matching algorithm is a full view of a periodically beating heart, composed of 64 RF beams at a frame rate that cannot exceed 520 Hz (due to the computational limitations of the Ultrasonix scanner).

4.3 Temporally unequispaced acquisition sequence

4.3.1 Rationale

Conventional ultrasound imaging using a phased array consists of acquiring a number of beams, typically 64 or 128, over a 90° field of view (**Figure 4-3**(a)). These beams are acquired sequentially, and the process is repeated for each frame. For example, a given beam, e.g., beam *k* (**Figure 4-3**(a)), will be acquired at a fixed rate (**Figure 4-3**(b)). TUAS is thus characterized similarly by two distinct rates, the motion-estimation rate and the motion-sampling rate, defined as follows (**Figure 4-3**(b),(c)): The motion-estimation rate r_{me} is defined as the inverse of the time lapsing between the two RF frames used to estimate motion, i.e., T_{me}. The motion-sampling rate r_{ms} is defined as the inverse of the time lapsing between two consecutive displacement maps, i.e., T_{ms}. In conventional imaging sequences, these two rates are equal, because a given frame is typically used for two motion estimations (u_n and u_{n+1} in **Figure 4-3**(b)). In TUAS, the operator can adjust the motion-estimation rate. As shown in **Figure 4-3**(c), a frame in the TUAS case is used only once for motion estimation (**Figure 4-3**(c)),

thus halving the motion-sampling rate relative to the conventional method.

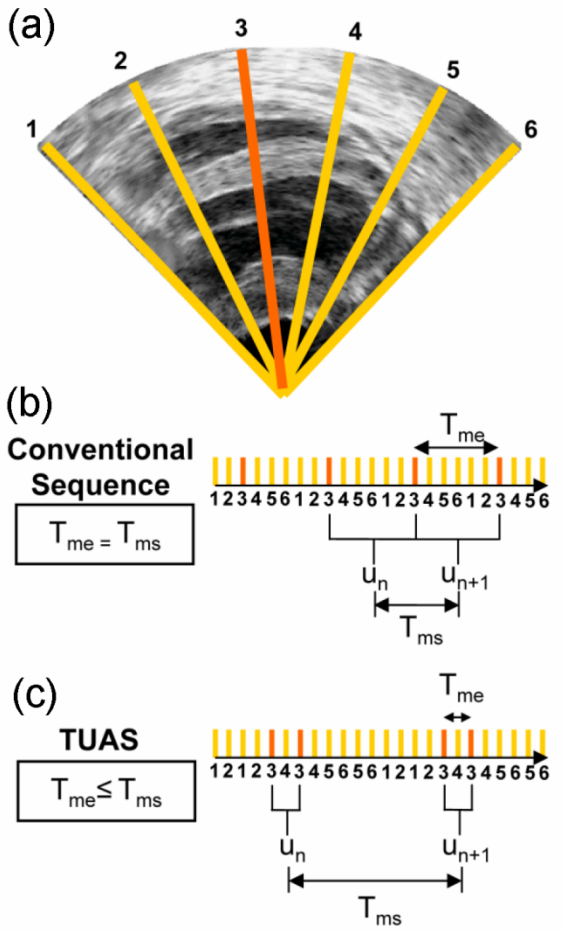

Figure 4-3 (a) Typical B-mode image containing N=6 lines. Acquisition times of a given line, e.g., line k, (b) in a conventional imaging sequence and (c) in a temporally unequispaced sequence. A displacement estimation is done between two RF lines separated by T_{me}. Displacement estimations are done every T_{ms}. (Provost et al., 2012)

For example, an acquisition performed at an 11-cm-depth with 32 beams with a conventional sequence will correspond to a frame rate of 219 Hz. However, while 219 Hz satisfies the Nyquist sampling criterion of cardiac motion, it is insufficient for accurate motion tracking using RF cross-correlation. Therefore, to reach a higher frame rate of, e.g., 500 Hz, the conventional

sequence requires halving the number of beams, and thus reducing either the beam density or the field of view or both. At the same depth and beam density, TUAS provides a motion-sampling rate of 109 Hz and a motion-estimation rate that can be varied, as shown in the following section, within the following group: {7000, 3500, 1750, 875, 438, 219} Hz. Both the lateral resolution and the field of view can be maintained while estimating the cardiac motion with an optimal frame rate, i.e., the motion-estimation rate that results in a larger elastographic signal-to-noise ratio (SNR_e). The tradeoff in this case is the halving of the motion-sampling rate; however, the motion-sampling rate has only a minor effect on the motion estimation accuracy. Theoretically, if this rate remains above the Nyquist rate of the estimated cardiac motion, it will have no effect. As shown earlier, a motion-sampling rate above 100 Hz is sufficient to accurately depict the EW.

4.3.2 Implementation

In a conventional imaging sequence, two consecutive frames with *N* beams per frame are acquired beam by beam in the order indicated in **Table 4-1**. This results in a time between two frames equal to $2dN/c$, where d is the imaging depth, N is the number of beams in the image, and *c* is the speed of sound. Motion is then estimated between the two consecutive acquisitions of beams at the same location. For example, motion is estimated through the cross-correlation of beam 1 acquired first and beam 1 acquired (N+1) beams later. Therefore, identical motion estimation and motion-sampling rates are obtained, equal to $c(2dN)^{-1}$.

TUAS was implemented in an open-architecture Ultrasonix MDP system (Ultrasonix Corp, Burnaby, BC, Canada) using the Texo Software Development Kit. In TUAS, the beams

constituting two frames are acquired in a different order. Beams are acquired consecutively within sectors containing k beams, and then repeated. **Table 4-1** describes different sequences for different values of k, e.g., for k = 1, k =4 and in the general case.

Axial motion is estimated between two beams acquired consecutively at the same location, which results in a motion-estimation rate of $c(2dk)^{-1}$. Since k needs to be a divisor of N, i.e., div(N), the group of available motion-estimation rates for a given number of beams is given by $c(2d)^{-1}\{(\mathrm{div}(N))^{-1}\}$. The highest motion-estimation rate occurs at k = 1, i.e., $c(2d)^{-1}$, and the lowest motion-estimation rate occurs at $k = N$, and is equal to that of a conventional imaging sequence, i.e., $c(2dN)^{-1}$. If motion is only estimated between the two closest acquisitions of the same beam in time, the motion-sampling rate is $c(4dN)^{-1}$. Note that in addition to motion being estimated between beams separated by T_{me}, lower motion-estimation rates can also be achieved by estimating motion between beams separated by T_{ms}-T_{me} (**Figure 4-3**), corresponding to a motion-estimation rate of $c(2d(N-k))^{-1}$, in which case the motion-sampling rate would be $c(2dN)^{-1}$.

Table 4-1 TUAS sequences. (Provost et al., 2012)

k = 1		k = 4		Arbitrary k	
Time (2d/c)	Line Number	Time (2d/c)	Line Number	Time (2d/c)	Line Number
1	1	1	1	1	1
2	1	2	2		…
3	2	3	3	k	k
4	2	4	4	k+1	1
5	3	5	1	…	…
6	3	6	2	2k	k
7	4	7	3	2k+1	k+1
8	4	8	4	…	…
…	…	9	5	3k	2k
2N-1	N	10	6	3k+1	k+1
N	N	11	7	…	…
		12	8	4k	2k
		13	5	4k+1	2k+1
		14	6	…	…
		15	7	2N-k	N
		16	8	2N-k+1	N-k+1
		…	…	…	…
		2N-7	N-3	2N	N
		2N-6	N-2		
		2N-5	N-1		
		2N-4	N		
		2N-3	N-3		
		2N-2	N-2		
		2N-1	N-1		
		2N	N		

4.4 Parallel Beamforming

4.4.1 Rationale

Having access to the element data allows the reconstructions of pixels at any location for each transmit (**Figure 4-1**A,G). However, if the location of a pixel corresponds to a region that is not insonified during transmit, its reconstruction will be inaccurate: e.g., a sharp drop of the signal-to-noise ratio of pixels occurs outside of the transmit mode focal zone for a standard, full

aperture transmit beam (**Figure 4-4**A). To increase the frame-rate rate, one simply has to increase the focal zone of the transmit beam, i.e., the transmit beam becomes the main parameter to optimize. Two types of beams are used in this dissertation: wide beams (**Figure 4-4**B), which can be generated by reducing the spatial extent of the transmit mode aperture, and a virtual-source sequence, which can be produced by applying transmit delays corresponding to a virtual point-source behind the probe.

4.4.2 Implementation

We developed customized imaging sequences using a Verasonics system (Verasonics, Redmond, WA) to sample the 64 elements of an ATL P4-2 phased array probe using point-source and wide transmit beams. A 2-D virtual point-source beam (or, virtual-source sequence for brevity) is a transmit mode in which every transducer element fires with the same amplitude but with delays such that the wave front generated propagates as if it were emitted from a single point 10.2 mm behind the probe. The lens that is typically present in phased-array probes results in planar focusing in the elevational dimension. This mode is similar to plane wave imaging (Bercoff et al., 2004), but the circular shape of the wave allows the probing of regions in the front and on the side of the probe. Therefore, the entire field of view is probed at each transmit, but the divergent nature of this transmit makes it more sensitive to artifacts originating, for example, from high impedance tissues such as the rib cage. A wide beam (**Figure 4-4**B) can be generated by reducing the transmit aperture, i.e., the number of elements used in transmit, and using apodization, i.e., the modulation of the transmit amplitudes of elements. In that case, only a portion of the image is probed at each transmit. This approach is also less prone to artifacts, as shown from its use in clinical systems to generate high quality three-

dimensional images. RF signals were reconstructed from the elements data in a pixel-wise fashion described as follows. Assuming a constant sound velocity, the element signal over time can be converted to a distance. The value of the RF signal at each pixel of the resulting image was then obtained by summing the 64 element data samples corresponding to time required for the emitted wave to travel to the pixel location, be reflected and reach a given element (Section 3.1). Subsampling resolution of the element data was achieved using linear interpolation. In the case of the virtual-source sequence, images were acquired at 2000 fps during 2s, followed immediately by the acquisition of a 128-lines, 30-fps, B-mode during 1.5s. The electrocardiogram (ECG) was acquired simultaneously. In the case of the wide beam sequence, a TUAS sequence was developed to transmit 12 beams twice at a rate of 137 Hz (motion-sampling rate) such that the repetition rate of these beams was 500 Hz (motion-estimation rate); no B-mode was acquired in wide beam acquisitions. More specifically, in the wide beam sequence, the amount of data acquired per frame was 12 times larger in comparison with the virtual-source sequence. This led to longer data transfer times and thus reduced the frame rate to levels insufficient for EWI. For example, 12-beam frames at a 12-cm depth are acquired at approximately 180 Hz, which is too low to perform EWI accurately. To palliate this issue, we used a TUAS approach and acquired a group of two frames before data transfer; note that in this case, TUAS is not only use to overcome physical limitations linked to the speed of sound, but also to avoid long transfer times between frames used for motion estimation.

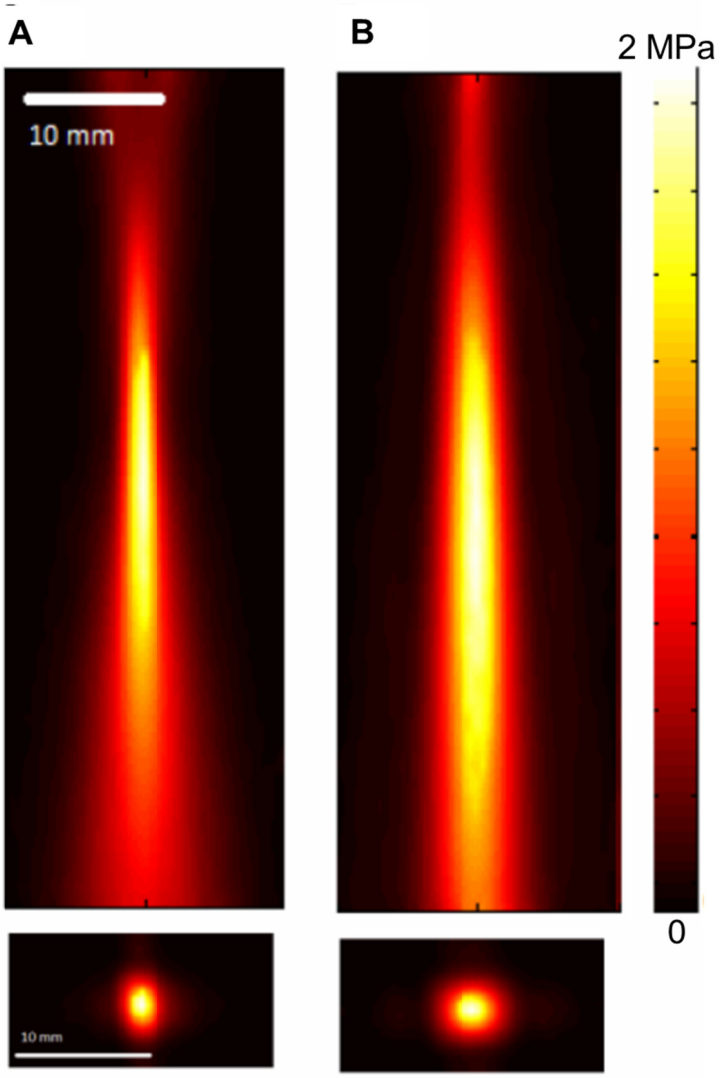

Figure 4-4 Beam profiles for different transmit mode settings of the Verasonics system. (A) Conventional transmit. (B) Wide beam. (Provost, Nguyen, et al., 2011)

4.4.3 Safety

Unlike the Ultrasonix system, the Verasonics system is not approved for human use by the Food and Drug Administration (FDA). In order to conduct human studies, the mechanical index (MI) and spatial-peak, temporal-average pressure (I_{spta}) were measured by suspending the emitting ultrasound probe (Phillips P4-2 ATL phased array) in a degassed water bath with the transducer

face oriented towards a hydrophone (Onda HGL-0400), a highly-sensitive device capable of measuring ultrasound pressures. The MI characterizes the mechanical bioeffects of the ultrasound and is proportional to the peak pressure achieved in transmit mode when the frequency and attenuation are maintained constant (which is the case, e.g., when we compare the virtual-source and wide-beam sequences against B-mode) and is limited to 1.9. The I_{spta} characterizes the thermal bioeffects of the ultrasound and depends on the spatial peak pressure and on the frame rate. These two safety parameters vary according to the input voltage applied to the probe elements (for a given transmit sequence) and is limited to 720 mW/cm in general, and to 430 mW/cm for cardiac applications (Center for Devices and Radiological Health, 2012). For a given voltage, conventional sequences result in higher MI and I_{spta} than the virtual-source sequence. Therefore, it is possible to use much higher voltages (and thus send more energy) when using a virtual-source sequence, while respecting safety standards. Since the image SNR is proportional to the emitted energy (Cobbold, 2007), the use of wide-beam or virtual-source sequences increases the SNR of the element data. However, other considerations, such as the poor lateral resolution associated with unfocused beams, will also alter image quality.

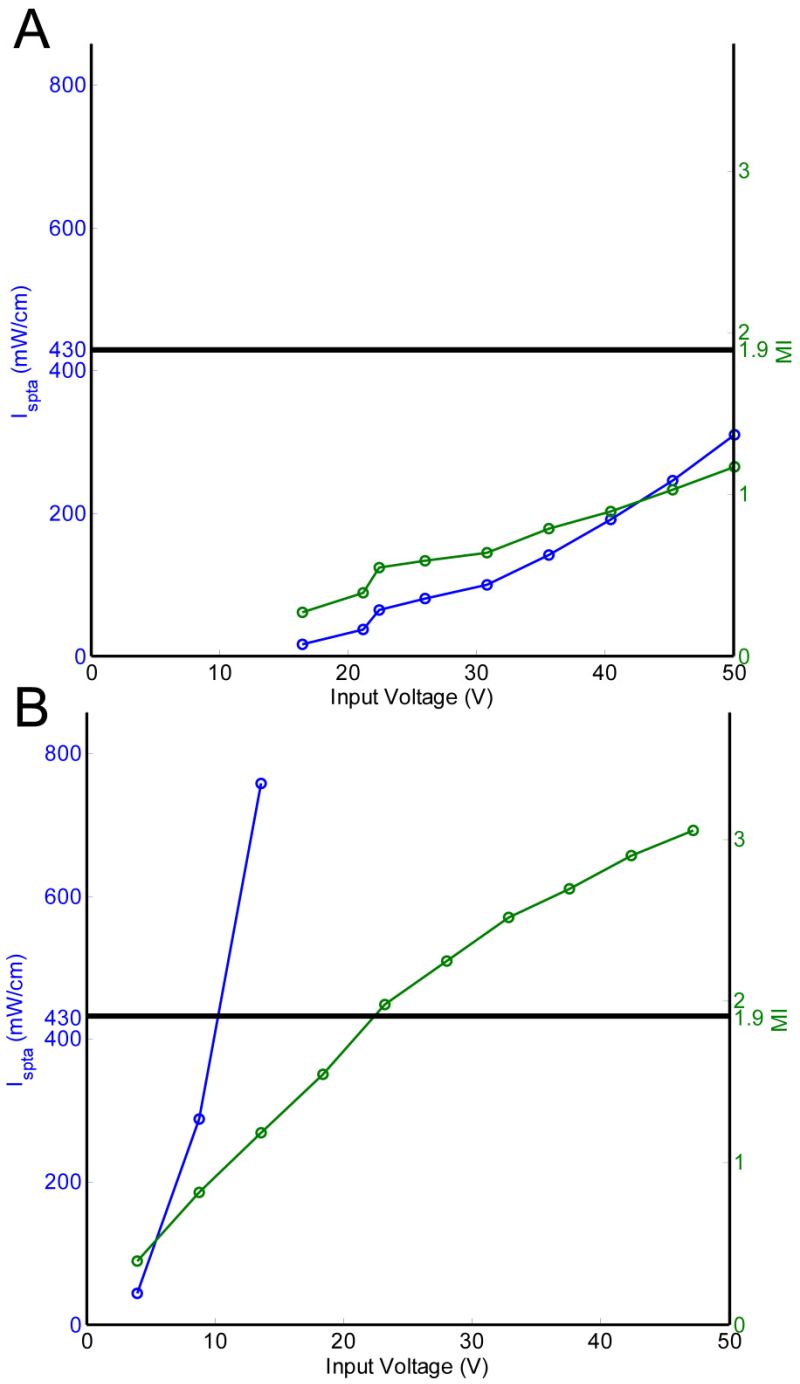

Figure 4-5 Safety parameters for (A) full aperture conventional sequence and (B) virtual-source sequence. The upper limits of both MI and I_{spta} correspond to the recommended limits provided by the FDA, i.e., 1.9 and 430 mW/cm, respectively.

4.5 EWI ciné-loop

The EWI ciné-loop (**Figure 4-1**E) is a video depicting the scan-converted, segmented, and saturated strains overlaid onto the B-mode images. Displacements and strains are estimated for each frame before segmentation is applied. Segmentation is then performed using the automated contour tracking technique (Luo and Konofagou, 2008). This method requires the segmentation of the first frame of interest and tracks this 'mask' from frame to frame using displacements obtained via the cross-correlation technique (**Figure 4-1** B). In its implementation for EWI, only axial incremental displacements are used. Additionally, to ensure the continuity of the mask, erosion and dilation operations are applied to the mask at each frame, along with filtering operations to maintain the smoothness of the mask edges. Since RF signals are obtained in polar coordinates (each RF line corresponds to an angle), they must be converted into Cartesian coordinates before they can be displayed, using bilinear interpolation. When necessary, temporal linear interpolation of the strains is performed to generate video frames at a 2-ms temporal resolution, therefore insuring consistent wave propagation velocities for acquisition made at different motion-sampling rates. When multiple views are displayed in bi- or multi-plane representation, they are temporally co-registered using the ECG signals, spatially co-registered by using anatomical landmarks and displayed in a three-dimensional biplane view using Amira 4.1 (Visage Imaging, Chelmsford, MA).

4.6 EWI isochrones

Isochrones (Figure 8F) are generated by mapping the first time at which the incremental strains

departed from or crossed zero following an event on the ECG, typically the onset of the P-wave when analyzing the four chambers of the heart, or the Q-wave when only the ventricles are mapped. More specifically, the absolute value of the incremental strains was minimized in a temporal window following the ECG event in up to a hundred manually selected regions. Subsample resolution was obtained through spline interpolation and Delaunay interpolation was used to construct continuous isochronal maps. When multiple views are displayed in bi- or multi-plane representation, they are temporally co-registered using the ECG signals, spatially co-registered by using anatomical landmarks and displayed in a three-dimensional biplane view using Amira 4.1 (Visage Imaging, Chelmsford, MA).

4.7 Conclusion

Three imaging sequences were presented in this chapter. While they all respect the necessary requirements outlined in Chapter 3, they also have individual advantages and disadvantages, described in Table 2. The ACT method can be implemented in most conventional ultrasound scanners and is probably the easiest to implement since it relies on the concatenation of standard sequences already available. It usually operates at frame rates between 300 and 500 Hz, depending on the imaging depth and on the number of sectors used. The number of sectors used will increase the acquisition duration, often up to 17-18 s. These long durations can be problematic with patients having irregular rhythms or whose acoustic window can be obscured by the lungs and need to hold their breaths. The frame rates achieved are more than sufficient for motion sampling, and are associated with high SNRe. The TUAS technique can also be implemented in a conventional scanner, but requires the capability of modifying the acquisition sequence, and is associated with low motion-sampling rates and low beam density.

However, it allows single-heartbeat EWI and can achieve an optimal motion-estimation rate. Finally, parallel acquisition sequences, while requiring a modern clinical scanner, can simultaneously achieve very high beam density, an optimal motion-estimation rate and a very high motion-sampling rate in a single heartbeat. On the other hand, it relies on divergent transmit beams, which are associated with lower lateral resolution in comparison with ACT or TUAS.

Table 4-2 : Summary of the different image formation options for EWI

	ACT	**TUAS**	**Parallel**
Beam Density	High	Low	Very high
Motion-estimation quality	High	Optimal	Optimal
Motion-sampling rate	High	Low	Very high (virtual-source) Low (wide beams)
Single heartbeat	No	Yes	Yes
Clinical Scanner	Yes	Yes	Yes

Chapter 5 Electromechanical Wave and Electrical Activation in Normal Hearts

5.1 Introduction

In this chapter and the following one, we aim to establish the level of correlation between Electromechanical Wave Imaging (EWI) and the electrical activation sequence. This goal is similar to the establishment of a new biomedical test, i.e., comparing a new methodology (i.e., EWI) against a gold standard (the electrical activation sequence). However, as explained in Section 2.5, mapping the electrical activation sequence, even during a non-survival animal experiment, is a daunting task. Additionally, the use of electrodes may alter the EWI measurements: the implantation of electrodes will affect the strains occurring in their vicinity and the fact that they are metallic will generate imaging artifacts. Therefore, we have developed three different approaches to validate against the electrical activation with varying degrees of interference with EWI:

1) Individual electrodes (study 1)
2) Basket catheter (study 2)
3) Simulations (study 3)

Using a small number of individual electrodes has the advantages of being relatively simple to perform experimentally and limiting ultrasound imaging artifacts and strain modifications, but provides a poor resolution. Basket catheters are a new product available in clinical electrophysiology to map the entire endocardial surface of a chamber (e.g., the left ventricle) with 64 electrodes. This approach provides a much higher mapping resolution than with implanted electrodes, but requires complex acquisition systems. The catheter also generates a force against the endocardium as well as a large amount of artifacts in ultrasound images. Finally, simulations have the advantages of mapping the full 3-D propagation of the electrical

activation, including the transmural, providing perfect spatial registration between the EWI and the electrical activation, and a complete absence of imaging artifacts, but rely on a number of assumptions included in the model. In this chapter, these three methodologies are applied to normal hearts during sinus rhythm and during pacing.

5.2 *In vivo* validation

5.2.1 Methods

In this study, approved by the Institutional Animal Care and Use Committee of Columbia University, five (n=5) mongrel dogs of either sex, ranging from 23 to 32 kg in weight, were anesthetized with either an intravenous injection of thiopental (10-17 mg/kg) or with an intravenous injection of Diazepam 0.5-1.0mg/kg IV as premedication, and Methohexital 4-11mg/kg IV as induction anesthetic. All animals were mechanically ventilated with a rate- and volume-regulated ventilator on a mixture of oxygen and titrated isoflurane (0.5-5.0%). Morphine (0.15mg/kg, epidural) was administered before surgery, and lidocaine (50 micrograms/kg/hr, intravenous) and/or Heparin (100,000 IU/h, intravenous) were used during the whole procedure. To maintain blood volume, 0.9% saline solution was administered intravenously at 5mL/kg/hr. The animals were positioned supine on a heating pad throughout the entire procedure (to avoid hypothermia). Standard limb leads were placed for surface electrocardiogram (ECG) monitoring. Oxygen saturation of the blood, and peripheral blood pressure were monitored throughout the experiment. The chest was opened by lateral thoracotomy using electrocautery.

5.2.1.1 Individual Electrodes

In this study, three dogs were used. Solid state pressure transducer catheters (Millar Instruments, Houston, TX) were inserted into the left-ventricular cavity via the right carotid artery and in the aorta. After removal of the pericardium, up to twelve sonomicrometry crystals with a 2-mm diameter combined with bipolar electrodes were then implanted in the ventricles. Sonomicrometry signals were not used for the purpose of this study and were turned off when ultrasound images were acquired. For endocardial and mid-wall crystals, an 18G needle was used for insertion. All crystals were maintained in position after placement using silk sutures. Pacing and electrophysiology measurements were performed using the same crystal types. Recording electrodes were located in the mid-wall along the two-chamber view and pacing electrodes were located on the epicardium along the four-chamber view (**Figure 5-1**). The time of electrical activation was determined by identifying the maximum value of the bipolar electrode signal. As unipolar and bipolar potential mapping have been shown to be nearly identical (Kimber et al., 1996), bipolar mapping was preferred to avoid difficulties such as far-field potentials.

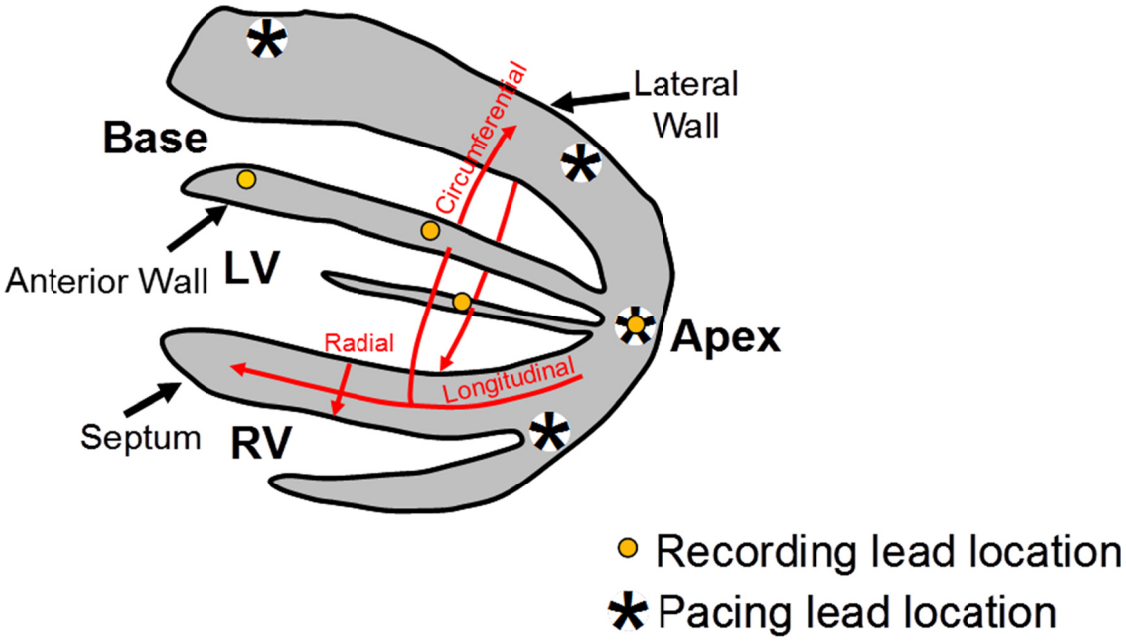

Figure 5-1 Positions of the pacing and recording electrodes in sub-study #1 and representation of the radial, longitudinal and circumferential coordinates of the heart. (Provost, Lee, et al., 2011a)

5.2.1.2 Basket Catheter

In this study, two dogs were used. A basket catheter of either 31 or 38 mm in diameter was inserted in the left ventricles either by canulating a pulmonary vein with a 9F sheath and guided, using ultrasound, to the left ventricle or through an apical puncture (**Figure 5-2**). This basket catheter contains 64 electrodes that were used to generate 3-D endocardial maps of the electrical activation. Four custom-built acquisition boards containing 16 channels each were used to measure 56 bipolar electrograms and three ECG leads (**Figure 5-3**). The multiplexed outputs of the individual boards were then sampled by a low-cost, USB data acquisition system (USB-6259, National Instruments, Austin, TX) controlled via a LabView interface. Pacing could also be performed from any electrode, thus allowing multiple, simultaneous (up to a 2-ms resolution) pacing sites. A separate, open-source Arduino Mega board (www.arduino.cc)

containing a micro-controller was used to send pacing stimulus through transmit multiplexers and was controlled via a C-based algorithm. Images in the four-chamber view were acquired using wide beams during pacing from the apical region of the lateral wall. In one dog, axial displacements were estimated at a 500-Hz motion-estimation rate and a 137-Hz motion-sampling rates a wide beams sequence. The window size was 4.60 mm and the overlap 90%. In the other dog, axial displacements were estimated at 1000 Hz with a motion-sampling rate of 2000 Hz using an axial window of 9.2 mm with virtual-source sequence. The incremental axial strains were estimated with a kernel size of 10.7 mm in both cases.

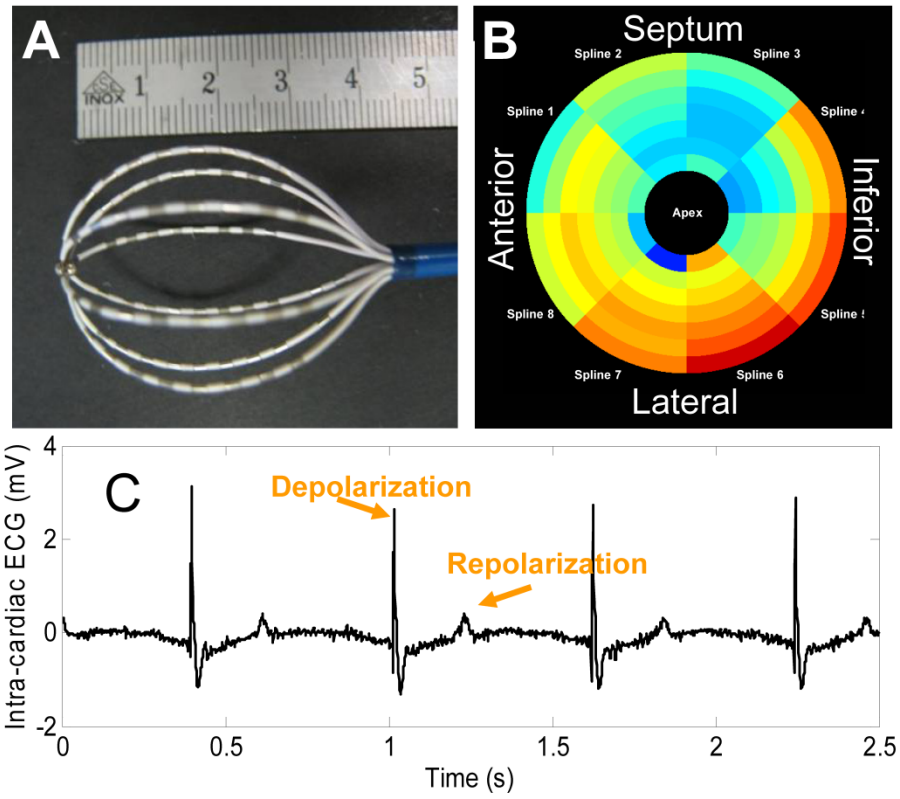

Figure 5-2 (A) Basket catheter used in sub-study #2. (B) Isochrones and (C) signals obtained in the bipolar mode. Bipolar signals could resolve both depolarization and repolarization.

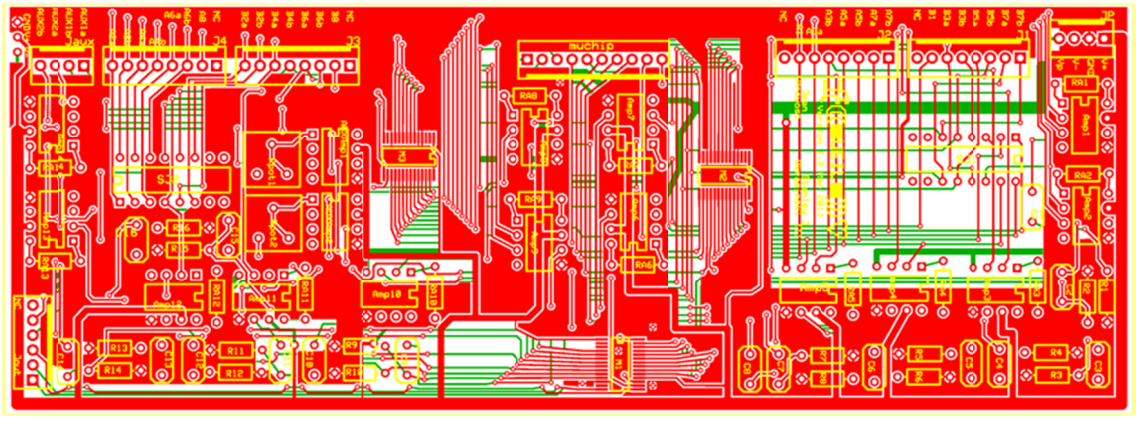

Figure 5-3 Printed circuit board design for amplification and multiplexing of 16 measured potentials and/or applied currents. A total of four boards were used to sample the bipolar potentials from 56 pairs of electrodes.

5.2.2 Results

To establish the feasibility of studying electrical cardiac events using EWI, the three canines that were implanted with individual electrodes were imaged *in vivo* during sinus rhythm and four distinct epicardial pacing protocols as follows: 1) from the basal region of the lateral wall (LVb), 2) from the left ventricle apex (LVa), 3) from the apical region of the anterior-lateral wall of the left ventricle (LVar), and 4) from the apical region of the lateral wall of the right ventricle (RVa). Bipolar electrograms were also acquired simultaneously in two of the three canines.

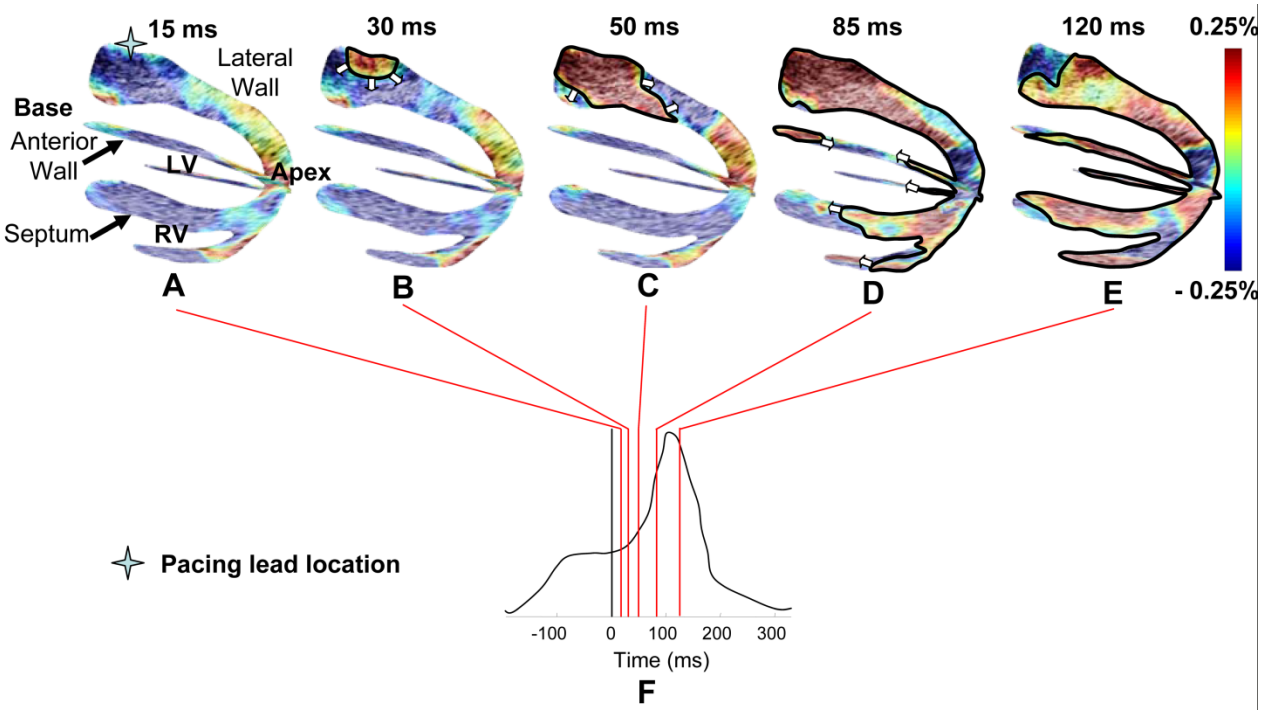

Figure 5-4 Propagation of the EW when paced from the lateral wall, near the base. Activated regions are traced at (A) 15 ms, (B) 30 ms, (C) 50 ms (D) 85 ms and (E) 120 ms and indicated on the (F) electrocardiogram. 0 ms corresponds to the pacing stimulus. (A-C) The EW propagates from the basal part of the lateral wall towards the apex. (D) Note that in the apical region, a transition from lengthening to shortening is observed rather than a transition from thinning to thickening. (D-E) In the anterior wall, the EW propagates from both the base and apex. The scale shows inter-frame strains. (Provost, Lee, et al., 2011a)

Two standard image planes, identical to the apical four- and two-chamber views used in echocardiography, were selected. The alignment of those two planes in a bi-ventricular view using anatomical landmarks such as the apex allowed a three-dimensional depiction of the electromechanical wave (EW) propagation (**Figure 5-4**). **Figure 5-4** depicts the propagation of the EW at different time-points following pacing from the basal region of the lateral wall (**Figure 5-4**A-E), as indicated on the electrocardiogram (**Figure 5-4**F). Colors correspond to extension (red) and compression (blue) of the myocardial tissue along the direction of the ultrasound beam. Due to the positioning of the ultrasound probe during those experiments, the strain estimation was performed mostly in the radial direction, except in the apical region of the

anterior and lateral walls where the estimation was performed longitudinally. The radial, circumferential and longitudinal directions are depicted in **Figure 5-1**. After a wall region is electrically activated to undergo systole, it is expected to transition from radial thinning to thickening and from longitudinal lengthening to shortening. This is depicted in Figure 2: 15 ms after pacing (**Figure 5-4**A), the tissue has not started to contract yet due to the electromechanical delay existing between the onset of the action potential and the contraction at the cellular level (Bers, 2002; Cordeiro et al., 2004). At 30 ms, thickening near the pacing lead (**Figure 5-4**B) in the basal region of the lateral wall is observed while the other regions of the ventricles undergo negligible strain variations. This initial thickening region then extends (**Figure 5-4**C) and reaches the apical region of the lateral, septal, anterior and right-ventricular walls as well as the basal region of the anterior wall (**Figure 5-4**D). Note that in the apical region of the anterior and lateral walls, activation resulted in shortening (blue). At 120 ms, both ventricles were activated except for a small region in the anterior and posterior walls near the base.

Isochronal maps were obtained by defining the onset of the EW as the first time-point following the Q-wave, at which the temporal strain profile crosses zero. **Figure 5-5** shows such maps during four different pacing schemes in both anterior and posterior views, i.e., LVb (**Figure 5-5**A), LVa (**Figure 5-5**B), LVar (**Figure 5-5**C) and RVa (**Figure 5-5**D). In three cases (**Figure 5-5**A,B,D), we identified a unique origin of the EW, i.e., the region with the shortest zero-crossing time. This region coincided with the position of the pacing lead. When pacing from the apical region of the antero-lateral wall (**Figure 5-5**C), the pacing lead was located in the apical

region between the two planes. A clear propagation of the EW emanating from the location of the lead was depicted. The same results were obtained in two separate animal cases (**Figure 5-5**A,B,D and **Figure 5-5**C, respectively) indicating preliminary reproducibility of the method.

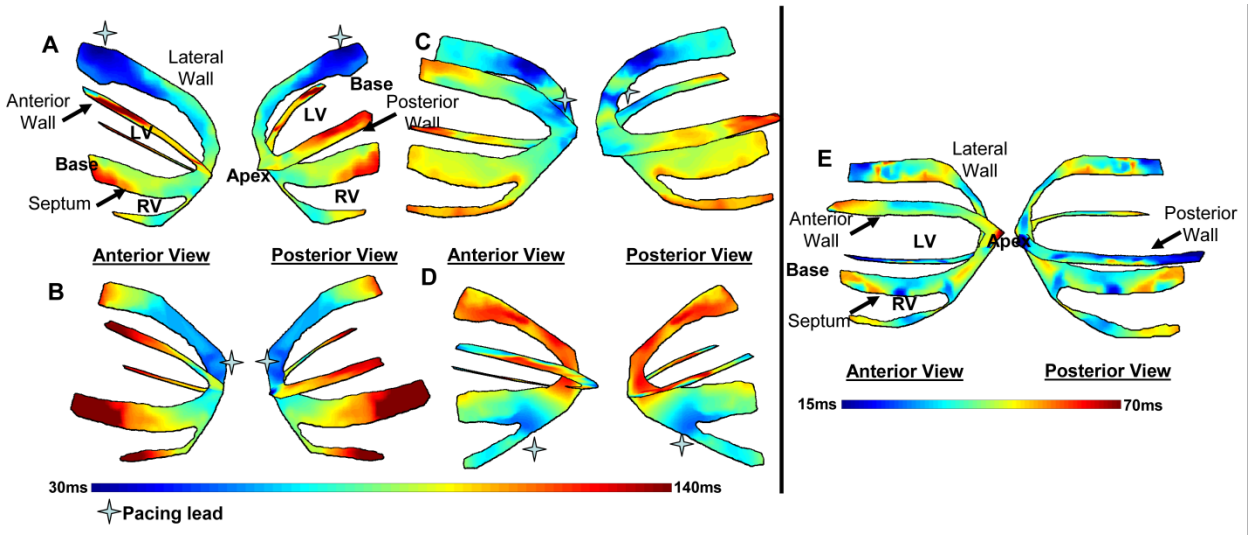

Figure 5-5 Isochrones showing the activation sequence under different pacing protocols. Arrow indicates the pacing origin. (A) Pacing from the basal region of the lateral wall. (B) Pacing from the apex. (C) Pacing from the apical region of the lateral wall. (D) Pacing from the apical region of the right-ventricular wall. (E) Isochrones showing the EW activation sequence during sinus rhythm. The activation sequence exhibits early activation at the median level and late activation at the basal and apical levels. Activation of the right ventricular wall occurred after the activation of the septal and lateral walls. (Provost, Lee, et al., 2011a)

During sinus rhythm, the natural pacemaker is the sinus node, located in the right atrium. Signals are generated spontaneously at the node, travel through the atrium (during the P-wave), to the atrio-ventricular node, the bundle of His and finally the Purkinje fiber network and the ventricular myocardium (during the QRS complex). Complex activation patterns are expected when imaging the ventricles, since activation will originate from multiple locations following the Purkinje fiber network. **Figure 5-5**E shows the isochronal representation of the EW in the left and right ventricles during sinus rhythm. Early activation halfway between the

apex and base, and late activation at the basal and apical levels were observed. Activation of the right-ventricular wall occurred after activation of the septal and lateral walls in both cases. Therefore, the EWI isochrones during sinus rhythm exhibited multiple origins of propagation, i.e., early activated regions, rather than a unique origin observed when pacing from a single lead.

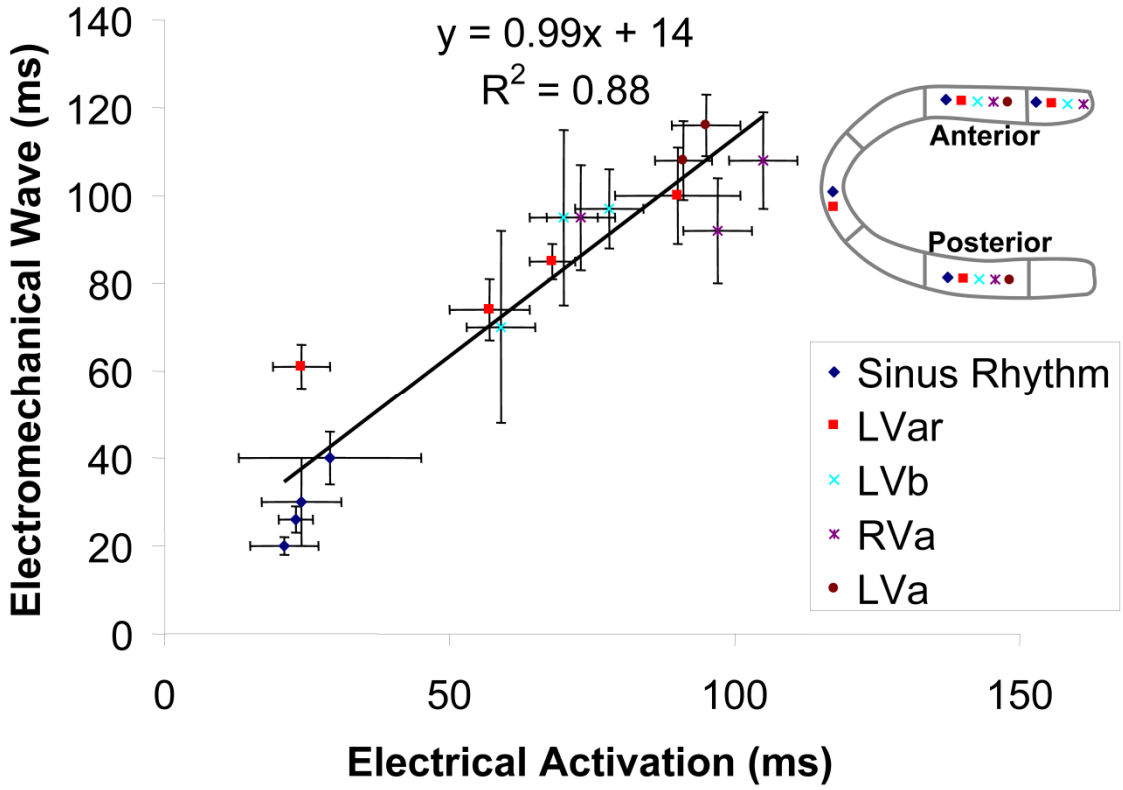

Figure 5-6 Electrical and electromechanical activation times during the four pacing protocols and sinus rhythm in four different heart segments in the posterior and anterior walls, as indicated in the legend. A strong correlation was observed, with a slope of 0.99. (Provost, Lee, et al., 2011a)

We then compared the EW against the electrical activation, the latter being measured using implanted bipolar electrodes. Four recording electrodes were placed in the two-chamber view plane for that purpose as indicated on **Figure 5-1**. **Figure 5-6** shows the timings of electrical activation and the corresponding EW onset time. The EW onset time was obtained by

averaging the isochrones within the echocardiographic segments (mean ± spatial standard deviation within a cardiac segment). The electrical activation times were averaged over ten cardiac cycles (mean ± temporal standard deviation). A linear relationship between the EW onset and the electrical activation time was found (**Figure 5-6**) in all four pacing cases and during sinus rhythm with a slope of 0.99 ± 0.1 (R^2 = 0.88, $p < 10^{-7}$) and an intercept of 14 ± 7 ms (p=0.06).

To increase the electrical mapping resolution, a basket catheter was used in two other dogs. The wide beam sequence was used in one open-chest animal and correlated with the electrical activation sequence during pacing from the apical region of the lateral wall. The heart was imaged in the four-chamber view with the ultrasound probe positioned parasternally. EWI shows activation (red) originating from the apical region of the lateral wall (**Figure 5-7**A,B), followed by activation of the right-ventricular wall (**Figure 5-7**C) and finally by the septum (**Figure 5-7**D). The corresponding EWI isochrones reflect this behavior (**Figure 5-7**E). The EW maps and the electrical activation obtained using the basket catheter (**Figure 5-7**F) were highly correlated (**Figure 5-7**G). A slope of 1.31 (R^2 = 0.99) was obtained between the electrical activation and the EW onset.

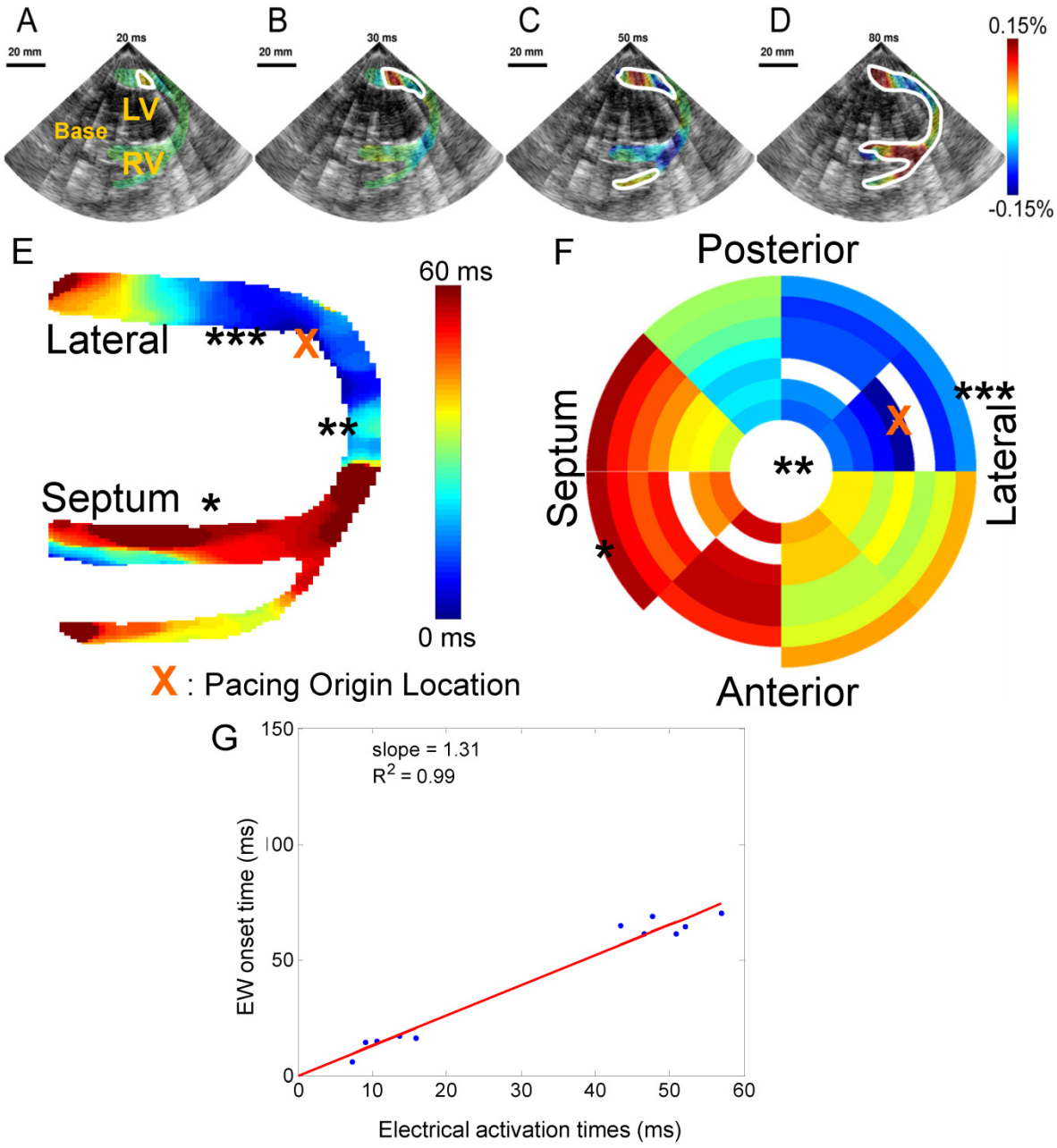

Figure 5-7 The EW in a canine during pacing from the apical region of the lateral wall. (A) Activation (red) originates from the endocardium and (B) propagates both towards the apex (in blue, due to the orientation of the probe) and the base. (C) The RV wall is then activated, (D) followed by the septum. (E) Corresponding EWI isochrones. (F) Electrical isochrones, depicting the activation on the 3-D endocardial surface of the heart. The symbols *,**,*** indicate corresponding regions between (E) and (F). (G) Using the electrical activation times measured using the basket catheter, the electrical activation times can be compared to the EW onset time. Since no ECG was acquired during this acquisition, the intercept was fixed to 0 ms. (Provost, Nguyen, et al., 2011)

Finally, we imaged another open-chest dog during pacing from a pair of electrodes of the basket catheter in four views, i.e., the two-chamber, the four-chamber, the three-chamber views and in a fourth view located between the two- and four- chamber views. This configuration allows the alignment of two splines with each view, and up to 56 electrical recordings; in the case of **Figure 5-8**, only 28 electrodes measurements are shown because of limited contact with the cardiac muscle, and, more importantly, because the basket catheter had a manufacturing defect that prevented measurement from 16 electrodes. Additionally, the papillary muscle on the lateral wall prevented the measurements of electrograms on the lateral wall in the four-chamber view. To perform co-registration between EWI and the basket catheter measurements, the earliest activation in both cases were aligned. The results are shown in **Figure 5-8**. Propagation from the pacing origin could be clearly mapped with EWI (**Figure 5-8**A) and with electrical mapping (**Figure 5-8**B). Both the electrical and the electromechanical activations followed similar propagation patterns. Indeed, when compared quantitatively, a large R^2 value (R^2 = 0.75) was obtained with a slope of 1.8 and an eEMD of 10.43 ms (**Figure 5-8**C).

5.2.3 Discussion

The objective in this study was to determine whether the EW could accurately depict electrical events in the normal ventricles. EWI with the automated composite technique (ACT) was performed in canine hearts during four distinct pacing protocols and sinus rhythm. Isochronal maps of the EW onset were generated and the earliest activation region was found to be highly correlated with the pacing site location. Electrodes were also implanted in the heart, allowing simultaneous measurements of the electrical activation times in selected echocardiographic

segments of the heart. A linear relationship was found between the electrical activation times and the EW onset, thereby showing that at the scale of the cardiac segments, the EW follows the electrical activation sequence.

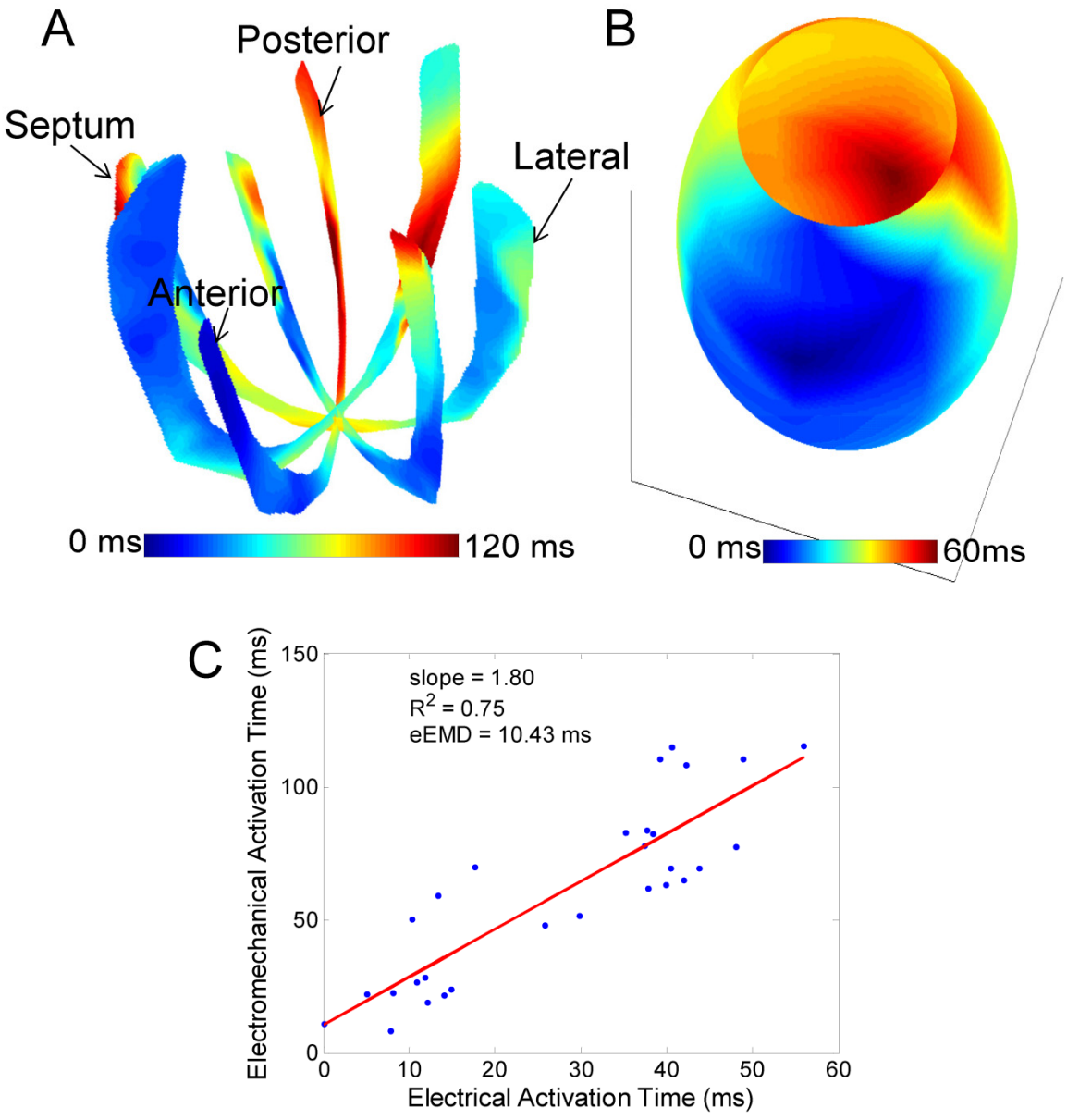

Figure 5-8 Simultaneous EWI and electrical mapping using a basket catheter in four parasternal views obtained in an open-chest canine. (A) EWI isochrones. The earliest activation occurs near the base of the anterior wall. (B) Interpolated electrical activation times. (C) Comparison between the electrical and electromechanical activation times.

The validation of the link between the EW and the electrical activation sequence in canines was two-fold. First, the localization of the earliest activation time in the EWI isochrones was highly correlated with the pacing site, thus allowing the noninvasive identification of the pacing lead location. For instance, right-ventricular pacing (**Figure 5-5**D) could easily be distinguished from left-ventricular free-wall pacing, apical pacing or sinus rhythm. Moreover, the EWI isochrones obtained during sinus rhythm (**Figure 5-5**E) were in agreement with maps previously reported in the literature obtained using electrography (Scher and Young, 1956; Durrer et al., 1970; Sengupta et al., 2008). Second, the electrical activation times and the EWI isochrones where highly correlated, with a slope of 0.99 (**Figure 5-6**). Comparing such maps constitutes, however, a significant challenge. The electrodes typically affect both the mechanical and electrical behavior of the heart muscle, and can also generate artifacts on the ultrasound image. To circumvent this issue in this study, the EWI image plane was selected in the vicinity of the plane defined by the electrode locations without being affected by the aforementioned artifacts. This approach showed that, at least on the scale of the heart segments in the regions studied, EWI reflects the electrical activity with good accuracy. The observed propagation from the epicardium to the endocardium when pacing, e.g. **Figure 5-5**A-C, indicates that EWI also provides information about the transmural electrical activity, which was also confirmed in simulations (Section 5.3). However, in sinus rhythm, activation from endocardium to epicardium, which is expected, was not observed everywhere in the heart. This could be explained by the limited information obtained through 2-D observation of an inherently 3-D phenomenon such as the cardiac electrical activation in combination with the fact that strain estimation at the boundary of the heart wall is more susceptible to noise.

EWI was then obtained using temporally unequispaced acquisition sequence (TUAS)-based wide-beams parallel acquisition (Section 4.4) and was found to be highly correlated with electrode measurements made using a basket catheter. These results are in good agreement with those found with ACT and sutured electrodes (**Figure 5-6**), indicating that the correlation between the EW and the electrical activation sequence is maintained even in situations where wide beams, which are more prone to image artifacts due to the large transmit focus used, are used in the presence of a basket catheter.

Finally, a high resolution comparison of EWI with a virtual-source sequence was performed, resulting in similar results, i.e., a strong linear correlation between the electrical and electromechanical activation times with a slope of 1.8. However, this relationship was obtained under the assumption that the ultrasound views and the splines pairs were perfectly aligned, and that the angle between splines remained constant despite the complex endocardial anatomy; this is not generally the case. Indeed, since we acquired four views, it was possible to linearly interpolate the electromechanical activation times and apply a rotation corresponding to one third of the angle separating two splines and achieve an R^2 of 0.85 and a slope of 1.4, which are closer to simulation results (Section 5.3). Remarkably, for larger rotations, R decreased rapidly, reinforcing the validity of the linear regression. This observation also stresses the need for better co-registration strategies, for example by using 3-D ultrasound to locate the splines and electrodes.

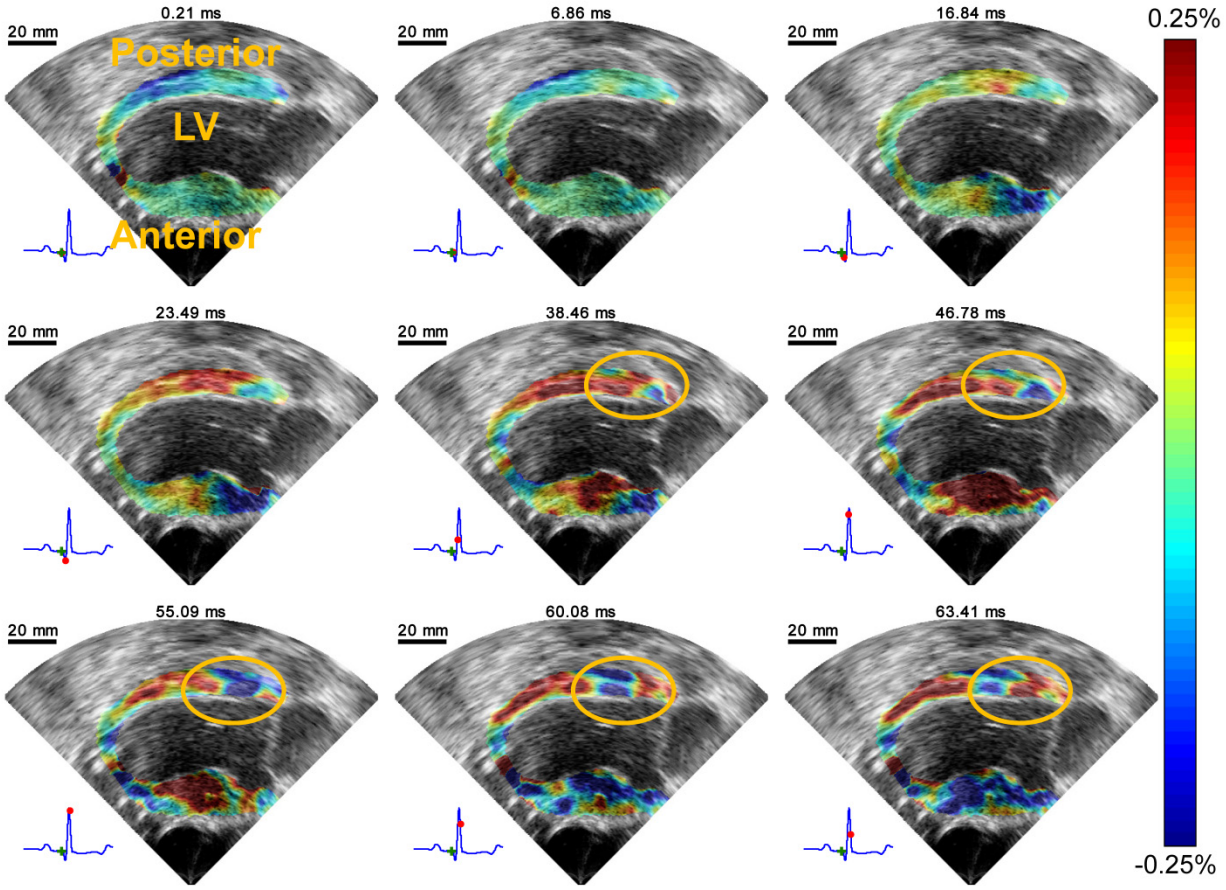

Figure 5-9 Propagation of the EW followed by the propagation of an oscillating, mechanical wave generated at the time of the mitral valve closure (circled) in an open-chest, normal canine during sinus rhythm in the two-chamber view. (Provost et al., 2010)

.

A number of phenomena occur in the heart when it undergoes electrical activation. For example, the valves can open and close and generate waves in the myocardium that could, potentially, alter the EW measurements. Oscillations, for example, can become visible in the strain maps as the mitral valve closes (**Figure 5-9**). Although this phenomenon has already been documented (Kanai et al., 1993; Støylen et al., 2001; Sengupta et al., 2007; Remme et al., 2008), the techniques developed here for EWI could constitute an interesting tool for its visualization and quantification. This phenomenon may, however, occur prior to the complete mechanical

activation of the entire ventricle, thereby also reducing the quality of the correlation between the EW and the electrical activation pattern. Appropriate modeling may provide a correction, e.g., by applying a band-pass filter corresponding to the valve wave bandwidth.

These results confirm that EWI, with any of the approaches developed (ACT, TUAS, or parallel beamforming) can be used to map electrical events in the normal ventricles during sinus rhythm and pacing. However, these studies do not validate the capability of EWI to map the electrical activation transmurally and are limited to parasternal views. In the following section, these two issues are investigated using simulations.

5.3 Simulations

5.3.1 Methods

Due to the limitations in current experimental techniques for mapping the 3-D electrical activation sequence with high spatiotemporal resolution, an anatomically realistic modeling approach to cardiac function appears as an attractive alternative in providing the 3-D electrical activation sequence in the ventricles. Our collaborators developed a high-resolution dynamic model of coupled cardiac electromechanics in the rabbit heart (Gurev, Constantino, et al., 2010) and used it to ascertain the mechanisms of spontaneously induced arrhythmias in acute regional ischemia (Jie et al., 2010). The model was extended to the canine heart, where the geometry and structure of the canine heart was reconstructed from MRI and diffusion tensor (DT) MRI scans (Gurev, Lee, et al., 2010) and validated in part with the results of this study in which we used this novel electromechanics model of the canine heart for the first time and

applied it, after optimizing it, to fully assess the utility of EWI in mapping the electrical activation sequence in the canine ventricles.

To achieve this goal, the EW in the model of the normal canine ventricles was simulated and compared to the results of the *in-vivo* experimental EW in one canine from Section 5.2. Once the match between simulated and experimental EWs was obtained and the predictive capabilities of the canine electromechanics model were established, the EW was compared to the electrical activation sequence obtained from the model, providing the desired relationship between the EW and the 3-D electrical activation maps in the canine ventricles, and thus assessing the utility of EWI in mapping the electrical activation. The isochrones were generated automatically to limit observer bias: To generate the isochrones, zero-crossing points were identified in three regions where the ultrasound beam was best aligned with either the radial or the longitudinal direction of the lateral, septal and RV walls. Time delays between these regions and the nearest neighboring pixels were then obtained via normalized cross-correlation. The procedure was repeated using these neighboring pixels until the time of electromechanical activation was mapped throughout the entire echocardiographic view.

The 3-D electromechanical model of the canine ventricles has previously been described in detail (Gurev, Lee, et al., 2010). Briefly, the electromechanical model of the normal canine heart was composed of two main components, an electrical component and a mechanics component (**Figure 5-10**D). The components represented two coupled finite-element models, both based on canine ventricular geometry and structure reconstructed from ex-vivo cardiac MR and DTMR

imaging datasets. Both the electrical and the mechanical component were biophysically detailed, incorporating canine specific ionic and myofilament models. The mechanical and electrical components were coupled weakly to minimize computations. Finally, the electromechanical model was coupled to a model of the circulatory system representing the systemic and pulmonary circulations (Gurev, Lee, et al., 2010). For the present application of the canine electromechanics model, the circulatory system model was modified to simulate backward flow from the left ventricle (LV) to the atrium in the normal canine heart (Otsuji et al., 1997), by delaying mitral valve closing for 100 ms after the pacing stimuli and by increasing the mitral valve resistance by a factor of 30. The computational mesh for the electrical component of the model consisted of linear mixed-type finite elements (1637744 elements and ~1 million nodes). The mechanics mesh was composed of non-linear, hexahedral, Hermite-based finite elements (566 elements and 1060 nodes). The generation of active stress in the myocyte was represented by active tension in the fiber and transverse to the fiber directions, calculated from the model of the cardiac myofilament.

Consistent with the goal of this study, we compared the EW in experiments and simulations. To generate the model EW, the inter-frame axial strains resulting from an activation elicited from the same pacing site as in the experiment were calculated. For this purpose, the output of the mechanics component of the canine electromechanical model, i.e., the nodes' position, was used to obtain maps of cumulative strain over time. The simulated inter-frame strains and EWI ciné-loop (**Figure 5-10**E) were obtained by computing the temporal derivative of the cumulative strains. Simulated EWI isochrones were obtained in the same fashion as the experimental ones

(**Figure 5-10**F). Since the simulations were based on a different canine heart than the one used in experiments, direct, pixel-to-pixel comparisons could not be performed. Instead, the fraction of the echocardiographic view of the ventricles, through which the EW had propagated, was plotted as a function of time. These fractions, as obtained from experiment and simulation, were then compared directly for the three pacing schemes.

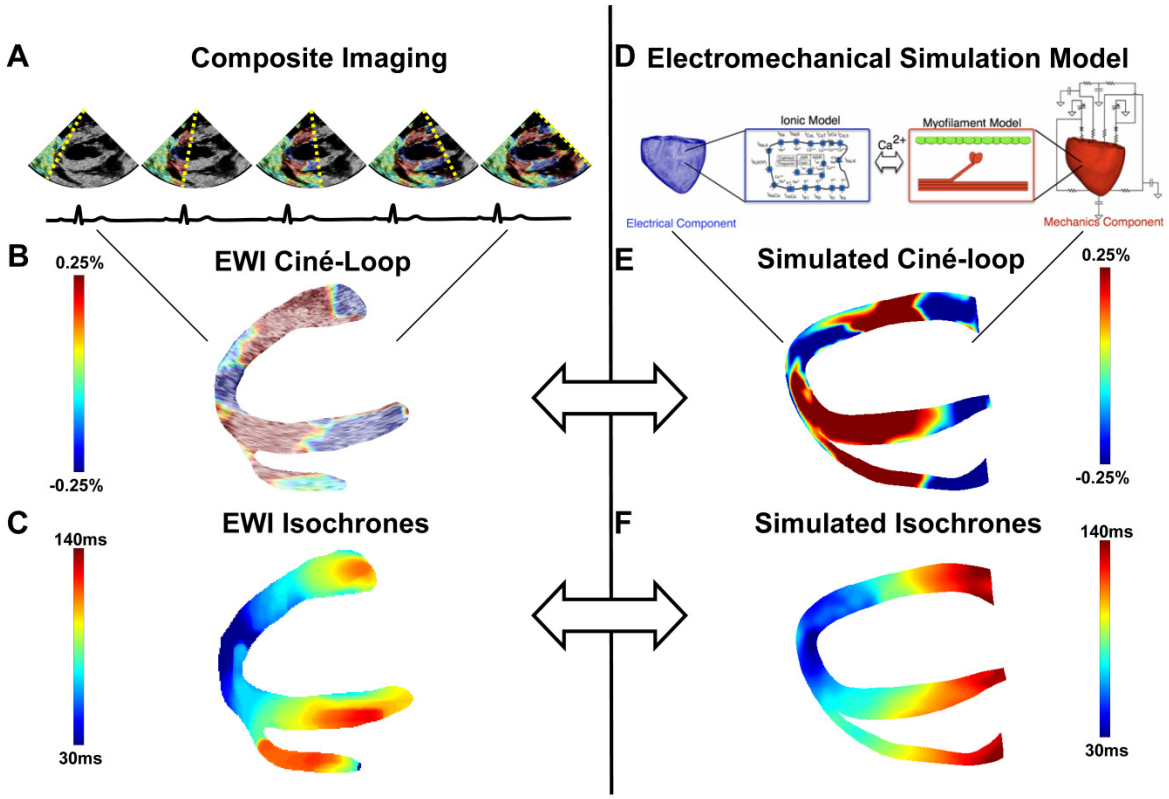

Figure 5-10 (A) ACT. (B) Strain-overlayed, segmented ciné-loop of the heart depicting the propagation of the EW. (C) EWI isochrones obtained from the interpolation of manually selected zero-crossing points of hundreds of locations in the ventricle. (D) Cardiac electromechanics model. (E) Simulated EWI ciné-loop. (F) Simulated EW isochrones. (Provost, Gurev, et al., 2011)

5.3.2 Results

Figure 5-11A and B depict the experimental and simulated EW maps during pacing from the basal region of the lateral wall. Blue and red indicate local compression and expansion of the tissue, respectively, in the direction of the ultrasound beam (**Figure 5-10**A). In the view presented here, activation results in expansion (red) throughout the ventricles with the exception of the apical region, which undergoes local compression (blue). In both experiments and simulations, the EW emerged from the basal region of the lateral wall (**Figure 5-11**A,B). The EW then propagated toward the apex, the septum and the RV wall. **Figure 5-11**C shows representative curves of the inter-frame strains over time in the lateral and septal walls during LVb pacing for both experiments and simulations. While simulated and experimental curves are not identical, they exhibit similar qualitative trends. More specifically, the inter-frame strains are negative and slowly varying before a sudden increase amounting to a few tenths of a percent. **Figure 5-11**D and E present the EW in experiments and simulations for pacing from the LV apex. In both experiments and simulations, the EW originated at the apex and propagated towards the base in the three walls. **Figure 5-11**F shows a comparison between simulated and experimental inter-frame strains over time at one location in the lateral wall and in the septum. In both simulations and experiments, slowly varying negative inter-frame strains are observed before a steep increase up to a maximum value of approximately 0.1%. After reaching maximum, the inter-frame strains decrease while remaining positive. **Figure 5-11**G and H shows the comparison between experimental and simulation EW when pacing from the RV apex. In this case (**Figure 5-11**G,H), the EW emerged from the RV apex and propagated towards the base and the lateral wall. **Figure 5-11**I shows a comparison between simulated and

experimental inter-frame strains. In both simulations and experiments, slowly varying negative inter-frame strains are observed, followed by a sudden increase. The inter-frame strains then reach a maximum at approximately 0.1%, followed by a decrease to approximately 0.025%.

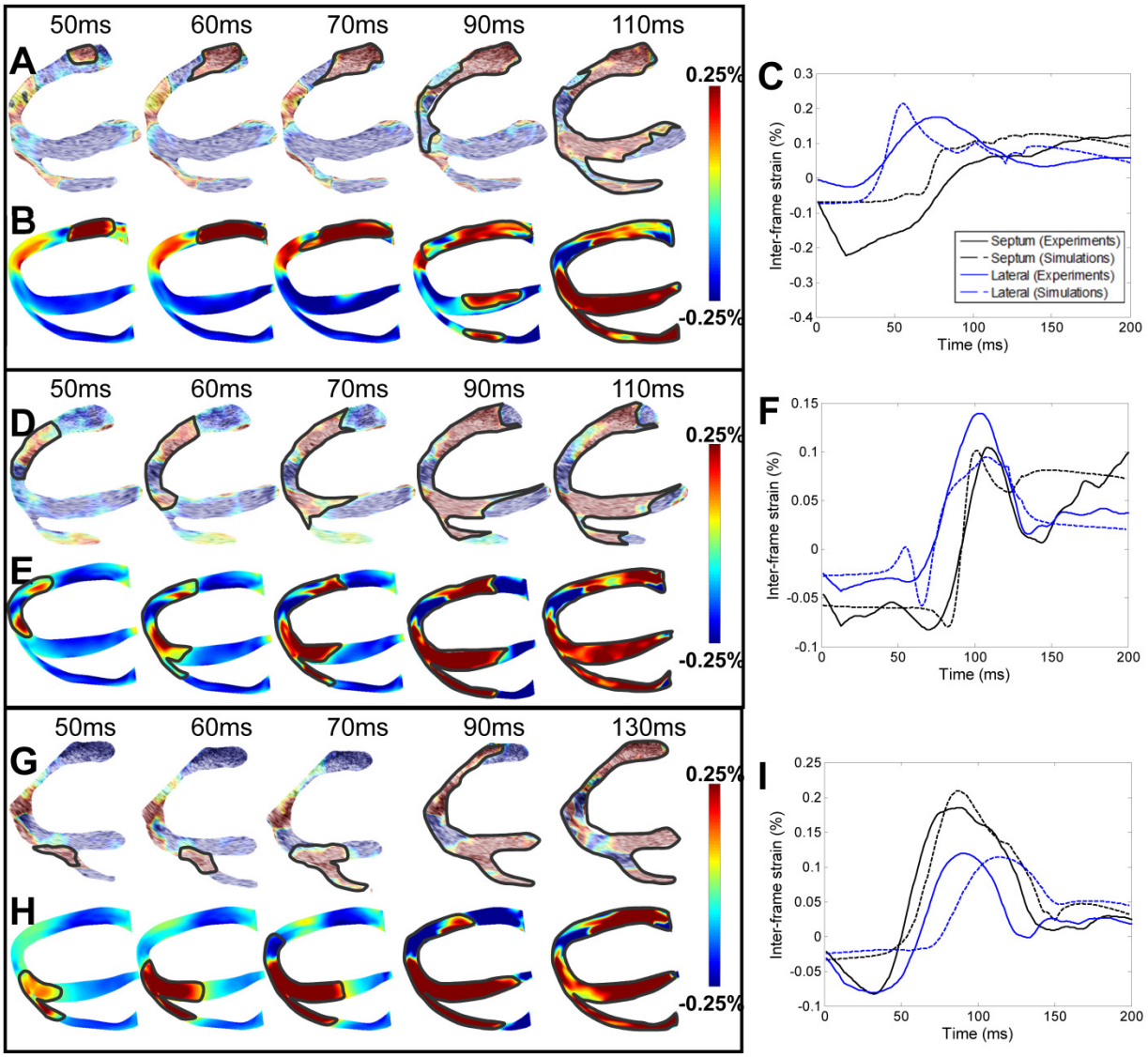

Figure 5-11 Inter-frame strains associated with the EW during the three pacing protocols. *LVb pacing*: (A) Experimental EW, (B) Simulated EW and (C) Comparative graph over time. *LVa pacing*: (D) Experimental EW, (E) Simulated EW and (F) Comparative graph over time. *RVa pacing*: (G) Experimental EW, (H) Simulated EW and (I) Comparative graph over time. (Provost, Gurev, et al., 2011)

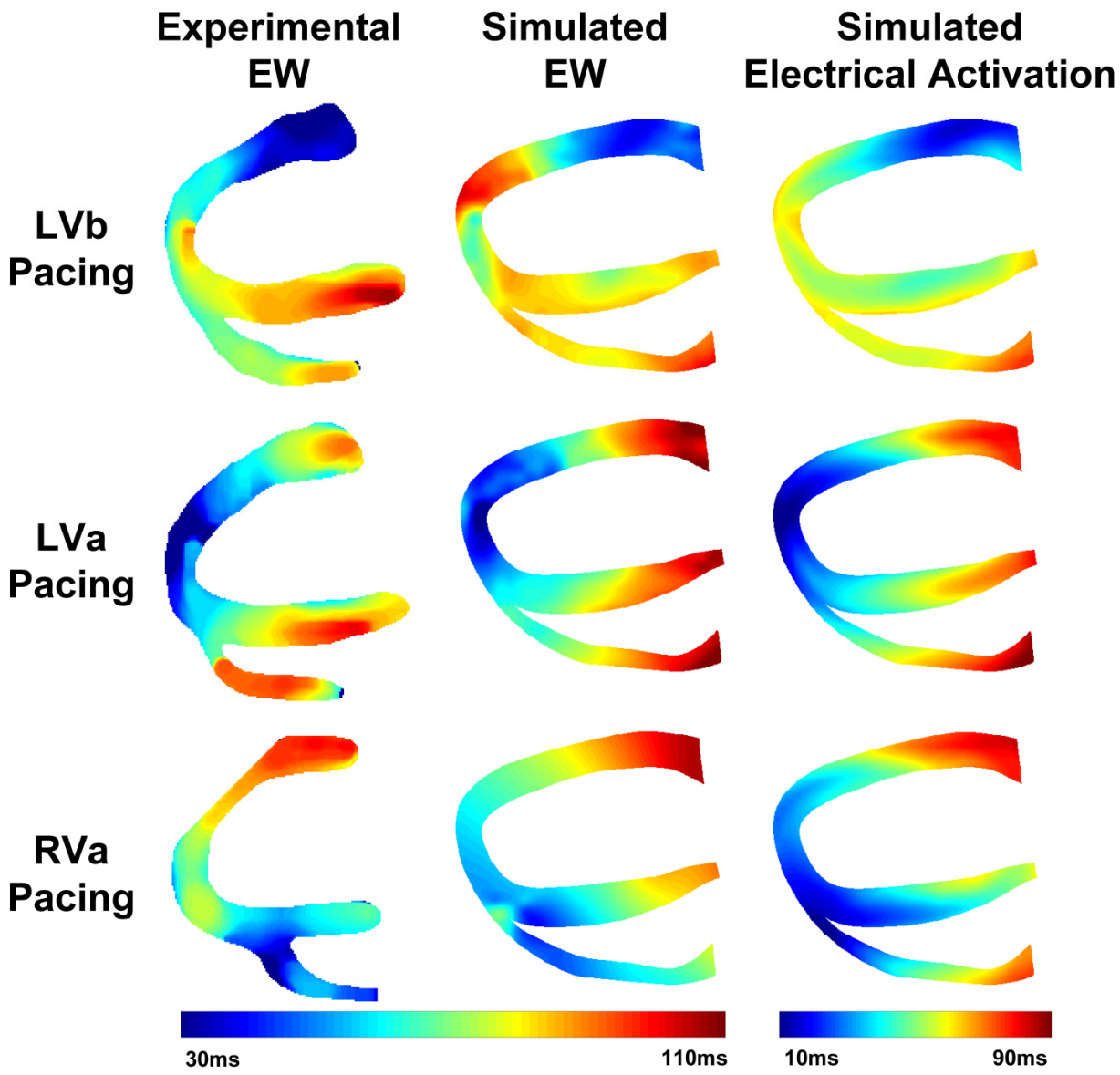

Figure 5-12 Experimental and simulated electromechanical activation isochrones and simulated electrical activation isochrones during the three pacing protocols. (Provost, Gurev, et al., 2011)

Figure 5-12 shows the isochrones of electromechanical activation in experiments, of electromechanical activation in simulations and of electrical activation in simulations during the three pacing schemes. To further quantify the agreement between simulations and

experiments, the isochronal representation of the EW was used to calculate, and then plot as a function of time, the electromechanically activated myocardial fraction in the echocardiographic view (**Figure 5-13**A). The time delay between simulations and experiments for a given fraction and a given pacing schemes was then computed. For LVb, LVa and RVa pacing, these time delays were on average (± standard deviation): 5.0 ± 4.3 ms, -2.5 ± 4.2 ms, and -4.9 ± 4.5 ms, respectively. To quantify the correlation between experiments and simulations one can also plot the simulated against the experimental fractions were plotted (**Figure 5-13**B). In such a graph, an ideal experimental reproduction would result in a slope of 1 (gray line). For LVb, LVa and RVa pacing, the regression slopes obtained through least-squares fitting (not shown) were 1.17 (R^2 = 0.96), 0.86 (R^2 = 0.99) and 0.89 (R^2 = 0.99), respectively.

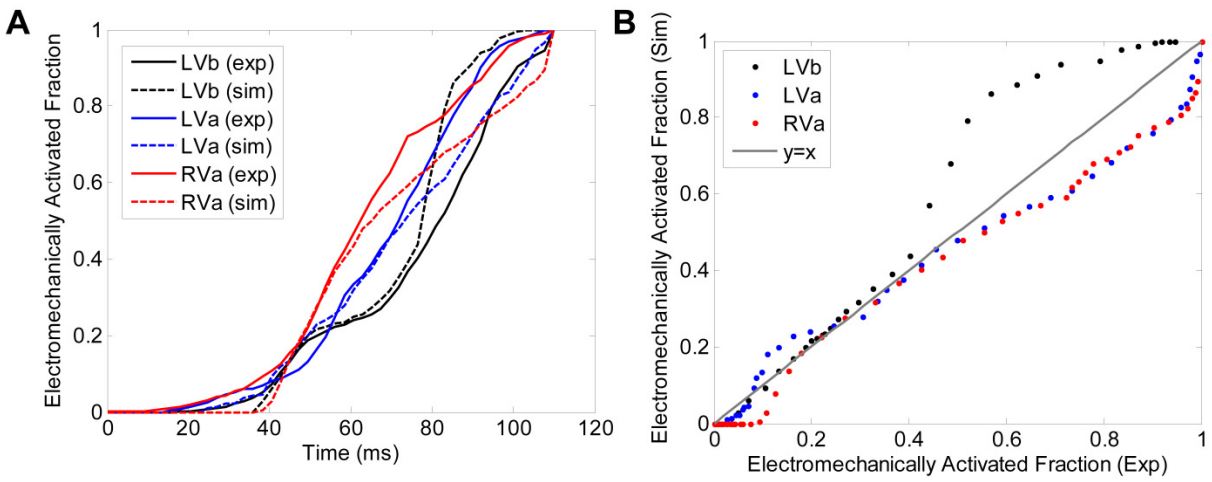

Figure 5-13 Comparisons between experiments and simulations. (A) Fraction of the myocardium in the echocardiographic view that underwent EW, plotted as a function of time, in experiments and simulations. (B) Electromechanically activated myocardial fraction in the echocardiographic view in simulations, plotted as a function of the same in experiments. (Provost, Gurev, et al., 2011)

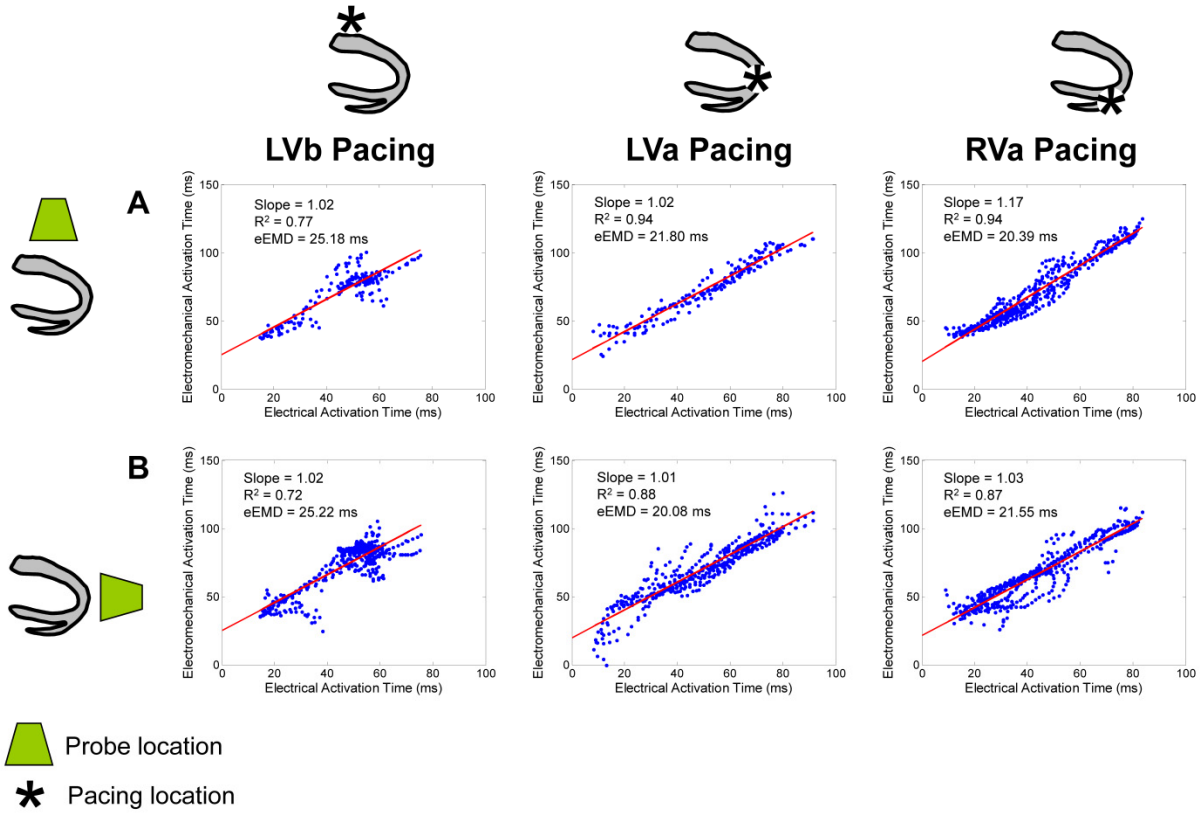

Figure 5-14 Correlation between the electrical activation time and the electromechanical activation time when the probe is located (A) parasternally and (B) apically. eEMD corresponds to the intercept of the regression fit. (Provost, Gurev, et al., 2011)

The results above indicate that the electromechanics model can reproduce the behavior of the EW during different pacing protocols. Simulations were then conducted to quantify the precision with which EWI can map electrical activation. **Figure 5-14** shows the correlation between the simulated electrical and simulated electromechanical activations during the three pacing protocols and for the two different imaging angles commonly used clinically: parasternal (**Figure 5-14**A) and apical (**Figure 5-14**B) views. In all six cases, a linear relationship was established, with slopes ranging between 1.01 and 1.17 ($0.72 < R^2 < 0.94$) and an effective electromechanical delay (eEMD), corresponding to the intercept, varying between 20.08 and

25.22 ms. Moreover, the distance between the location of the earliest electromechanical activation site and the location of the earliest electrical activation site was computed for each pacing scheme and both views. A precision in the earliest electrical activation site localization of 4.9 ± 3.3 mm was found.

5.3.3 Discussion

In this study, a realistic canine cardiac electromechanics model was used to reproduce the experimentally obtained EW from three different pacing sites to better understand the relationship between EW and the electrical activation sequence in the ventricles. Current experimental methods do not allow mapping of both the transmural electrical activation sequence and the EW simultaneously and at high spatial resolution. Since the strains associated with the EW are minute, any insertion of plunge needles to map the activation sequence would inadvertently alter the normal EW. Therefore, a unique and important avenue available for comparing the EW with the electrical activation sequence is the use of realistic electromechanical simulations. This methodology establishes a framework that can be used to further evaluate the clinical potential of EWI as a useful tool for the diagnosis as well as treatment planning and assessment of cardiac rhythm dysfunction.

The simulation model was capable of reproducing the realistic EW characteristics observed in the canine experiments, such as spatial propagation (**Figure 5-11**), temporal shape (**Figure 5-11**), isochrones (**Figure 5-12**), and activated fraction of the ventricles (**Figure 5-13**). Since different hearts were used in simulations and experiments, a perfect reproduction of the EW observed in experiments was not expected. Even under such imperfect conditions, a good

match was achieved: a regression slope varying between 0.86 and 1.17 ($R^2 > 0.96$) was found between experimental and simulated electromechanically activated myocardial fractions. The model of EW was then used to quantify the relationship between the electrical activation and the EW sequence in the normal canine heart. These were in excellent agreement for all pacing protocols and for two different imaging angles. The relationship between the electrical activation and the EW onset was found to be linear with a slope of 1.01 to 1.17 and with an intercept of 20.08 to 25.22 ms. These results are in agreement with published results, although the methods and the strain tensor components used were different: Badke et al. (Badke et al., 1980) found, using implanted beads, a slope of 1.1 with an intercept of 17 ms. Using MR tagging, Wyman et al. (Wyman et al., 1999) found a slope of 1.06 with an intercept of 8.4 ms, and Faris et al. (Faris et al., 2003) found a slope between 0.87 and 1.05 and an intercept between 19.4 ms and 37 ms. The slope between the electrical and electromechanical activations was closer to 1 unlike in previous modeling results (Gurev, Constantino, et al., 2010), which used a different definition of the electromechanical activation (based on the fiber strain) and did not include the backward flow, i.e., flow from the LV to the left atrium. The linear relationship indicates a one-to-one correspondence between the electrical activation sequences and the EW. A slope higher than one indicates that the delay between the local electrical activation and the local onset of mechanical contraction increased over time (i.e., with increasing distance away from the pacing site). In other words, EWI provided an accurate representation of the electrical activation sequence but shifted in time. While the relationship between the electrical and electromechanical activations remained linear with high correlation coefficients for all pacing schemes, EWI during LVa and RVa pacing followed more closely the

electrical activation sequence than during LVb pacing (**Figure 5-14**). Similarly, while both apical and parasternal views provided high correlation coefficients, the parasternal view systematically provided a higher correlation coefficient between the electrical and electromechanical activations during the three different pacing schemes. These results indicate that EWI could be used for mapping of electrical activation in normal hearts with different imaging angles and for different pacing protocols. Finally, EWI was also found capable of identifying the region of earliest electrical activation with an accuracy of approximately 5 mm.

In this study, the EW was reproduced accurately with the realistic cardiac electromechanics model, indicating that the model framework is capable of faithfully representing the physiology of cardiac electromechanics and that it could thus be used to test new hypotheses. Furthermore, a strongly correlated, linear relationship was found between the electrical activation sequence and the EW onset in the normal heart, ascertaining the potential of EWI to noninvasively map the electrical activation sequence of the heart *in vivo*.

5.4 Conclusion

In this chapter, the correlation between the electrical and electromechanical activations was demonstrated using three different image formation strategies (ACT, TUAS, and parallel beamforming) and three different electrical activation mapping techniques (sutured electrodes, basket catheter and simulations). More specifically, the relationship between the electrical and electromechanical activations is approximately linear with large R^2 value and with a slope of between 0.99 and 1.4, in accordance with previous results obtained with different means in the literature (Badke et al., 1980; Wyman et al., 1999; Faris et al., 2003). Additionally, we demonstrated that this relationship is maintained transmurally, and with a changing

insonification angle. This last result is important, since it indicates that EWI could be applied noninvasively in humans in conventional apical views. However, before EWI can be applied in humans, it is important to characterize the relationship between the electrical and electromechanical activations of the heart in the presence of disease and validate that EWI can be performed in a closed-chest setting. This is done in the next chapter.

Chapter 6 Electromechanical Wave and Electrical Activation in Diseased Hearts

6.1 Introduction

In Chapter 5, we demonstrated the existence of a strong correlation between the electrical and electromechanical activations in normal hearts, both during pacing and sinus rhythm. This indicates the potential of Electromechanical Wave Imaging (EWI) to act as a noninvasive surrogate for electrical mapping in the clinic, under the assumption that this electromechanical relationship is maintained in the presence of disease, e.g., in patients with arrhythmia. In this chapter, four conditions that are clinically relevant to heart failure and cardiac resynchronization therapy (CRT) during heart failure are studied. More specifically, we study the electromechanical coupling occurring during different levels of ischemia, left bundle branch block (LBBB), fibrillation, and atrio-ventricular block (Mosterd et al., 1999; Epstein et al., 2008). We aim at determining if 1) the electromechanical coupling is maintained in the presence of disease, 2) EWI can detect and characterize the effect of disease on the electromechanical activation, and 3) EWI has the potential to be used for diagnosis.

Ischemia occurs when insufficient blood flow perfuses the myocardium. A typical occurrence of this condition is the partial or complete blockage of a coronary artery. Coronary heart disease is responsible for 1 of every 6 deaths in the United States (Roger et al., 2011). Currently, the echocardiographic stress test may allow detection of early ischemia. However, such tests are limited by low image quality caused by fast heart rates, potential contrast administration requirements, and the limited time available to acquire an image. Moreover, for patients who cannot perform the stress test, drugs such as dobutamine may need to be systemically administered. In a related study (Lee et al., 2011), we found that ischemia cannot be detected

on the B-mode images before an obstruction of 80% flow is reached, even in the excellent imaging conditions in an open-chest setting. In this chapter, we demonstrate that EWI can detect and map ischemic regions when coronary flow is obstructed at 60% and above by detecting regions in which the electromechanical wave (EW) doesn't propagate (Section 6.2).

LBBB is a condition in which the conduction through the Purkinje fiber network connecting the atrio-ventricular node to the left ventricle (LV) (i.e., the left bundle branch) is impeded. During LBBB, the electrical activation of the ventricles becomes dyssynchronous: the right ventricle (RV) is activated rapidly via the Purkinje network, while the LV is activated via the cell-to-cell myocardial conduction system. One third of subjects with heart failure also have dyssynchrony due to LBBB (Clark et al., 2008). CRT, which uses biventricular pacing to correct this dyssynchrony, is an evolving therapy that has led to lower mortality and improved clinical status (Cleland et al., 2005). However, approximately 30% of subjects show no functional benefit after implantation (Gregoratos et al., 2002). This limited success likely reflects both an incomplete understanding of basic mechanisms as well as inadequate tools for optimizing the use and programming of existing pacing therapies. In this section, we aim at demonstrating that EWI can detect and characterize LBBB in canines *in vivo*.

Fibrillation refers to a state of rapid, uncoordinated contractions of the upper or lower chambers of the heart. The number of individuals with atrial fibrillation (AF) in the United States is expected to reach 12 million by 2050 (Lloyd-Jones et al., 2009). AF is the most common arrhythmia (Fuster et al., 2006), is responsible for 15-20% of strokes (Lloyd-Jones et al., 2009),

and costs $6.65 billion per year in treatment (Coyne et al. 2006). Ventricular fibrillation, which is studied in this chapter, is associated with sudden cardiac death, a leading cause of death in the United States. Developing a technology to map ventricular fibrillation transmurally, and to better understand the electromechanical mechanisms at play could help in defining risk factors and improve preventive treatments such as implantable cardioverter-defibrillators.

Atrio-ventricular dissociation is a condition in which the atria and ventricles do not activate in a synchronous fashion but contract and are electrically activated independently of each other (Harrigan et al., 2001). Atrio-ventricular dissociation can be caused by atrio-ventricular block and sometimes can be induced on purpose in patients, via the ablation of the atrio-ventricular junction, for ventricular rate control in specific cases (Gallagher et al., 1982; Betts, 2008). For the purpose of this dissertation, the objective was to study, with EWI, a condition that is non-periodic and commonly found in heart failure. Additionally, these experiments were performed in an experimental setup as close as possible to the clinical environment, i.e., by imaging closed-chest, conscious canines.

6.2 Ischemia

6.2.1 Methods

In this study approved by the Institutional Animal Care and Use Committee of Columbia University, three (n=3) mongrel dogs of either sex, ranging from 23 to 32 kg in weight, were anesthetized with an intravenous injection of thiopental (10-17 mg/kg). They were mechanically ventilated with a rate- and volume-regulated ventilator on a mixture of oxygen

and titrated isoflurane (0.5-5.0%). Morphine (0.15mg/kg, epidural) was administered before surgery, and lidocaine (50 micrograms/kg/hr, intravenous) was used during the entire procedure. To maintain blood volume, 0.9% saline solution was administered intravenously at 5mL/kg/hr. The animal was positioned supine on a heating pad. Standard limb leads were placed for surface electrocardiogram (ECG) monitoring. A solid-state pressure transducer catheter (Millar Instruments, Houston, TX) was inserted into the left-ventricular cavity via the left carotid artery, the aortic root and across the aortic valve. Oxygen saturation of the blood, and peripheral blood pressure were monitored throughout the experiment. The chest was opened by lateral thoracotomy using electrocautery. After removal of the pericardium, a customized constrictor and a flow probe (Transonic Systems, Inc., USA) were positioned immediately distal to the first diagonal of the left anterior descending (LAD) coronary artery to induce graded LAD occlusion -and thus variable ischemic levels- at 20% increments of the initial coronary blood flow. A total of twelve piezoelectric crystals (Sonometrics Corp., Canada) were then implanted in the left ventricular wall. For endocardial and mid-wall crystals, an 18G needle was used for insertion. All crystals were maintained in position after placement using silk sutures.

EWI using ACT (Section 4.2) was performed at each LAD flow occlusion level. Forty-five minutes after complete LAD occlusion, the constrictor was released for complete reperfusion and the same scanning procedure was repeated. The heart was then excised and sectioned in 1-cm transverse slices to perform pathology. The sliced heart sections were immersed in a 1% Triphenyltetrazolium chloride (TTC) solution and incubated at 37°C for 1.5 hours. The sections

were finally fixed in a 10% formalin solution for 30 minutes. A pale region indicated the site of the ischemia/infarction, while the stark color represented the viable cardiac muscle.

6.2.2 Results

Figure 6-1 shows the evolution of the EW propagation at different levels of ischemia. The time, at which the images are displayed, corresponds to the time, at which the activated region covered the largest portion of the myocardium, i.e., immediately after electrical activation and preceding the closing of the mitral valve. When the LAD was occluded at 60% and beyond, the ischemic region was easily identified as the region, through which the EW cannot propagate. The ischemic region appears to grow with the LAD occlusion level until it reaches a maximum size at 100% LAD flow occlusion (**Figure 6-1**(f)). After reperfusion, the size of the ischemic region in the posterior wall decreases. The presence of acute ischemia was confirmed with pathology, after reperfusion (**Figure 6-1**(i)). TTC was used to stain non-viable tissue, which generally spans a smaller region than the ischemic one (Liu et al., 2002). Reperfusion accentuates the size of this non-viable region (Farb et al., 1993). The transverse slice shown in **Figure 6-1**(i) was obtained approximately at 3 cm from the apex.

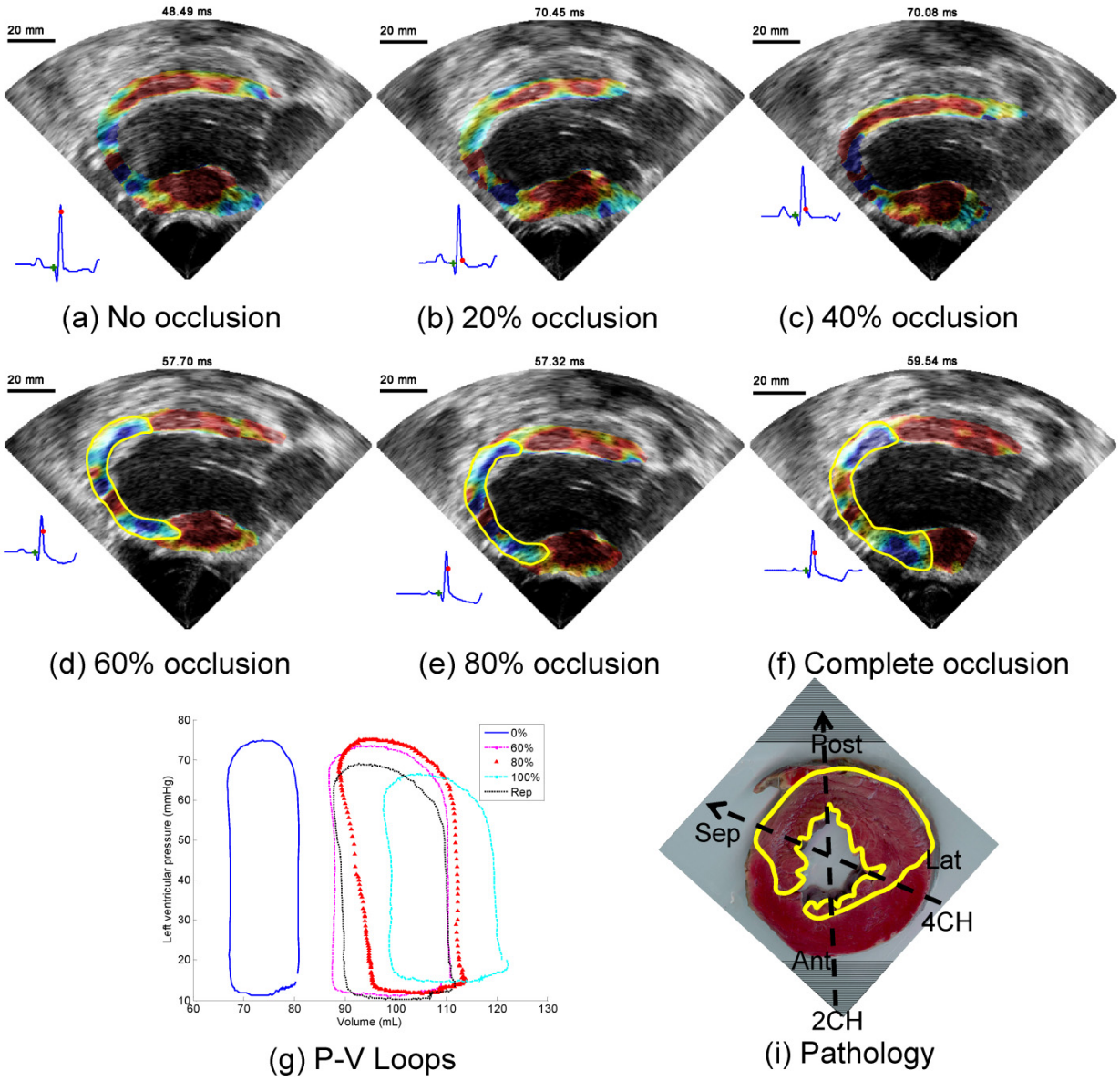

Figure 6-1 Evolution of the EW as the occlusion level of the LAD is increasing. The time point chosen to display the EW corresponds to the time at which the largest portion of the myocardium is activated. No significant differences were observed between (a) no occlusion and (b) 20% and (c) 40% flow occlusion. The ischemic region (delimited by the yellow line) becomes visible at (d) 60% flow occlusion and increases in size as the level of flow occlusion reaches (e) 80% and (f) 100%. g) After reperfusion, the ischemic region was smaller. h) Evolution of the PV loop with the occlusion level. (i) TTC staining after infarction (reperfusion). This mid-apical slice shows the extent of the infarcted region (white) over the viable tissue (red). The parasternal two- and four-chamber views are also depicted. (Provost et al., 2010)

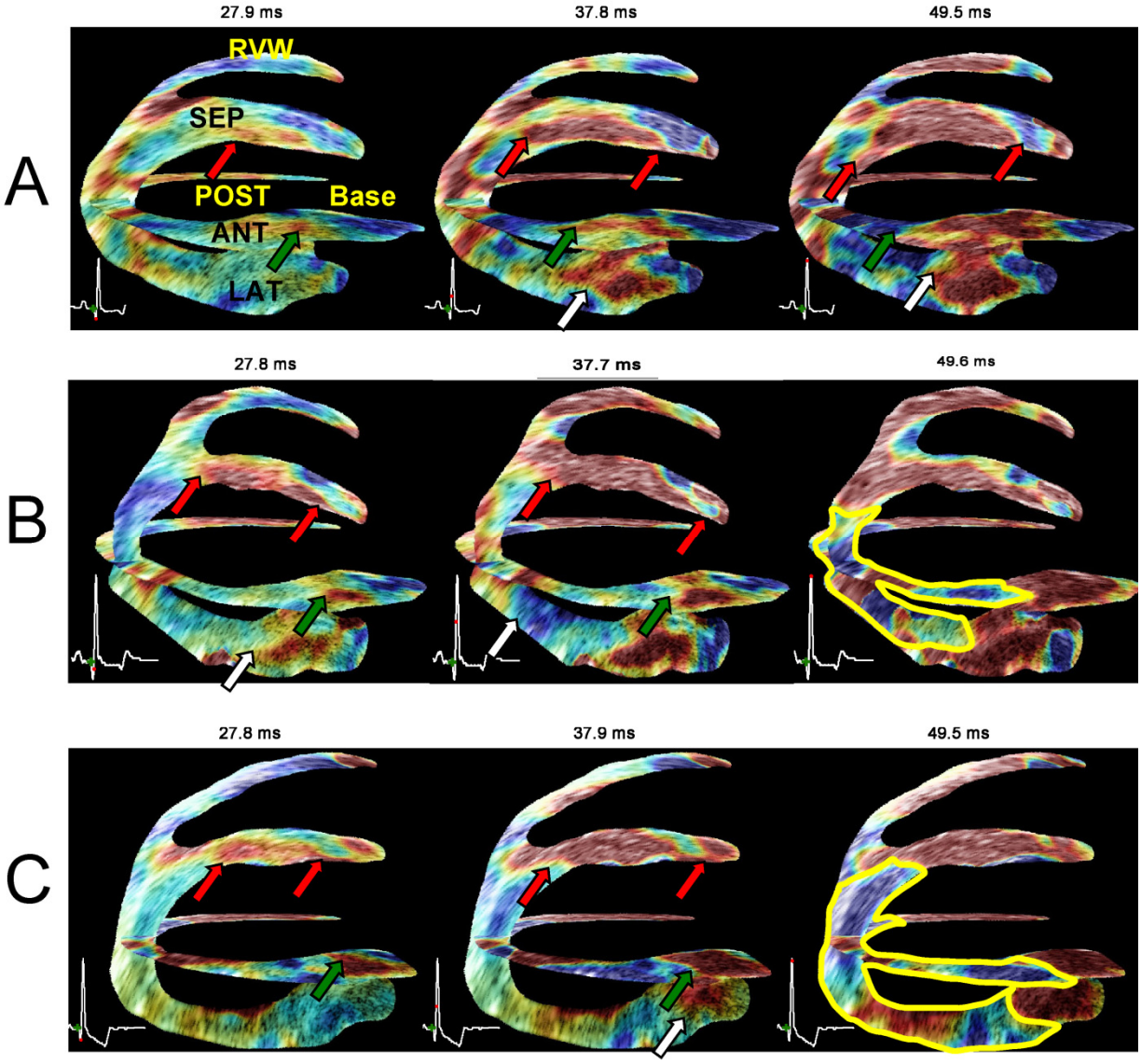

Figure 6-2 Bi-plane (two-chamber and four-chamber views) view of the same heart under different LAD coronary artery occlusion levels. Red, white and green arrows indicate the propagation of the EW in the septal, anterior, and lateral wall, respectively. (a) Without any occlusion, i.e. normal coronary flow, radial thinning is visible up to regions where the axial direction of the ultrasound beam coincides with the longitudinal direction of the cardiac geometry, where shortening is expected (in blue). (b) At 60% occlusion, this behavior is reversed in presence of ischemia: a region (delimited with a yellow line) containing radial thinning (blue) and longitudinal lengthening (red) is observed. (c) At complete occlusion this region increases in size. The ischemia is visible in the anterior, posterior and lateral wall near the apex at 60% occlusion and in the anterior, posterior, lateral, and septal wall at 100% occlusion. (Provost et al., 2010)

Figure 6-2 shows the comparison between the normal, 60% LAD occlusion and 100% LAD occlusion in a bi-plane view. In the ischemic cases, the wave was initiated as in the normal case, but its propagation was impeded at the apical region, where the ischemic region is expected to form. After EW propagation, a region that did not undergo thickening could be identified, which indicated an inability of the tissue to contract. The location of the ischemic region (yellow contour in **Figure 6-2**) is consistent with the pathology findings as shown in **Figure 6-1**(i).

6.2.3 Discussion

The presence of ischemia impeded the EW from propagating. This is expected, since during the first few minutes of ischemia, the myocardium gradually loses its ability to generate systolic force (Holmes et al., 2005). In other words, even if the electrical activation did occur, the ischemic region would not contract in response to it. Previous studies (Villarreal et al., 1991) confirmed that five minutes of experimental ischemia in dogs converted the normal pattern of systolic circumferential and longitudinal shortening and radial thickening to circumferential and longitudinal thickening and radial shortening. Earlier studies (Vatner, 1980) found the relationship between regional myocardial shortening and the level of blood flow irrigating that region to be exponential, i.e., that the decrease in regional thickening becomes more important as the coronary flow is diminished, and that a 20% LAD flow occlusion level was sufficient to significantly impair cardiac function. In the present study, an ischemic region could be clearly identified when the LAD was occluded at 60% and beyond and was increasing in size as the

level of LAD occlusion increased. The biplane view shown in **Figure 6-2**B indicates the presence of ischemia in the apical region even when the LAD is not completely occluded.

By comparing **Figure 6-2** B and C, it is possible to observe the ischemic region growing towards the lateral, posterior, and septal walls with increasing levels of LAD flow occlusion. Currently, the echocardiographic stress test may allow detection of early ischemia. However, such tests are limited by low image quality caused by fast heart rates, potential contrast administration requirements, and the limited time available to acquire an image. Moreover, for patients who cannot perform the stress test, drugs such as dobutamine may need to be systemically administered. Therefore, EWI at rest could become a valuable complementary or alternative method to the echocardiographic stress test for early ischemic onset detection. However, these results also suggest that EWI might be limited in assessing the electrical activation sequence occurring in regions undergoing acute ischemia and, therefore, negligible strains.

6.3 Left Bundle Branch Block

6.3.1 Methods

In this study approved by the Institutional Animal Care and Use Committee of Columbia University, one (n=1) male mongrel of 25 kg in weight, was anesthetized with an intravenous injection of thiopental (10-17 mg/kg). The animal was mechanically ventilated with a rate- and volume-regulated ventilator on a mixture of oxygen and titrated isoflurane (0.5-5.0%). Morphine (0.15mg/kg, epidural) was administered before surgery, and heparin was administered throughout the procedure. To maintain blood volume, 0.9% saline solution was

administered intravenously at 5mL/kg/hr. Oxygen saturation of the blood, and peripheral blood pressure were monitored throughout the experiment. The animal was positioned supine on a heating pad. Standard limb leads were placed for surface electrocardiogram (ECG) monitoring. An RF ablation catheter was first inserted into the left-ventricular cavity with fluoroscopy guidance via the left carotid artery, the aortic root and across the aortic valve. The left bundle branch was localized near the ventricular septal base by identifying its signature (i.e., two activation spikes) on the bipolar electrogram measured with the ablation catheter. RF ablation was then performed, and successful ablation concluded upon by the observation of a marked widening of the QRS complex on the surface ECG. The RF ablation catheter was then removed and a basket catheter was inserted in the left-ventricular cavity. The positions of the splines were obtained by identifying spline markers on fluoroscopy images and later confirmed post-mortem after dissection the heart at the end of the experiment. The chest was opened by lateral thoracotomy using electrocautery and the pericardium was removed. EWI was performed in 2- and 4-chamber views using ACT.

6.3.2 Results

Figure 6-3 shows the EWI isochrones (**Figure 6-3**A), the electrical isochrones (**Figure 6-3**B), and their correlation (**Figure 6-3**C). The EW first propagated in the RV wall, followed by the septum, before reaching the LV posterior wall approximately 50 ms later. The entire LV was activated more than 125 ms after the Q-wave on the ECG. The electrical activation sequence of the LV shows a similar propagation pattern: the septal region is activated first, followed by the posterior wall, with the lateral wall region being activated last. This may seem in contradiction with the EW which propagated in the anterior wall last; however the basket catheter used

spanned only 31 mm in diameter, and therefore recorded the electrical activation of the bottom half of the LV. Following proper registration, a strong correlation (R^2=0.69) between the electrical and electromechanical activation (**Figure 6-3**C) is obtained, with a slope of 2.11.

6.3.3 Discussion

The results of this study demonstrate that the correlation between the electrical and electromechanical activations is maintained during LBBB. Remarkably, the slope obtained was significantly higher (2.11) than during pacing (1-1.31). Slopes larger than 1 already indicate an increasing electromechanical delay with time, most likely caused by the tethering of inactivated regions. More specifically, when the positive strains in an activated region are high, they generate negative strains in the neighboring regions. Therefore, strains in an inactivated region are negative and become larger as the rest of the heart undergoes activation. In other words, the correlation slope is expected to increase with the dyssynchrony of the electrical activation of the heart.

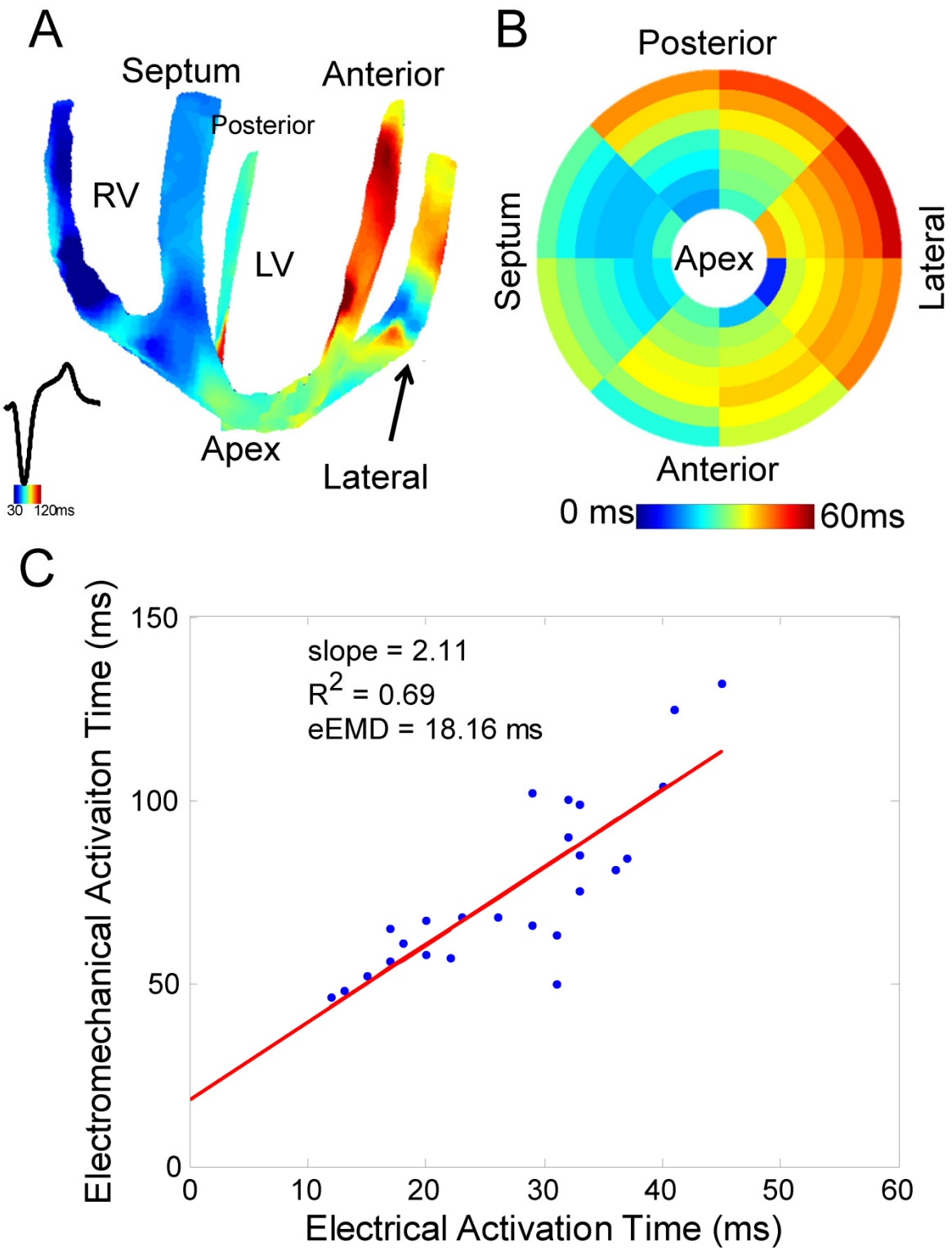

Figure 6-3 EWI during LBBB. (A) Bi-plane isochrones of the electromechanical activation. (B) Endocardial electrical activation map. (C) Correlation between the electrical and electromechanical activations.

6.4 Fibrillation

6.4.1 Methods

In this study, approved by the Institutional Animal Care and Use Committee of Columbia University, two male mongrel dogs, 18-25 kg in weight, were anesthetized with an intravenous injection of Diazepam 0.5-1.0mg/kg as premedication, and Methohexital 4-11mg/kg as induction anesthetic or with an intravenous injection of thiopental (10-17 mg/kg). The animals were mechanically ventilated with a rate- and volume-regulated ventilator on a mixture of oxygen and titrated isoflurane (0.5%–5.0%). Morphine (0.15 mg/kg, epidural) was administered before surgery, and lidocaine (50 micrograms/kg/h, intravenous) was used during the entire procedure.

To maintain blood volume, 0.9% saline solution was administered intravenously at 5 mL/kg/h. Standard limb leads were placed for surface electrocardiogram (ECG) monitoring. Oxygen saturation of the blood and peripheral blood pressure were monitored throughout the experiment. The chest was opened by lateral thoracotomy using electrocautery. In one case, three pacing electrodes were sutured at the basal region of the lateral wall, at the left ventricular apex and at the right ventricular apex. RF ablation of the left bundle branch was performed under fluoroscopy and a basket catheter (Boston Scientific, Natick, MA) was introduced in the left ventricle via the carotid artery. EWI was performed with TUAS using a conventional scanner.

In the second animal, the basket catheter was inserted in the left ventricle via an apical puncture. EWI with a virtual-source sequence at 2000 fps was performed during 1 second simultaneously with mapping using a basket catheter during ventricular fibrillation. The dominant frequencies (Sanders et al., 2005) of both the strain and electrical potential were also computed by identifying the frequency with the largest amplitude below 15 Hz after performing a fast Fourier transform. Dominant frequencies can be used to identify potential ablation sites in patients with atrial fibrillation (Sanders et al., 2005). EWI was performed using the virtual-source sequence. In both animals, ventricular fibrillation occurred spontaneously.

6.4.2 Results

The EW was first imaged during pacing using TUAS (Section 4.3) in a full four-chamber view of a heart in an open-chest canine *in vivo*. **Figure 6-4** shows the axial incremental strains during the EW imaged with an 1100-Hz motion-estimation rate and a 137-Hz motion-sampling rate. These images show features of the EW that are expected during pacing from the basal region of the lateral wall. The EW first appears in the basal region of the lateral wall (**Figure 6-4**(a),(b)), approximately 30 ms after pacing. The EW was initiated at the epicardium and traveled toward the endocardium of the lateral wall. The EW then propagated to the septum (**Figure 6-4**(b)-(f)) and then to the right ventricle (**Figure 6-4**(f)).

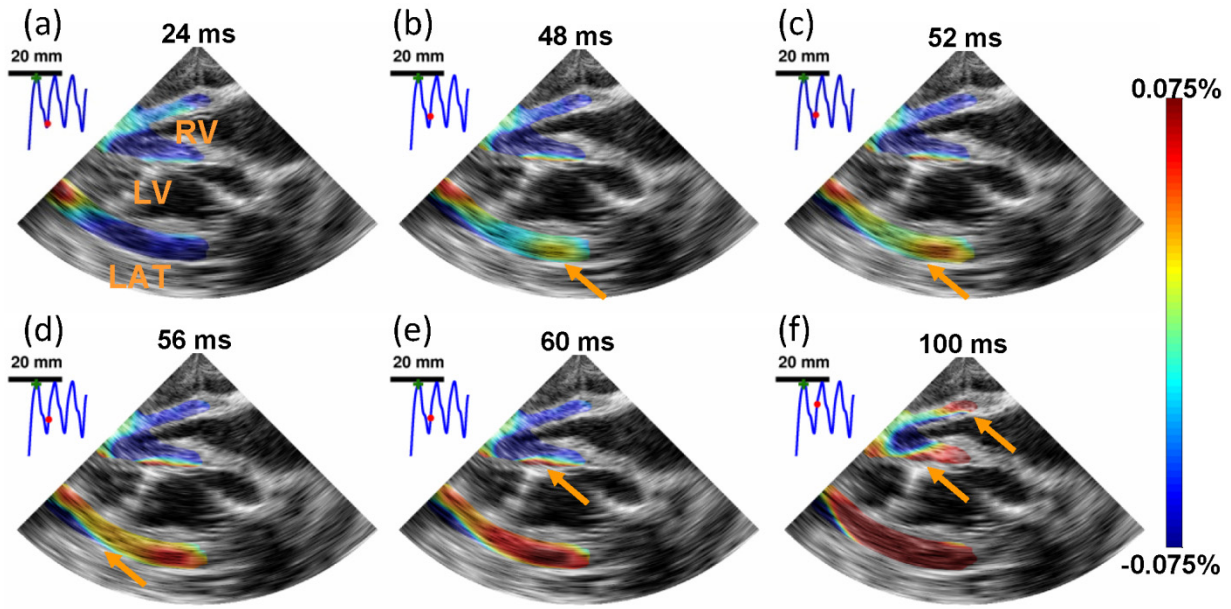

Figure 6-4 EWI during pacing in the four chamber parasternal view. RV, LV, and LAT, respectively, denote right ventricle, left ventricle and lateral wall. Arrows depict the propagation of the EW. The EW was initiated in the right part of the lateral wall (b) and propagated toward the apex, followed by the septum (b-e) and right-ventricular wall (f). 0 ms corresponds to the pacing time. Motion-estimation rate : 1100 fps. Motion-sampling rate : 128 fps.

Previously, the EW had been observed at high resolution in a full view of the heart only during periodic, repeatable heartbeats. Using TUAS, it was possible to image cardiac abnormalities that are non-periodic, such as fibrillation. **Figure 6-5** shows such an example. After prolonged pacing, the heart underwent ventricular fibrillation. EWI was performed with a motion-estimation rate of 2000 Hz. The acquisition was performed during 8 seconds. No or limited wall motion could be observed on the B-mode. However, the incremental strains mapped depicted small, local and oscillating deformations. While pacing from the basal region of the lateral wall was maintained during fibrillation, no clear propagation was observed from the pacing origin.

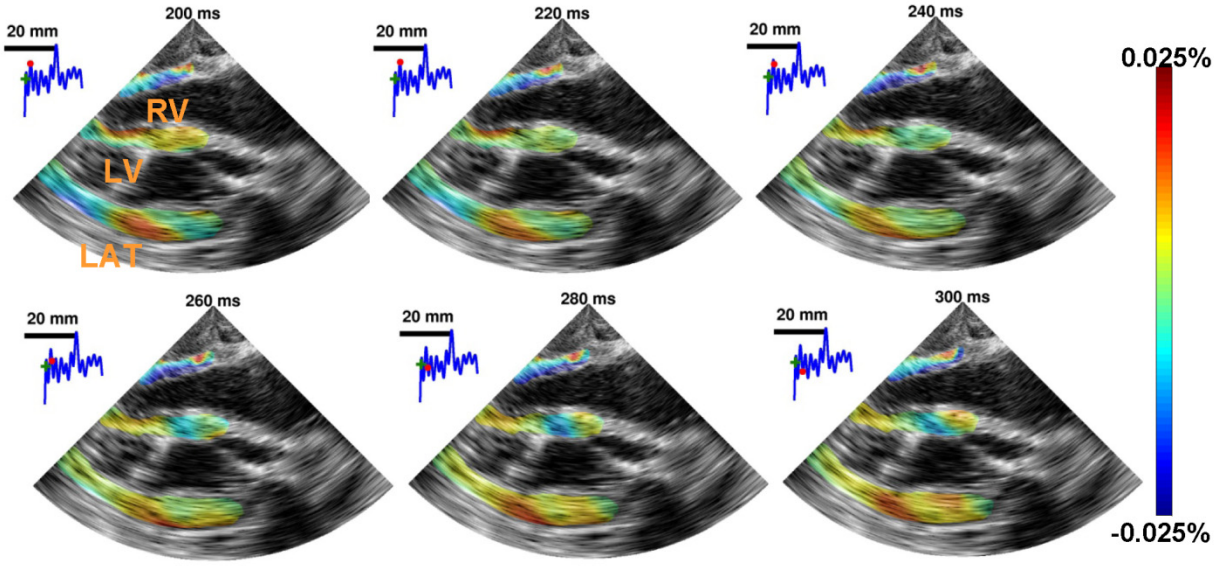

Figure 6-5 EWI during fibrillation in the four chamber apical view over 100 ms. RV, LV, and LAT, respectively, denote right ventricle, left ventricle and lateral wall. No organized contraction can be observed. EWI was performed with a 2000 Hz motion-estimation rate and a 120 Hz motion-sampling rate.

Ventricular fibrillation was further characterized in the second canine. **Figure 6-6** shows the strain and electrical potentials over time (**Figure 6-6**A), along with their respective Fourier transform (**Figure 6-6**B). Additionally, EWI dominant frequencies were mapped (**Figure 6-6**C). The dominant frequencies electrical potentials were obtained with a resolution of 0.24 Hz and were comprised between 5.12 and 8.9 Hz, with an average value of 6.14±0.24 Hz. EWI dominant frequencies at the locations of the basket catheter electrodes were obtained with a resolution of 1 Hz and were comprised between 4.1 and 7.1 Hz with an average of 4.9±1 Hz.

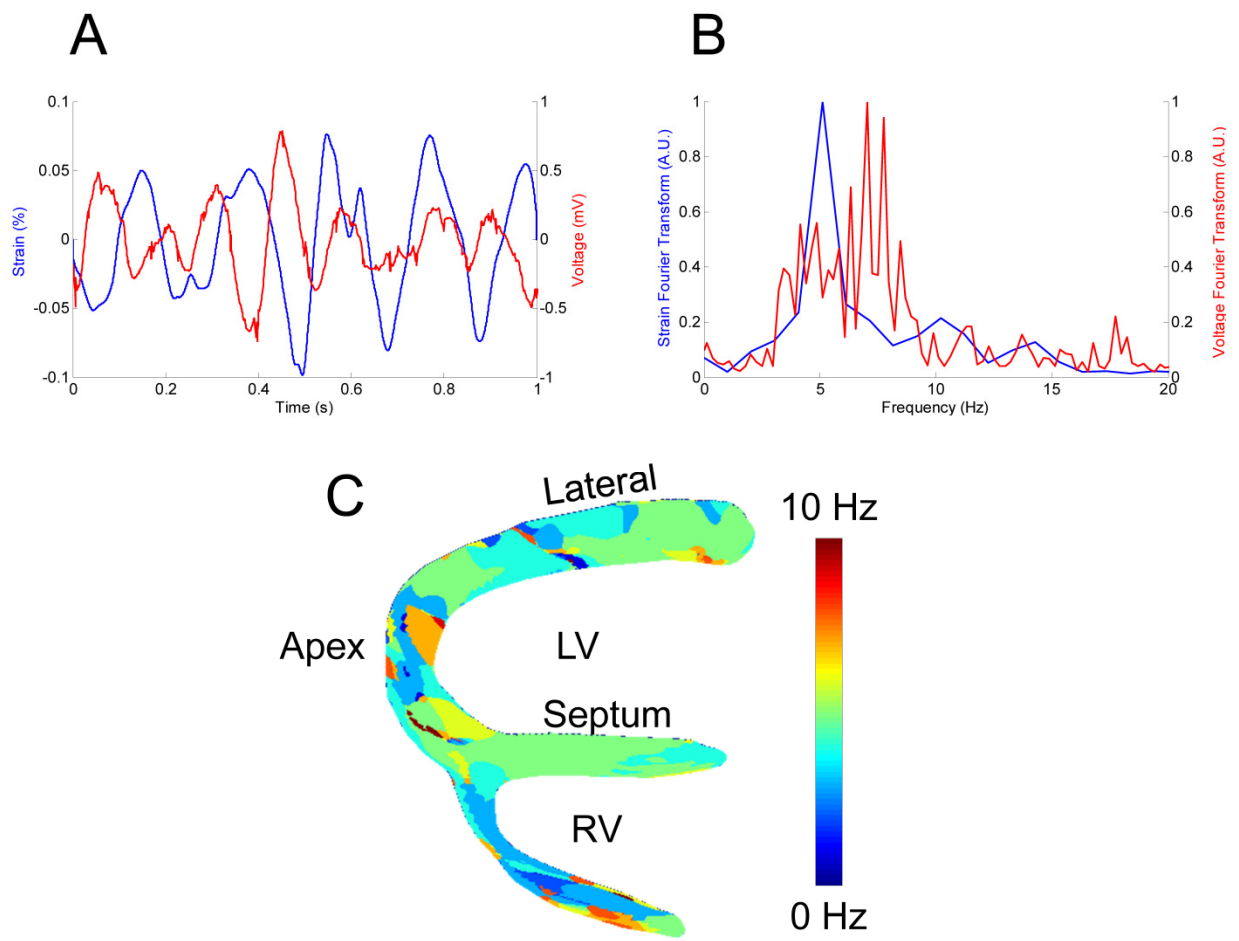

Figure 6-6 EWI during fibrillation. (A) Comparison between the electrical potential and the strain at the same location in the heart. (B) Fast Fourier transform of the signals obtained in A. (C) Map of the dominant frequencies obtained with EWI.

6.4.3 Discussion

The EW propagation pattern obtained during ventricular pacing could easily be distinguished from fibrillation. EWI was shown capable of mapping dominant frequencies occurring during fibrillation and was in agreement with electrical mapping. It is important to note that there is no technology existing today that can provide maps of dominant frequency transmurally in a full field of view. Indeed, while the dominant frequencies obtained with EWI were not identical

to the ones measured with electrical mapping, they were within the uncertainty range of this study. These results show that EWI can map non-periodic arrhythmias *in vivo* and can be used to characterize fibrillation.

6.5 Atrio-Ventricular Dissociation

6.5.1 Methods

Four normal, conscious, shaved, mongrel canines of 20-25 kg in weight were imaged before and after the implantation of a pacemaker in the right ventricle and ablation of the atrio-ventricular node in a closed-chest setting. These canines were conscious and drug-free and were gently held on a table by two people during the ultrasound scan. EWI was performed using the virtual-source sequence, in the apical 4-chamber view.

6.5.2 Results

EWI was performed in a standard apical four-chamber view in a normal, conscious canine during sinus rhythm using the virtual-source sequence. In that view, the EW is expected to mostly result in shortening (negative strains) of the tissue, since the ultrasound beam is aligned with the longitudinal direction of the heart. During sinus rhythm, the natural pacemaker is the sinus node, located in the right atrium. Signals are generated spontaneously at the node, travel through the atrium (during the P-wave), to the atrio-ventricular node, the bundle of His and finally the Purkinje fiber network and the ventricular myocardium (during the QRS complex). Complex activation patterns are expected when imaging the ventricles, since activation will originate from multiple locations following the Purkinje fiber network. **Figure 6-7** shows that the EW follows such a pattern. The EW (shortening, blue) originated from the right atrium and

propagated towards the left atrium. Between the P- and the Q-wave on the ECG, little or no propagation is observed. During the QRS complex, activation originating from multiple sources, located for example at the mid-level of the septum, high on the lateral wall and near the right apex are observed. These results are in accordance with previous studies of the normal electrical activation of the heart (Scher and Young, 1956; Durrer et al., 1970).

The same animal was then imaged during pacing from the right ventricle after ablation of the atrio-ventricular node. In that case, the electrical activation of the atria and the ventricles are dissociated, i.e., the activation of the sinus node do not necessarily results in the activation of the ventricles. This phenomenon can be observed on the ECG trace, where multiple P-waves without a following QRS complex can be observed (**Figure 6-8** A). During the P-wave, the EW (shortening, blue) is initiated from the right atrium and propagates in the left atrium (**Figure 6-8**B). This is expected, since the atria are still driven by the sino-atrial node as during sinus rhythm (**Figure 6-7**). During the QRS complex however, activation was triggered by the pacemaker located near the apex of the right ventricle. Therefore, the EW was expected to propagate from the right ventricle near the apex towards the other regions of the heart. EWI displays such a pattern (**Figure 6-8** C): the EW (shortening, blue) originated near the right ventricular apex and propagated towards the septum and the lateral wall.

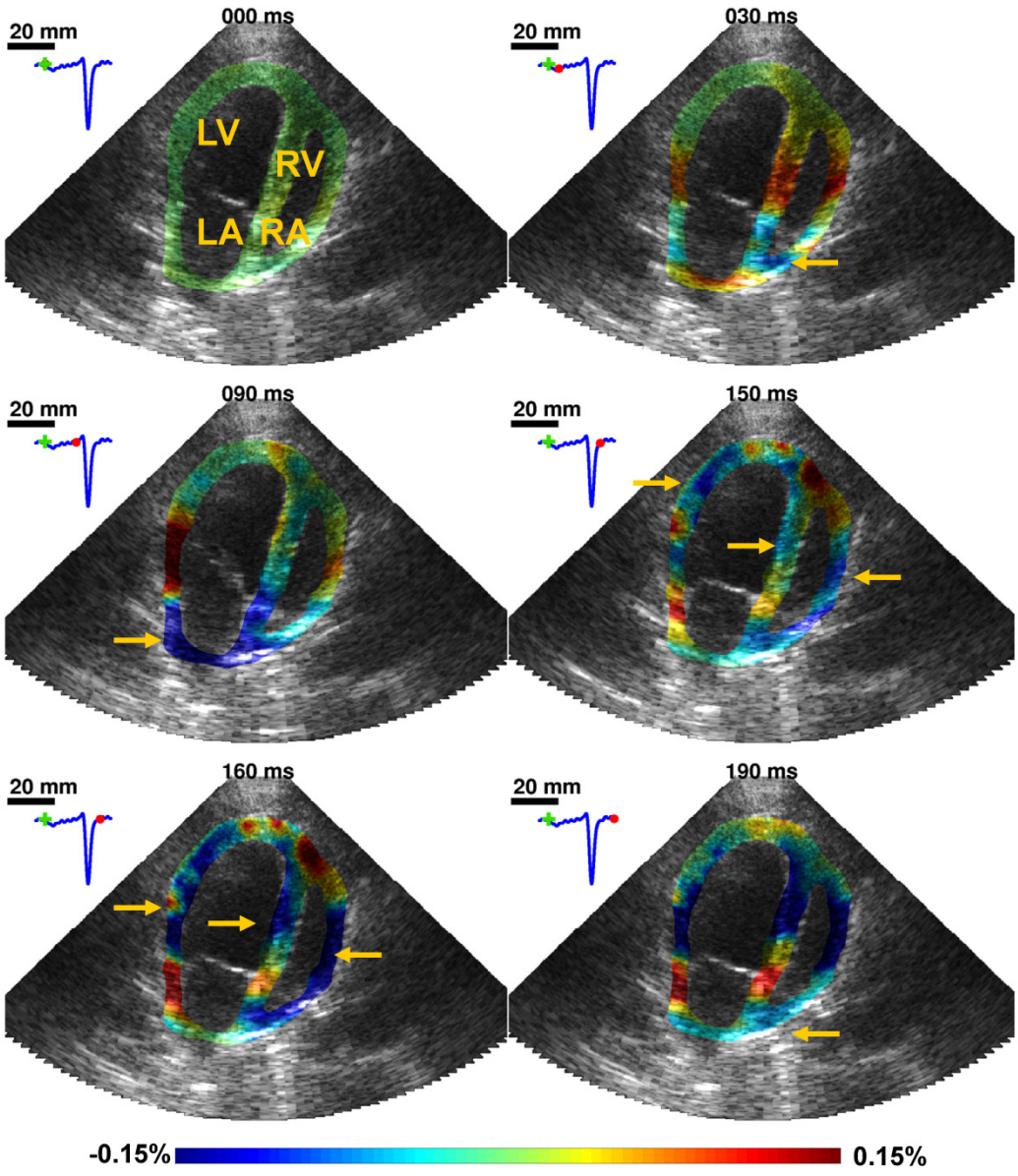

Figure 6-7 EWI during sinus rhythm in a closed-chest canine. Activation is first observed in the right atrium (30 ms) followed by the left atrium (90 ms). Activation is then mapped in the ventricles, from multiple origins located on the endocardium of the septum, in the right ventricular wall and near the apex in the lateral wall (150-160 ms) until complete activation (190 ms). (Provost, Nguyen, et al., 2011)

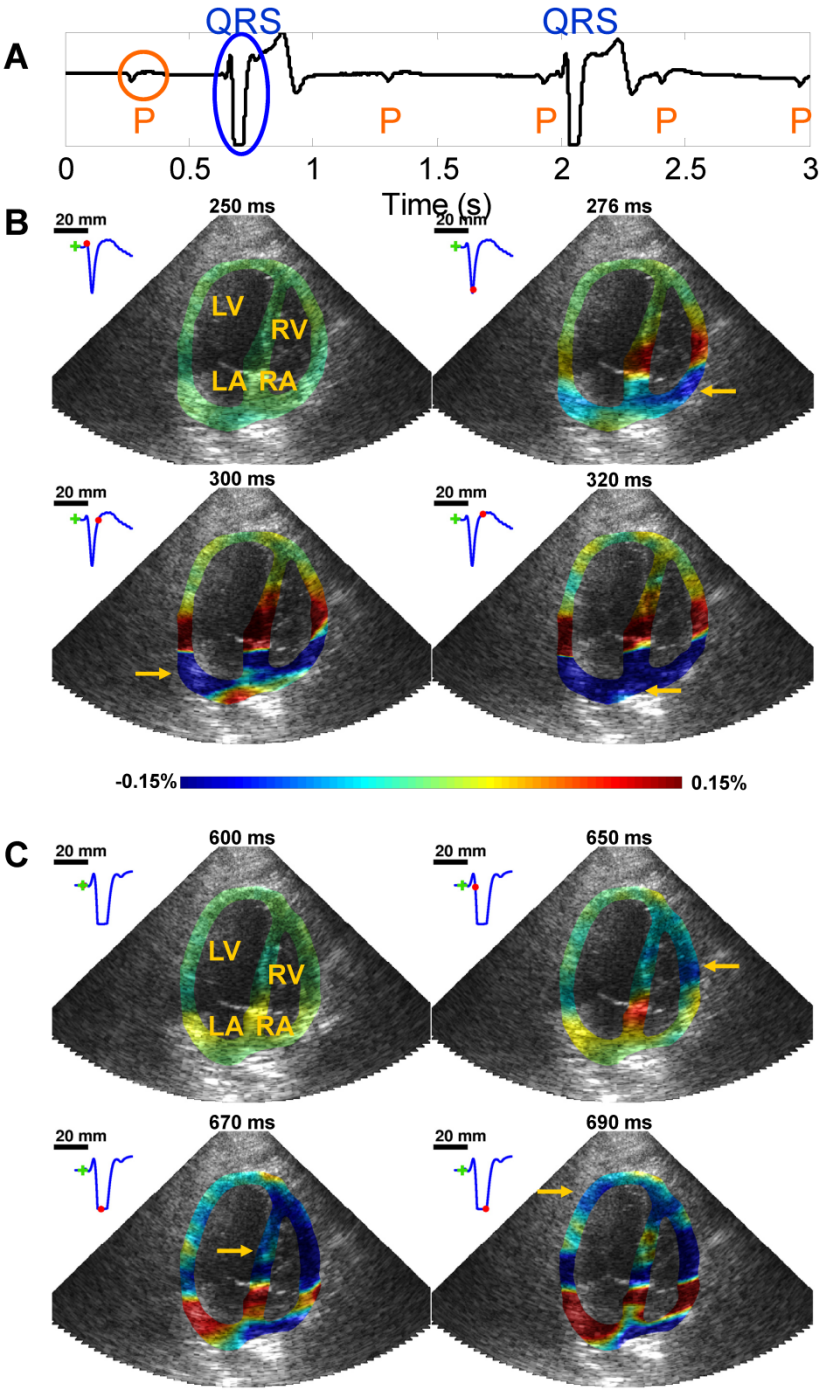

Figure 6-8 EWI during pacing from the right ventricle in a closed-chest canine. (A) ECG during atrioventricular dissociation. P-waves do not result to QRS complexes, since the atria and ventricles are electrically isolated. A total of five P-waves can be observed, while only 2 QRS complex are present. (B) EWI during the first P-wave (circled). Activation (blue) is initiated in the right atrium (276 ms) and propagates towards the left atrium (300, 320 ms). (C) EWI during the first QRS complex (circled). Activation (blue) is first observed in the right-ventricular wall (650 ms). The septum is then activated (670 ms), followed by the lateral wall (690 ms). Activation does not propagate to the atria, since the atrio-ventricular node was ablated.(Provost, Gurev, et al., 2011)

6.5.3 Discussion

The results of this study demonstrate that EWI can characterize different rhythms, including non-sustained ones. Additionally, the rhythms mapped were in accordance with the expected electrical activation sequence. Indeed, the atrial electromechanical activation remained similar before and after the ablation of the atrio-ventricular node. These results also indicate the EWI capability of mapping the electromechanical activation in the atria, in a closed-chest setting, and open the door to its application to humans (Chapter 7).

6.6 Conclusion

In this chapter, we investigated the capability of EWI to map the electrical activation of the diseased heart, i.e., during ischemia, LBBB, fibrillation, and atrio-ventricular dissociation. Both ischemia and LBBB are often linked to heart failure and to the clinical decision-making of implanting a cardiac resynchronization therapy device. Assisting in the decision around implanting such a device and CRT treatment monitoring are target applications of EWI. Understanding the effect of such conditions on the EW constitutes an important milestone in the development of EWI. The detection of LBBB in a patient with heart failure is, on the other hand, behind the rationale for the implantation of a CRT device: because the left ventricle undergoes a delayed activation, adding a pacing electrode on the epicardium of the LV can help to reduce the dyssynchrony of the heart. More specifically, the results obtained in this chapter indicate that during sinus rhythm, ischemia results in the absence of propagation of the EW in the ischemic region, while the electrical activation sequence could be obtained with high accuracy during LBBB. The study of fibrillation demonstrated that EWI can characterize uncoordinated activation sequences in the ventricles. This is an important result to consider for

the application of EWI to atrial arrhythmias, of which atrial fibrillation is the most common. Finally, we demonstrated that EWI could be applied in conditions similar to a clinical setting and using apical views, which are typically easier to obtain in patients. Indeed, mapping the EW during atrio-ventricular dissociation was performed and demonstrated that EWI is reliable even in complex, non-sustained rhythm. We have shown for the first time that EWI can map the activation of the atria *in vivo* and in a closed-chest setting during sinus rhythm. The fact that the activation originated from the right atrium and propagated towards the left atrium suggests a correlation with the electrical activation, as the main pacemaker of the heart, i.e. the sino-atrial node, is located in the right atrium. Finally, the atrial activation remained the same after ablation of the atrio-ventricular node, as expected, and the EW accurately depicted pacing from the right-ventricle. In the following chapter, EWI is applied in normal human subjects and in patients in apical views.

Chapter 7 Clinical Applications

7.1 Introduction

In Chapters 5, and 6, we demonstrated that Electromechanical Wave Imaging (EWI) can be used to characterize rhythms in normal hearts both during sinus rhythm and pacing, and in the presence of conditions such as ischemia, left bundle branch block (LBBB), fibrillation and atrio-ventricular dissociation, in all four chambers of the heart. This demonstrates that EWI has the potential to characterize heart failure and atrial arrhythmia, both of which are major healthcare challenges today. In this chapter, we perform a feasibility study of EWI in normal patients, in patients with heart failure and cardiac resynchronization therapy (CRT), and in patients with atrial tachyarrhythmia.

Cardiac arrhythmias and conduction abnormalities have been linked to stroke (Wolf et al., 1991), heart failure (Carson et al., 2005) and sudden cardiac death (Zheng et al., 2001), but currently physicians do not have access to a noninvasive imaging modality to map the site of arrhythmogenesis for diagnosis, treatment planning and follow-up. LBBB and tachyarrhythmias are associated with heart failure, morbidity, and mortality and can be treated with biventricular pacing therapy and radiofrequency ablation, respectively. One of the major limitations in the utility of these treatment strategies is the current lack of access to a noninvasive imaging modality capable of accurate mapping of electrical activation in the heart. The only noninvasive tool currently available to the physician is the 12-lead electrocardiogram (ECG), which provides information on the conduction and global activation properties of the heart. The 12-lead ECG does, however, have limitations in reliably determining the site of origin or specific underlying mechanism of atrial tachyarrhythmias, such as macro-reentrant atrial flutter (AFL) vs. focal

atrial tachycardia. Detailed mapping of cardiac electrical activity during arrhythmias can be achieved with intracardiac electroanatomical mapping, a procedure that consists of introducing electrode-catheters into the heart chambers to obtain a series of local intracardiac electrograms. This approach is, however, costly and time consuming, and, as with any invasive procedure, carries some degree of risk. Both 12-lead ECG and invasive methods are also limited in their utility for monitoring response to CRT therapy over an extended period of time. The mechanisms by which CRT can reverse heart failure are not fully understood and the lack of tools to longitudinally study the electromechanical effects of CRT has limited the development of effective techniques for optimization of pacing parameters (Chung et al., 2008; Hsing et al., 2011). Finally, our understanding of the normal human transmural cardiac activation is limited, as it is extrapolated from data derived from animal studies, *ex vivo* human hearts (Durrer et al., 1970), and endocardial or epicardial mapping studies of arrhythmia patients (Cassidy et al., 1984; Ponti et al., 2002; Kojodjojo et al., 2006). New imaging modalities (Rudy and Burnes, 1999), based on body surface potential measurements, have also been developed to noninvasively map the electrical activation of the epicardium in normal (Ramanathan et al., 2006) and arrhythmic (Ramanathan et al., 2004; Wang et al., 2007; Ghosh et al., 2008) human subjects. However, these methods required patient-specific modeling and were limited to depicting the epicardial electrical activation, although new approaches are being developed to map the endocardial (Modre et al., 2003) and transmural (Zhang et al., 2005) activations. More importantly, these methods rely on either ionizing three-dimensional computerized tomography or magnetic resonance imaging, which is contraindicated in patients with pacemakers, defibrillators, or other metallic hardware.

In this feasibility study, we demonstrate for the first time that noninvasive transthoracic EWI acquisitions can be used to map the electrical activation sequence during different cardiac rhythms in humans. The normal transmural electromechanical activation sequence maps detected the region of early activation with the expected location of the sino-atrial node in the right atrium; further activation sequence of the normal sinus rhythm into the ventricles also correlated with the expected endocardial sites of early activation in the ventricles. EWI was performed in CRT patients with LBBB, during sinus rhythm, left-ventricular (LV) pacing, and right-ventricular (RV) pacing. The electromechanical activation maps demonstrated the capability of EWI to locate the pacing sites and characterize the LBBB activation sequence transmurally. EWI was also performed in atrial flutter patients and correlated with results from invasive intracardiac electrical mapping studies. Finally, the feasibility of single-heartbeat EWI using parallel beamforming with a virtual-source sequence is demonstrated for the first time in humans in a subject with both AFL and right bundle branch block (RBBB).

Our findings show the potential for EWI to provide information on the normal cardiac activation, to assist in the diagnosis and treatment planning of patients with cardiac arrhythmias (even in patients with non-sustained arrhythmias since EWI can be performed in a single heartbeat), and to aid in monitoring and follow-up of patients undergoing CRT pacing therapy in a noninvasive, low-cost, and potentially real-time fashion.

7.2 Methods

The study protocol was approved by the Institutional Review Board (IRB) of Columbia University, and informed consent was obtained from all human subjects prior to scanning. Five normal subjects (21-23 years old) were imaged by a trained cardiologist. Three subjects with CRT were scanned during scheduled routine device checks. The device was first configured to pace only from the LV, after which EWI was performed in the four-chamber view. EWI was then performed when the device was set to pace only from the RV and when the device was not pacing. The pacing rate was adjusted to sufficiently high values to minimize beats triggered by sinus rhythm. Finally, EWI with ACT (Section 4.2) and parallel beamforming with 2-D virtual point-source transmit beam (Section 4.4) was performed on two and one patients with AFL, respectively, a few minutes to a few hours prior to a scheduled mapping and ablation procedure.

7.3 Normal Subjects

7.3.1 Results

EWI with ACT (Section 4.2) was performed on normal subjects for this study (**Figure 7-1**, **Figure 7-2**). The EW was found to originate in the RA, propagating towards the LA. During the QRS complex, the EW propagated in the ventricles from multiple origins and propagated transmurally from the endocardium to the epicardium. **Figure 7-2**D-E depicts the atrial (**Figure 7-2**D) and ventricular (**Figure 7-2**E) activation of the first normal subject (**Figure 7-2**A) in greater detail. The EW originated in the superior wall of the RA, near the lateral wall, and propagated towards the LA (**Figure 7-2**D). The site of earliest activation is compatible with the expected

location of the sinus node. In the two-chamber view (**Figure 7-2**D), which depicts the LA and the LV, the EW originated in the superior wall of the LA and propagated toward the posterior and anterior walls. The last region to undergo electromechanical activation was located in the LA anterior wall, near the mitral valve (**Figure 7-2**D). Following a delay similar to the PR segment, the ventricles were activated from three main origins, i.e., near the apex in the posterior wall, at the mid-level of the septum, and near the base in the anterior wall, as depicted in the electromechanical activation isochrones (**Figure 7-2**E). From these three origins, the EW propagation occurred transmurally from the endocardium towards the epicardium (**Figure 7-2**E).

7.3.2 Discussion

The activation sequence found in normal subjects with EWI is in accordance with the literature regarding sinus rhythm (Section 2.3.1): as in the normal electrical activation sequence, the EW first appeared at the sinus node location in the RA and propagated within the RA and into the superior wall of the LA as expected due to the conduction through the Bachmann's bundle. Activation further propagated toward the inferior region of the RA and the anterolateral and posterior wall of the LA. The EW then propagated in the ventricle from three sites corresponding to the sites of early electrical activation, i.e. an area high on the anterior paraseptal wall immediately below the mitral valve, and area at half the distance from apex to base in the left side of the interventricular septum, and the posterior paraseptal area at approximately one third of the distance from apex to base (onset of the QRS complex).

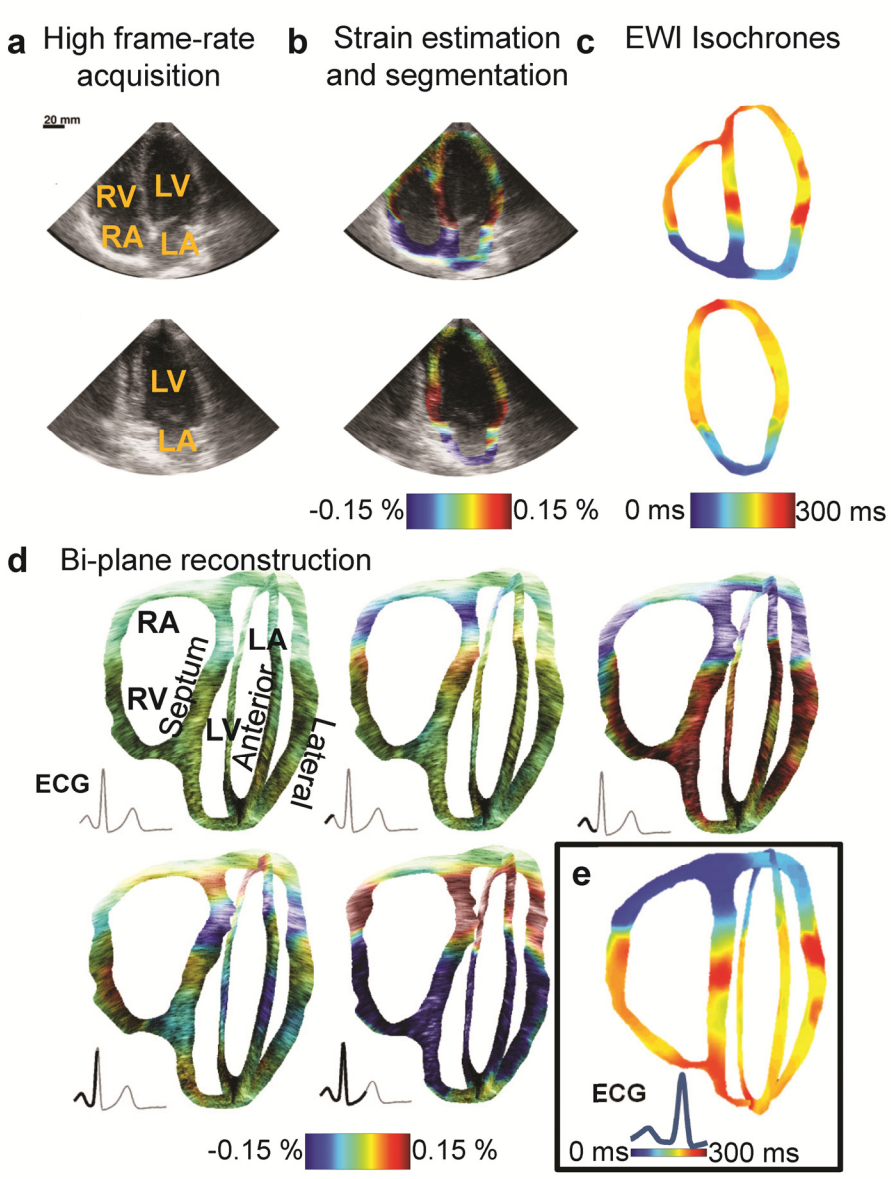

Figure 7-1 (a) High frame-rate acquisition of standard four and two-chamber RF images is performed using ACT or parallel beamforming with a virtual source sequence. (b) Motion maps are generated with RF cross-correlation and used to track the segmented heart throughout the cardiac cycle in both views (the first frame of each view is segmented manually). Axial incremental strains are then estimated and overlaid onto the B-mode images to produce the EWI ciné-loop. (c) EWI isochrones are obtained by mapping the local zero-crossing time of the strains. (d) Bi-plane representations of the EWI ciné-loop can then be generated by synchronizing (using the ECG) and combining both views. The example shown here is from a 23-year old male healthy volunteer. (e) EWI isochrones are finally obtained by mapping the first zero-crossing time of incremental strains following the onset of the P-wave (in the atria) or the onset of the QRS (ventricles). The EW originates in the right atrium and propagates towards the left atrium during the P-wave of the ECG. In the ventricles, activation originates from multiple endocardial breaking points located, for instance, at the mid-septum and mid-anterior-wall, near the right-ventricular apex and near the base on the lateral wall.

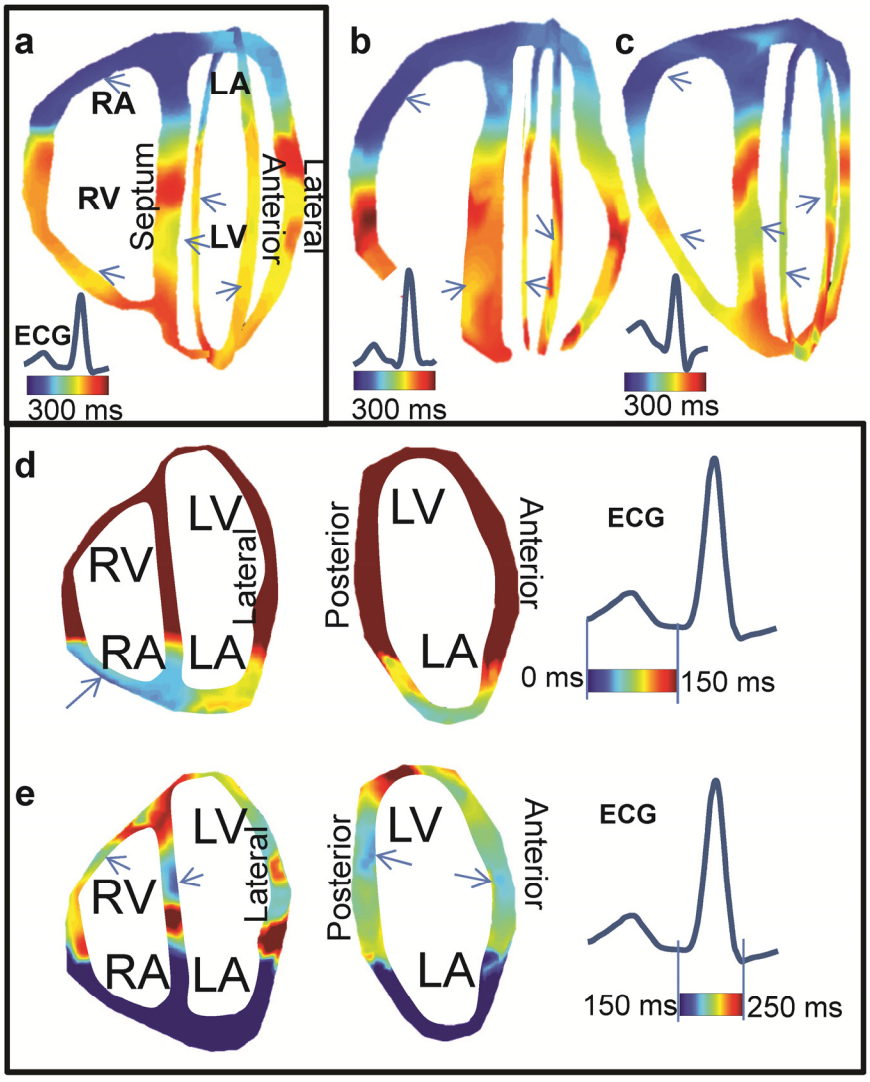

Figure 7-2 EWI isochrones of three normal subjects (a-c) The atrial activation sequence originates from the RA and propagates in the LA. In the two chamber view, propagation from the top of the LA is observed. In the ventricles, arrows indicate the sites of early activation, located in the septum at the mid-level, in the anterior wall near the base and in the posterior wall near the apex. (d-e) EWI isochrones of the normal subject (a) in the two and four-chamber views with different colorbars to highlight the atrial and ventricular activation sequences. The atrial activation sequence originates from the RA and propagates in the LA. In the two chamber view, propagation from the superior wall of the LA is observed. In the ventricles, arrows indicate the sites of early activation, located in the septum at the mid-level, in the anterior wall near the base and in the posterior wall near the apex, in the left ventricle, and near the apex of the right ventricle, in accordance with existing literature.

7.4 Cardiac Resynchronization Therapy

7.4.1 Results

Subjects with CRT devices have a pacemaker with three leads, typically one positioned in the RA appendage, a second one near the apex of the RV and a third one in a coronary sinus branch on the epicardial side of the LV, typically near the base of the lateral LV wall. The CRT subjects imaged in this study had an underlying LBBB, a condition in which the conduction through the Purkinje fiber network connecting the atrio-ventricular node to the LV (i.e., the left bundle branch) is impeded.

EWI with ACT was performed in three subjects during either sinus rhythm, LV epicardial pacing only, or RV pacing only, in three (n=3) subjects with NYHA class I non-ischemic cardiomyopathy (Subject 1), NYHA class IV non-ischemic cardiomyopathy (subject 2), and NYHA class III ischemic cardiomyopathy (subject 3) (**Figure 7-3**). Only the four-chamber view was acquired. In all three subjects, the EW originated on the epicardium of the LV lateral wall during LV epicardial pacing (**Figure 7-3**A,D,G) and at the apex of the RV during RV pacing (**Figure 7-3**B,E,H). During sinus rhythm, the septum and the RV wall were activated prior to the LV lateral wall (**Figure 7-3**C,F,I). The time required for both ventricles to be electromechanically activated varied significantly, from under 100 ms (e.g., Subject 1 during RV pacing and sinus rhythm, **Figure 7-3**B,C), to over 200 ms (e.g., Subject 1 during LV epicardial pacing, **Figure 7-3**A, and Subject 3 in all pacing schemes, **Figure 7-3**G,H,I). More specifically, during LV epicardial pacing, the transmural EW propagation originated from the epicardium of the lateral wall in all three subjects. In subjects 1 and 3 (**Figure 7-3**A,G), the earliest activation was located on the epicardium of the lateral wall

near the base. In Subject 2 (**Figure 7-3**D), the earliest electromechanical activation was detected on the epicardium at half the distance from apex to base. During RV pacing, the earliest electromechanical activation was located near the apex in all three subjects, either at the apex (**Figure 7-3**B), in the septum (**Figure 7-3**E), or on the RV wall (**Figure 7-3**H). Finally, during sinus rhythm, the EW originated from multiple locations in the septum and the RV wall (as opposed to the sole site when pacing), with the RV and septal walls being electromechanically activated prior to the lateral wall in all cases. In Subject 1, one early activation site was mapped in the basal region of the septum (**Figure 7-3**C); in Subjects 2 and 3, two sites were identified at the basal and apical regions of the septum (**Figure 7-3**F,I). In subjects 2 and 3, the strains measured in the lateral wall remained minute (**Figure 7-3**, black region), i.e., the myocardial region shown in black did not contract. Remarkably, these regions underwent large strains when the heart was paced.

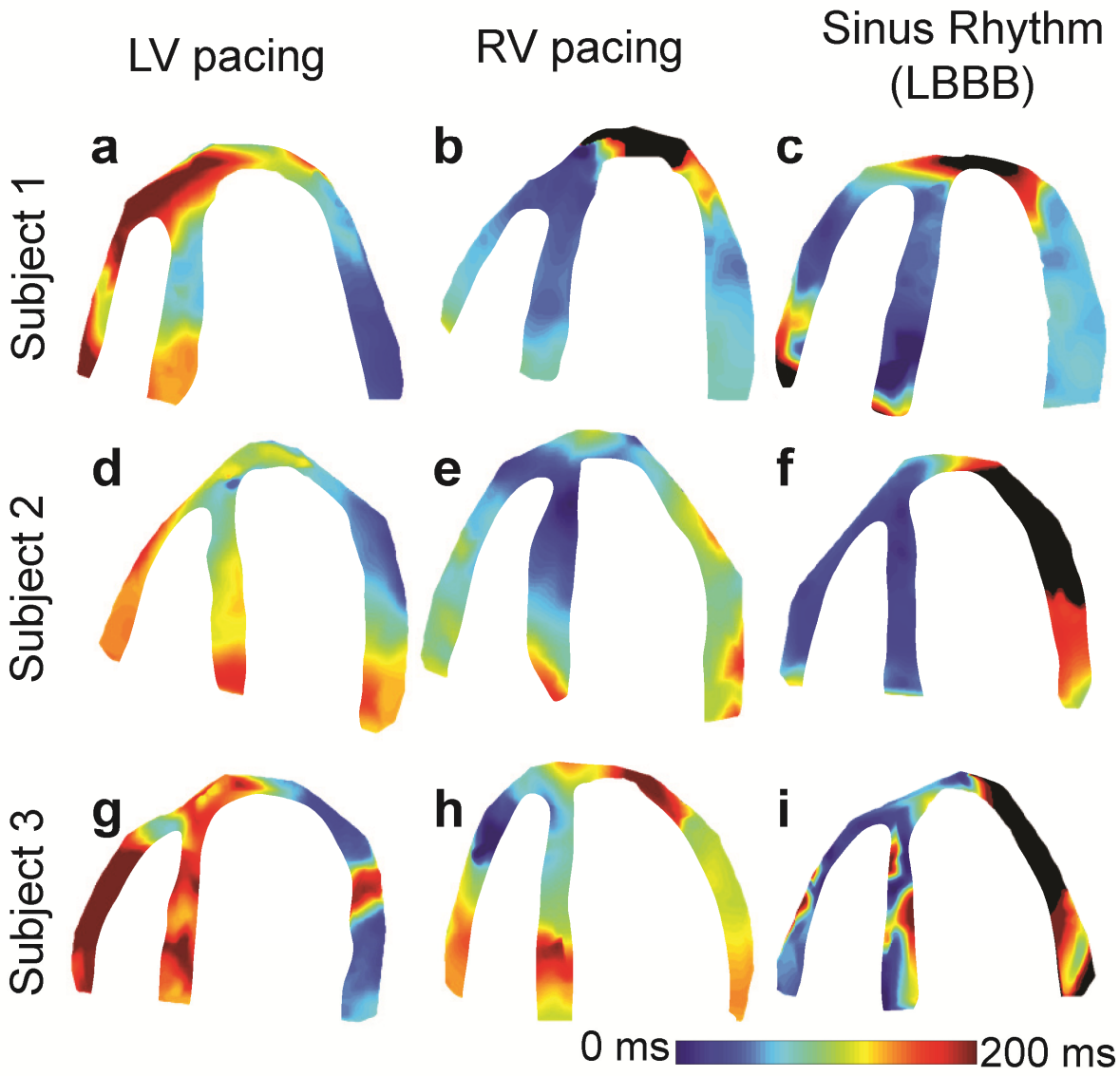

Figure 7-3 Ventricular EWI isochrones of three CRT patients with LBBB during RV pacing, LV pacing and sinus rhythm. Electromechanical activation times could not be obtained in blackened regions. All three patients presented similar activation patterns: from the right ventricular apex during RV pacing, from the epicardium of the LV lateral wall during LV pacing. During sinus rhythm, the right ventricle was electromechanically activated rapidly, followed by the LV lateral wall. Large portions of the LV lateral wall were not electromechanically activated in two cases (black region, patients 2 & 3).

7.4.2 Discussion

In accordance with our previous results in canines, EWI was capable of identifying the pacing location in either the right or left ventricle consistently. Similarly, in patients with LBBB, the electrical activation of the ventricles becomes dyssynchronous: the RV is activated rapidly via the Purkinje network, while the LV is activated via the cell-to-cell myocardial conduction system. In the LV, subjects with LBBB have either one or two sites of early activation, typically located midway between apex and base in the septum, in the apical region of the septum or in the basal region of the anterior wall. The last region of activation in the LV is typically located in the posterior or lateral wall (Vassallo et al., 1984). These propagation features were also observed in the CRT patients during sinus rhythm, although in two of them, a region of no or little contraction was observed in the lateral wall. Such a phenomenon was also observed during acute ischemia in canines (Section 6.2); remarkably, it is in the patients at advanced stages of heart failure (class III and IV) that this absence of contraction was observed, and was reversed when the heart was paced. Further study of this electromechanical re-activation during pacing could be a promising avenue in the study of the success mechanisms of CRT.

7.5 Atrial Flutter

7.5.1 Results

AFL is an atrial tachyarrhythmia that arises due to a reentrant circuit in either the RA or LA. A reentrant circuit produces a localized, self-perpetuating electrical activation that results in rapid atrial excitation. AFL can often be treated effectively with radio-frequency (RF) ablation. In the current study EWI with ACT was performed in two subjects with AFL, immediately prior to a

scheduled mapping and ablation procedure (Figure 7-4) and with parallel beamforming in one subject.

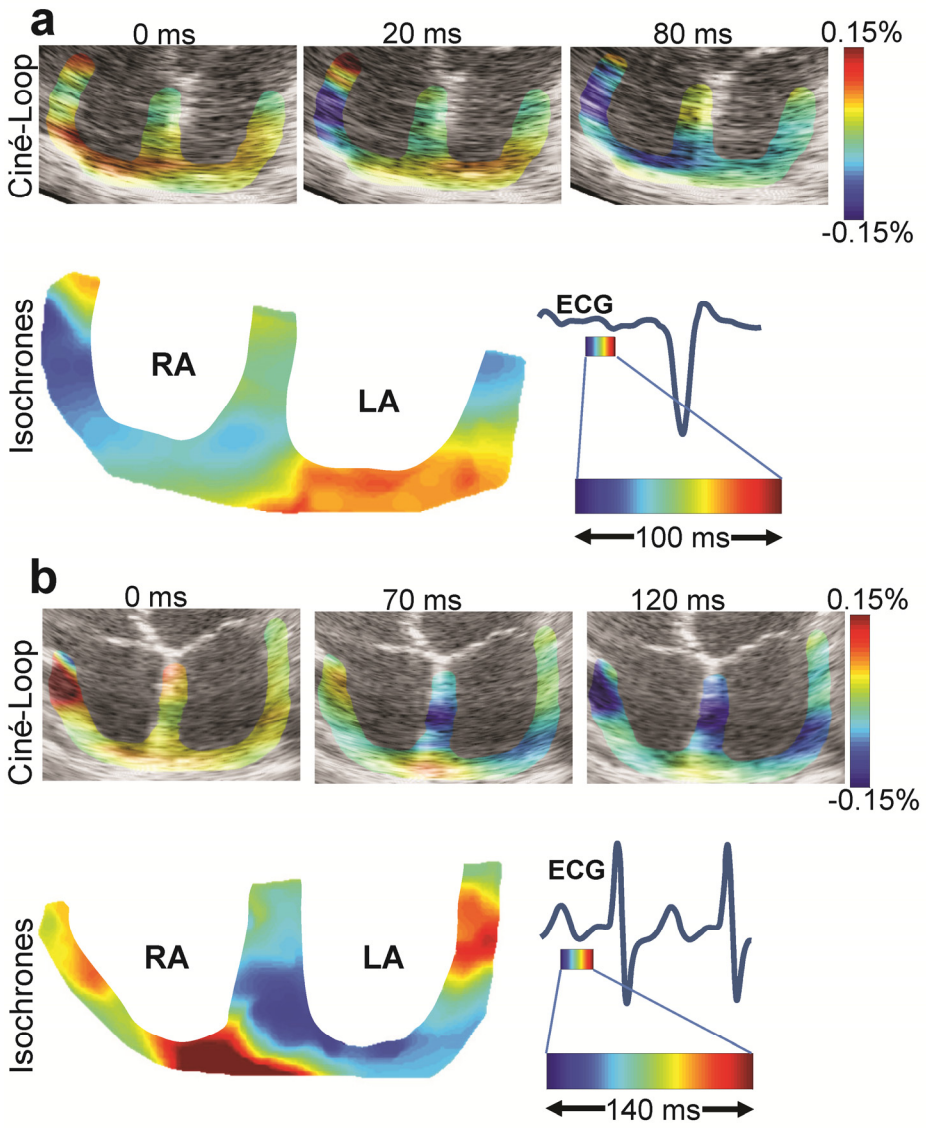

Figure 7-4 EWI ciné-loop and isochrones during atrial flutter (a) EWI ciné-loop and isochrones of a patient undergoing typical right-atrial flutter. The EW originated in the lateral wall of the RA (20 ms) and propagated towards the septum and the LA (80 ms). EWI isochrones also depict this propagation pattern in greater details. (b) EWI ciné-loop and isochrones of a patient undergoing atypical left-atrial flutter. In this case, the EW originated in the left endocardium of the septum, and propagated in the LA (70 ms), before reaching the RA (120 ms). EWI isochrones also depict this propagation pattern in greater details.

The intracardiac electrical mapping procedure indicated that the patients had right (**Figure 7-4**a) and left AFL (**Figure 7-4**b), respectively. In the subject with right AFL, the results of the activation sequence mapping demonstrate the close correlation between EWI and the electrical activation sequence (**Figure 7-5**). Indeed, in both EWI (**Figure 7-4**a) and electrical mapping (**Figure 7-5**), propagation from the tricuspid valve toward the superior wall in the lateral wall of the RA is observed, with the activation of the septum occurring from the superior wall towards the tricuspid valve. In the subject with left AFL (**Figure 7-4**b), the EW propagated from the LA to the RA. More specifically, the EW originated in the left side of the septum, propagated towards the superior wall of the LA and finally reached the RA. The ablation site that led to successful termination was located at the right-inferior pulmonary vein. Again, this specific site was not imaged for EWI mapping. In both cases, the propagation was repeated at each P-wave confirming the reproducibility of EWI.

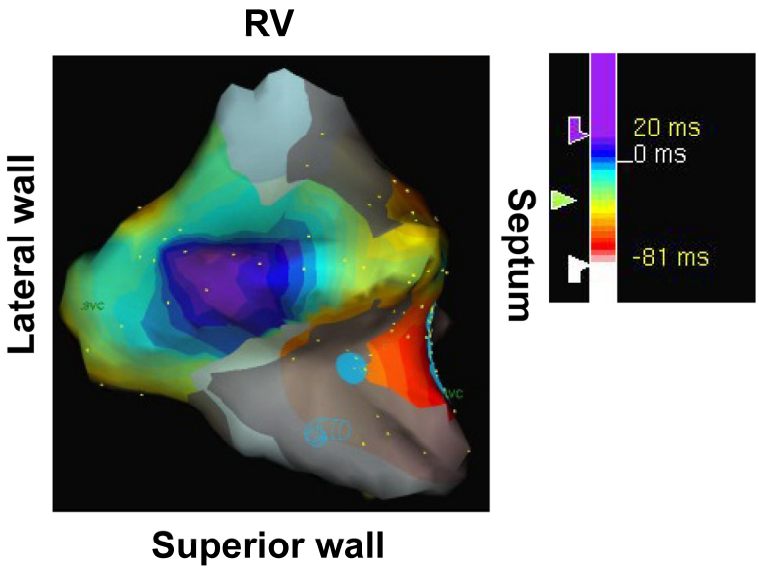

Figure 7-5 Electrical activation mapping of the right atrium corresponding to Figure 7-4 a

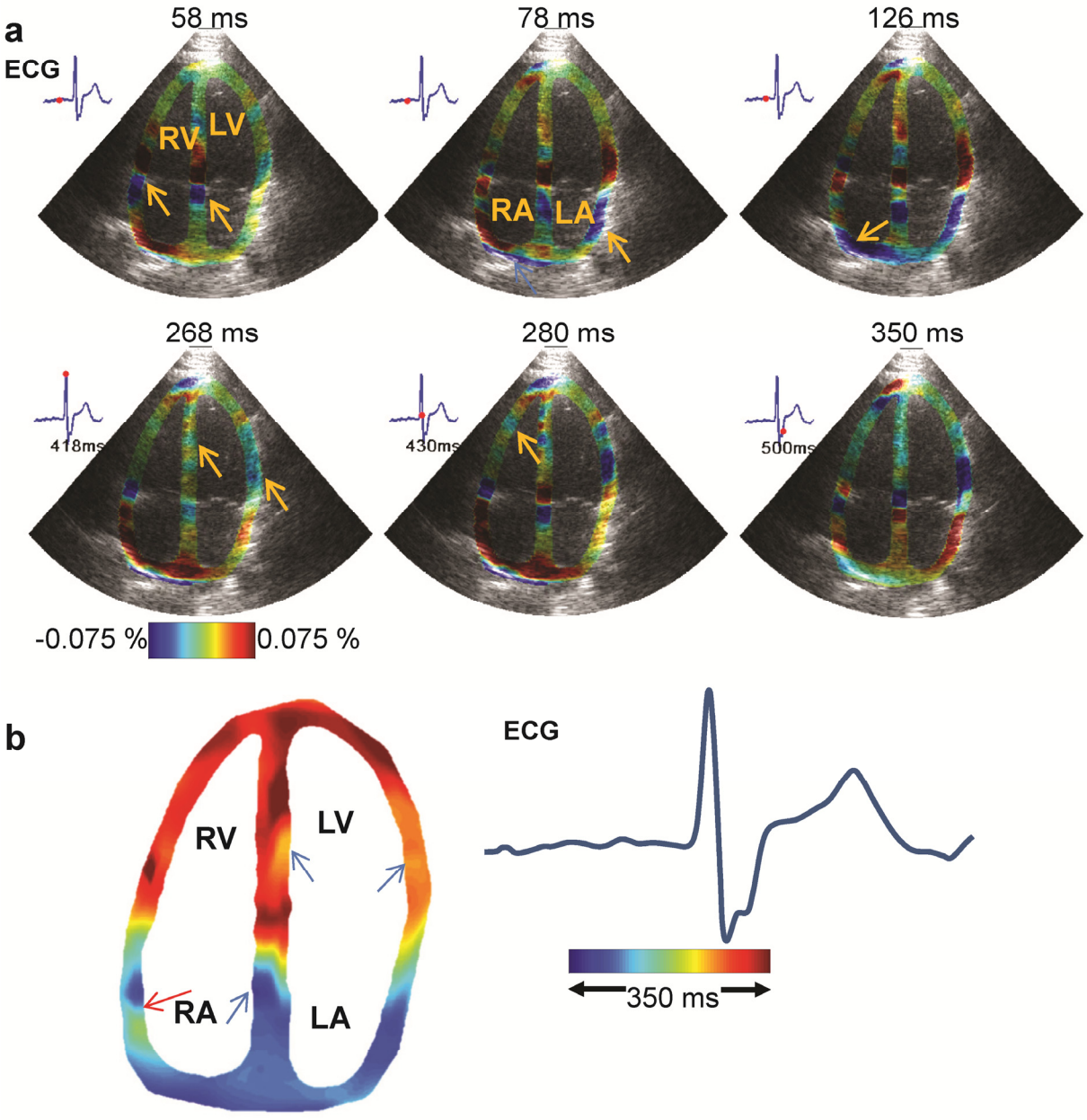

Figure 7-6 Single-heartbeat EWI (a) ciné-loop and (b) isochrones of a patient during atrial flutter and RBBB. In the atria, activation originated from the atrial septum and right atrial lateral wall and propagated in the superior wall of the RA and in the LA. A region of slow conduction could be identified (red arrow). The ventricular EW was initiated at the mid-level of the septum, and propagated in the LV lateral wall. The RV wall was activated last. Arrows in (a) indicates regions undergoing activation.

EWI with parallel beamforming (virtual-source sequence) was applied to a subject with typical right AFL and RBBB (**Figure 7-6**). The EWI isochrones (**Figure 7-6**B) were used to identify a region of slow conduction (red arrow). This site was located in the vicinity of the successful ablation site in this patient - the slow-conducting cavo-tricuspid isthmus. In the ventricles, regions of early activation were observed at the mid-level of the septum and near the base in the left lateral wall (**Figure 7-6**A). Unlike in the normal case (**Figure 7-2**E), the EWI isochrones (**Figure 7-6**B) show that activation of the RV wall occurs near the base, and later than in the LV lateral wall, in accordance with the expected propagation pattern during RBBB (Fantoni et al., 2005).

7.5.2 Discussion

These results demonstrate the capability of EWI to characterize atrial arrhythmias for the first time in humans. The propagation patterns observed were consistent with atrial flutter in all cases; moreover, EWI maps were in accordance with cardiac mapping in one case, and with the ablation site in another. The lack of cardiac mapping in two cases is due to the fact that they were not performed in a comprehensive manner before ablation was performed in these patients, in order to reduce the procedure length and potential risks and illustrate the need for a noninvasive method to map the electrical activation of the heart. Indeed, accurate activation maps can improve the success rate of ablation in atrial flutter (Shah et al., 1999).

7.6 Summary

The objectives of this study were (1) to determine the potential for clinical role of EWI, by predicting activation patterns in normal subjects, (2) to determine the feasibility of EWI to

identify the site of origin in subjects with tachyarrhythmia, and (3) to identify the myocardial activation sequence in patients undergoing CRT. In normal subjects (**Figure 7-2**), the EW propagated, in both the atria and the ventricles, in accordance with the expected electrical activation sequences based on reports in the literature. In subjects with CRT (**Figure 7-3**), EWI successfully characterized two different pacing schemes, i.e., LV epicardial pacing and RV endocardial pacing versus sinus rhythm with conducted complexes. In two subjects with AFL (**Figure 7-4**), the propagation patterns obtained with EWI were in agreement with results obtained from invasive intracardiac mapping studies, indicating that EWI may be capable of distinguishing LA from RA flutters transthoracically. Finally, we have shown the feasibility of EWI to describe the activation sequence during a single heartbeat in a patient with AFL and RBBB (**Figure 7-6**).

Over the past decade, morbidity and mortality associated with heart disease such as ischemia have decreased while the prevalence of heart failure has significantly increased (Braunwald et al., 2004). One third of subjects with heart failure also have dyssynchrony due to LBBB (Clark et al., 2008). CRT, which uses biventricular pacing to correct this dyssynchrony, is an evolving therapy that has led to lower mortality and improved clinical status (Cleland et al., 2005). However, approximately 30% of subjects show no functional benefit after implantation (Gregoratos et al., 2002). This limited success likely reflects both an incomplete understanding of basic mechanisms as well as inadequate tools for optimizing the use and programming of existing pacing therapies. As we show in this study, EWI characterized each pacing scheme in accordance with the expected electrical activation sequence, i.e., in a unique and predicted

fashion. Although validation against mapping in the human ventricle is beyond the scope of this feasibility study, animal experiments predict a strong correlation between the electrical and electromechanical activation times. These results indicate that EWI might be used as an accurate surrogate to invasive intracardiac mapping. The availability of this information has the potential to guide optimization of CRT and device programming. Optimization of device programming is frequently not pursued by practitioners, in large part due to lack of effective tools and methodologies (Turcott et al., 2010). EWI could be uniquely positioned to provide critical information for these purposes, given that it is noninvasive, non-ionizing, low-cost, and can be readily implemented in most ultrasound scanners already available at the point of care.

ECG recordings have limitations in the determination of specific atrial tachyarrhythmia mechanisms. In patients who have undergone a previous catheter procedure, the surface ECG may not be helpful in distinguishing LA from RA flutters (Bochoeyer et al., 2003; Garan, 2008). Intracardiac mapping and ablation procedures for LA and RA flutters can differ significantly with regard to complexity, procedural risk, anticipated success rates, appropriate patient selection and requirements for pre-procedural planning(De Ponti et al., 2006; Barbato et al., 2008). The results of our study show that EWI could potentially aid in clinical decision-making by identifying the chamber of origin of AFL prior to any invasive procedure. Future applications of EWI could theoretically be expanded to include insights with regard to specific arrhythmia mechanism (i.e., macro reentry vs. focal atrial tachycardia) and transmural localization of likely sites for successful ablation (e.g., epicardial vs. endocardial site of ongoing ventricular tachycardia).

Limitations to this feasibility study include the small number of subjects for each condition. This choice was made to assess the versatility of the methodology, i.e., the capability of EWI to map different types of abnormal rhythms in all four chambers. Additionally, while the capability of EWI to map ventricular activation times during pacing has been shown in animal models, further studies involving complete electrical mapping and larger groups of subjects will be necessary to validate the proposed clinical applications in the atria. The characterization of a subset of rhythms with EWI may also require the use of three-dimensional maps; while this can be compensated with the use of multiple planes (**Figure 7-1**), using 3-D ultrasound in a single heartbeat would be advantageous and theoretically possible but would require additional technical developments to achieve sufficient frame rates. In addition, as observed in the AFL cases of this study, the ventricular contraction can, by pre-stretching the atria, modify activation times. This limitation can be circumvented simply by mapping the atrial contraction during ventricular diastole. Finally, this technique relies on transthoracic ultrasound imaging for which the image quality can be limited in patients with poor acoustic windows or who are overweight, although the EWI methodology could be implemented with transesophageal or intra-cardiac probes.

7.7 Conclusion

The results of this chapter demonstrate for the first time that mapping the transient strains occurring in response to the electrical activation, i.e., the electromechanical wave propagation, can be used to characterize both normal rhythm and arrhythmias in humans, in all four cardiac chambers transthoracically using multiple and single-heartbeat methodologies. EWI has the potential to noninvasively assist in clinical decision-making prior to invasive treatment, and to aid in optimizing and monitoring response to CRT. Before EWI can be brought into the clinic, however, a number of developments must or could be achieved. They are described in Chapter 8.

Chapter 8 Summary and Future Work

8.1 Summary

In this dissertation, we introduced a novel imaging modality, Electromechanical Wave Imaging (EWI), for the noninvasive and transmural characterization of electrical and electromechanical events in the myocardium.

A novel method to measure the signal-to-noise ratio of the electromechanical wave (EW) (Section 3.6; Provost et al., 2012) was also implemented and used to define three key technical requirements necessary to perform EWI: high frame rate, full field of view, and high beam density. Three different strategies were then devised to achieve those requirements: the automatic composite technique (Section 4.2; Wang et al., 2008; Provost et al., 2010), the temporally unequispaced acquisition sequence (Section 4.3; Provost et al., 2012), and parallel beamforming (Section 4.4; Provost, Nguyen, et al., 2011). The choice between these techniques can be made based on the equipment available (conventional or modern clinical scanner) and the phenomenon to be observed (single or multiple-heartbeat acquisition) with different trade-offs in terms of frame rates and image resolution, while always respecting minimum requirements.

In vivo experiments involving 10 canines were conducted to establish the correlation between the electrical and electromechanical activation times in normal canines and show the reproducibility of the method including in the clinically relevant closed-chest setting in conscious canines (Sections 5.2 and 6.5; Konofagou and Provost, 2011, 2012; Konofagou et al., 2011; Provost, Lee, et al., 2011a; Provost, Nguyen, et al., 2011). A novel *in-vivo-in-silico*

framework was also developed to validate EWI against quantities that cannot be obtained or are difficult to obtain *in vivo*, i.e., high-resolution transmural electrical activation sequence, and the full, noise-free 3-D strain tensor. This framework was used to confirm experimental measurements showing a strong correlation between the electrical and electromechanical activations, to extend this validation to the transmural propagation, and to demonstrate the angle-independence of EWI (Section 5.3; Provost, Gurev, et al., 2011).

To establish the validity of EWI in diseased hearts, *in vivo* experiments involving 10 canines were performed. The propagation of the EW was shown to be blocked in the ischemic region, indicating that EWI could be used to detect ischemia at early stages, but also that EWI may not be capable of mapping the electrical activation in ischemic regions (Section 6.2; Provost et al., 2010). During left bundle branch block, the EW maintained its propagation and was in good agreement with cardiac mapping (Section 6.3). During ventricular fibrillation, the dominant frequencies mapped with EWI were also in good agreement with electrical mapping, indicating that EWI could potentially be used to identify arrhythmogenic zones (Section 6.4). Finally, EWI was shown capable of mapping propagation in all four chambers of the heart during atrioventricular dissociation, a common condition in humans undergoing cardiac resynchronization therapy (CRT) (Section 6.5; Provost, Nguyen, et al., 2011).

Finally, the feasibility and clinical relevance of EWI in humans was demonstrated in a study involving 11 human subjects. Indeed, the normal transmural activation sequence was, for the first time, mapped in conscious, normal human subjects (Section 7.3; Provost, Lee, et al.,

2011a). EWI was also applied in CRT and was found capable of identifying the pacing origin. In patients with advanced cardiomyopathy, regions that were not electromechanically activated during sinus rhythm were found to undergo the EW when pacing the heart, indicating that EWI could be used to further our understanding of the response to CRT. Finally, the capability of EWI to map macro-reentrant circuits was demonstrated in patients with atrial flutter and validated, in one patient, against cardiac mapping (**Figure 7-5**).

8.2 Future Work

8.2.1 Introduction

A number of improvements could be made to overcome obstacles currently preventing EWI from being implemented on a wide scale or to enhance EWI capabilities. This section aims at providing a description of the developments believed to be necessary or useful in translating EWI to the clinic.

8.2.2 Real-time Implementation

Most of the currently implemented processing to perform EWI can be done at a fast rate. For example, immediately following image acquisition in the automated composite technique (ACT), an experienced operator can obtain the EWI ciné-loop and isochrones in less than fifteen minutes with the current, non-optimized, interpreted (as opposed to compiled), and not fully automated implementation. An interesting avenue for EWI would be a real-time implementation, i.e., either overlaying the EW during acquisition, or obtaining the EWI ciné-loop and isochrones a few seconds after the end of acquisition. The latter option is more viable for EWI for two reasons: 1) interleaving processing during acquisition will inevitably reduce the

frame rate; and 2) the EW propagates too fast for the human eye to follow at the acquisition frame rate. Indeed, for the human eye to track the EW, it is necessary to display the EWI-ciné loop acquired at a high frame rate, e.g., 500 Hz, at a video frame rate that the eye can appreciate, e.g., 25 Hz. In other words, to display an EW occurring over 0.3 s, the corresponding EWI ciné-loop will last 500/25*0.1 = 6 s.

Among the three EWI methods developed in this dissertation, the most computationally intensive is the parallel beamforming (Section 4.4) approach since the radio-frequency (RF) frames must be generated from the element data. Therefore, we explore here strategies to increase processing speed only for this method, as the results can be directly applied to ACT (Section 4.2) and the temporally unequispaced acquisition sequence (TUAS) (Section 4.3) and perform even faster in these cases. We have implemented the image formation algorithm, motion and strain estimation, scan conversion and overlay using a Tesla GPU (Nvidia, Santa Clara, CA) and the Matlab parallel processing toolbox (The Mathworks, Nattick, MA). Although some key functions were not optimized for the GPU (for instance, the cross-correlation and the scan-conversion algorithms (Section 4.5)), it was possible to generate a 300-ms EWI ciné-loop (64 RF lines, 80% overlap) with a temporal resolution of 2 ms in 21 s. Since displaying the ciné-loop requires 6 s, it means that the operator needs to wait 15 s after segmenting the first frame of interest to observe the EW propagation. Given that this process remains sub-optimal, it is reasonable to claim that it is possible to generate the EWI ciné-loop on-line, after a negligible delay following the acquisition.

Another important bottleneck in the EWI process is the generation of isochrones. In its current implementation, isochrones generation requires the operator to select regions (or pixels) of the heart and identify the zero-crossing time for each. While such an approach ensures a minimal number of spurious values, it is user dependent and slow. We have implemented an automatic isochrones generation algorithm based on cross-correlation of strain time series which led to the results of Section 5.3 (**Figure 5-12**). Briefly, this method consisted in detecting the shift in zero crossing time of neighboring pixels with cross-correlation and required the selection of one or multiple seeds. After selecting the seeds, the isochrones are generated in a neighbor-to-neighbor fashion. For example, if one seed was selected in the lateral wall and another in the septum, the regions of calculated isochrones grew by one pixel per iteration and eventually met each other. The continuity of the connection was then used as an indicator of success of the method. While this method is fast, it was found to not be robust and often required multiple initiations (with different seeds locations) to achieve continuous isochrones. This is believed to be due to cumulative errors (large dependence on the selected seed) and to the rapid change of wave form as the axial direction of the beam spatially transitions from being aligned with one heart coordinate to another, e.g., from the radial coordinate to the longitudinal coordinate. Higher beam density or 2-D estimation of displacement and the mapping of the 2-D strain tensor could potentially be used to avoid those transitions (for example, by tracking the zero-crossings of longitudinal strains instead of axial strains) and allow the use of automatic isochrones generation.

To simplify the user interface, another approach would consist in showing only the strains corresponding to electromechanical activation (e.g., negative in an apical view) with a large threshold around zero to limit false positive measurements. We have developed such an approach (Provost, Lee, et al., 2011a, 2011b) but have not validated it against electrical mapping (**Figure 8-1**). As this approach requires substantial filtering and thresholding, it is expected to be less accurate, but constitutes a reasonable trade-off that results in ciné-loops that are easier to understand and allows the fast, automatic generation of isochrones.

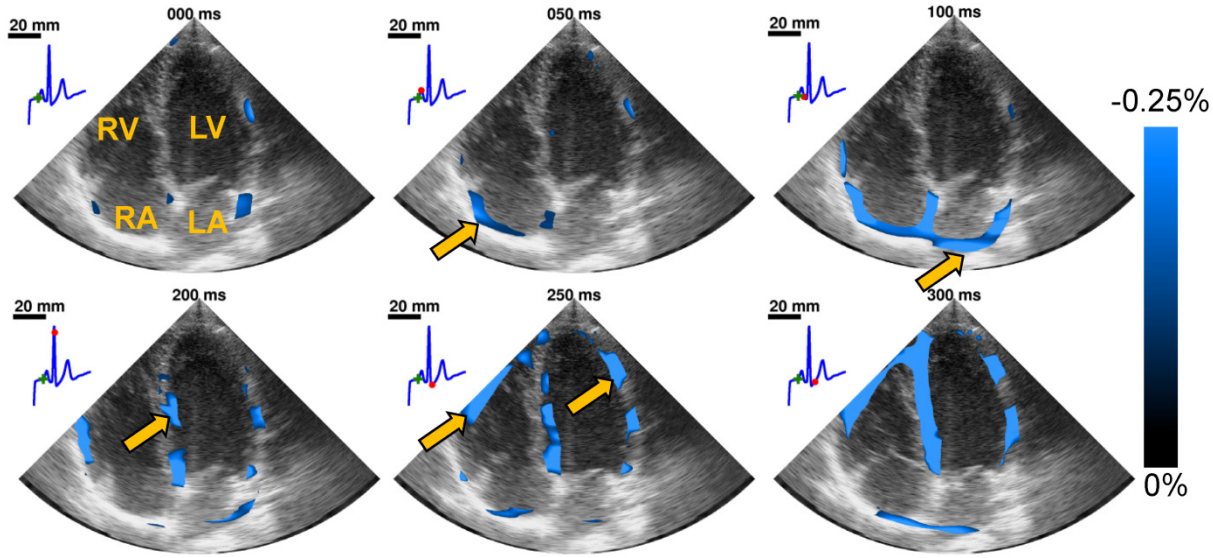

Figure 8-1 Electromechanical Activation ciné-loop during sinus rhythm in a human subject. Only strains corresponding to activation are displayed. Activation originated in the right atrium and propagated into the left atrium before reaching the ventricles during the QRS complex from multiple origins. Artifacts are visible at 0 ms where activation is displayed, although the heart is not undergoing electrical activation.

8.2.3 Three-dimensional EWI

Mapping the electrical activation in three dimensions is critical to identifying arrhythmogenic zones in the myocardium. We implemented a multi-plane representation to address this need

(e.g., **Figure 5-8**). However, single-heartbeat, high-resolution, 3-D electromechanical wave maps could significantly improve the diagnosis potential of EWI. The developments described in this dissertation related to using 2-D diverging waves emanating from a 2-D virtual point-source to image the heart (Section 4.4) are expected to be translated in a straightforward manner to 3-D imaging. Indeed, using a 2-D array, it is possible to steer ultrasound beams in any solid angle. Therefore, one could consider the emission of a spherical wave from a virtual point-source to insonify the entire heart and use a dense matrix of elements to reconstruct images in a pixel-wise fashion, similar to the methods developed herein (Section 4.4). In comparison to a circular wave, a spherical wave suffers a faster geometrical attenuation. However, since the biosafety standards for ultrasound limit mostly peak pressures, it is likely that much higher levels of power could be used while remaining safe for the patients and ensure a high image signal-to-noise ratio (Section 4.4.3). In the event that it is not the case, an approach combining limited-aperture focusing in one dimension (e.g, elevational) and a virtual point-source in the other dimension (e.g., lateral) in a TUAS framework could allow a higher signal-to-noise ratio at the cost of a reduction in motion-sampling rate. In summary, the strategies developed for parallel imaging in this dissertation could be applied in a straightforward manner to 3-D imaging while maintaining the same frame rates.

8.2.4 Further validation of EWI against electrical mapping

The validation of EWI against electrical mapping performed in this dissertation has many limitations that could be overcome. For example, the number of animals used could be increased to quantify, with statistical significance, the linear relationship between the electrical and electromechanical activations and how it varies according to the type of activation (sinus

rhythm, number of pacing sites, the presence of disease, etc.). Moreover, only acute conditions were studied, while most of the clinical cases of interest typically involve chronic conditions such as heart failure. The development of a basket catheter mapping system could allow such study; indeed, the catheter can be inserted in a minimally invasive manner in a canine under fluoroscopy (Section 6.3), and EWI can be performed in a closed-chest setting (Section 6.5), thus allowing longitudinal studies of both the electrical and electromechanical activations. Finally, the precise co-registration of EWI with the basket catheter remains an open problem and greatly affects the correlation results (Section 5.2.2). Three-dimensional ultrasound could also be useful for that purpose. Additionally, it is possible that strains acquired at high frame rates are correlated not only with the depolarization of the heart, but also with its repolarization. The repolarization sequence and its heterogeneity are linked to a number of conditions (Hlaing et al., 2005) and could become another application of EWI.

The basket catheter system could also be improved by including the measurement of unipolar signals, as it was originally designed (**Figure 5-3**). Unipolar signals have the advantage of being omnidirectional (Sevaptsidis et al., 1992), unlike bipolar signals that measure the electrical activation in a specific direction (i.e., along the vector connecting two electrodes). Using unipolar signals, one can reconstruct bipolar signal in multiple directions since a bipolar signal can be obtained from the subtraction of two unipolar signals. The resulting mapping resolution is therefore increased (**Figure 8-2**), and mapping the wave front of the electrical activation and its main propagation direction becomes possible by computing the 2-D gradient of activation times.

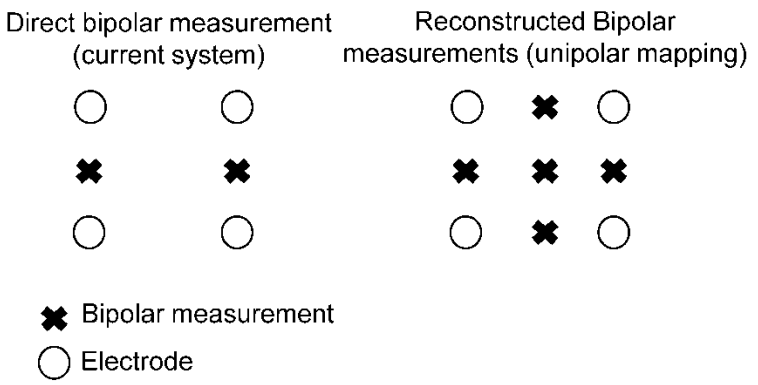

Figure 8-2 Direct and reconstructed bipolar measurements. Reconstructed bipolar measurements can be obtained from unipolar measurements and can increase the mapping resolution when using an electrode grid such as a basket catheter.

Thorough validation in humans is probably one of the most important future studies to conduct. It can be done by constructing full electrical activation maps in patients and comparing them with transthoracic EWI maps, although co-registration between the two modalities (EWI and electrical mapping) might limit the quality of the data. Another approach would consist of implementing EWI in an intra-cardiac probe, which can be co-registered with good accuracy in current clinical scanners (e.g., CARTOSOUND Image Integration Module with 3-D SOUNDSTAR Catheter, Biosense Webster, CA).

8.2.5 Clinical applications

EWI could be useful for the characterization of a number of diseases that can be treated with ablation therapy: e.g., atrial fibrillation, ventricular tachycardia, Wolff-Parkinson-White (WPW) syndrome, premature ventricular contractions (PVC), etc. Ventricular tachycardia can be caused by a reentry circuit near an old infarct. Current challenges include the determination of the transmural location of the successful ablation site; epicardial ablations are less common and are a more difficult procedure (Sacher et al., 2010). WPW is a heart condition where an additional

electrical pathway links the atria to the ventricles. In PVC, automaticity or reentry cause the ventricles to contract preemptively. PVC can also be treated with ablation, but knowing the location of the potential ablation sites prior to catheterization would help plan and limit the risks of the procedure. In all of these cases, EWI has the potential to help in noninvasively determining the transmural location of potential ablation sites.

8.3 Conclusion

This dissertation explored the development, validation, and clinical feasibility of EWI, which constitutes a unique tool for noninvasively evaluating the cardiac electromechanical function of the heart. The ubiquity of ultrasound scanners in diagnostic cardiology indicates the important translational aspects of EWI. Mapping the transient strains occurring in response to the electrical activation, i.e., the electromechanical wave propagation, can be used to characterize both normal rhythm and arrhythmias in humans transmurally, in all four cardiac chambers transthoracically using multiple and single-heartbeat methodologies. EWI therefore offers the potential to noninvasively assist in clinical decision-making prior to invasive treatment, as well as for treatment monitoring, at the point of care and in real time.

List of Publications Related to the Thesis

Peer-reviewed Journals

1. Wang, S., Lee, W.-N., **Provost, J.**, Luo, J., and Konofagou, E. E. A composite high-frame-rate system for clinical cardiovascular imaging. IEEE Transactions on Ultrasonics, Ferroelectrics and Frequency Control, *55*, 2221-2233, 2008. (Chapter 4)
2. **Provost, J.**, Lee, W.-N., Fujikura, K., and Konofagou, E. E. Electromechanical Wave Imaging of Normal and Ischemic Hearts *in vivo*. IEEE Trans. Med. Imaging *29*, 625-635, 2010. (Chapters 4, 5, 6)
3. Konofagou, E., Lee, W.-N., Luo, J., **Provost, J.**, and Vappou, J. Physiologic Cardiovascular Strain and Intrinsic Wave Imaging. Annu. Rev. Biomed. Eng. *13*, 477-505, 2011. (Chapters 5, 6)
4. Lee, W.-N., **Provost, J.**, Fujikura, K., Wang, J., and Konofagou, E. E. *In vivo* study of myocardial elastography under graded ischemia conditions. Physics in Medicine and Biology *56*, 1155-1172, 2011. (Chapter 6)
5. **Provost, J.**, Gurev, V., Trayanova, N., and Konofagou, E. E. Mapping of cardiac electrical activation with electromechanical wave imaging: An in silico-*in vivo* reciprocity study. Heart Rhythm *8*, 752-759, 2011. (Chapter 5)
6. **Provost, J.**, Lee, W.-N., Fujikura, K., and Konofagou, E. E. Imaging the electromechanical activity of the heart *in vivo*. Proceedings of the National Academy of Sciences. vol. 108, no. 21, pp. 8565–8570, 2011. (Chapters 5, 7)
7. **Provost, J.**, Nguyen, V.T.-H., Legrand, D., Okrasinski, S., Costet, A., Gambhir, A., Garan, H., and Konofagou, E.E. Electromechanical wave imaging for arrhythmias. Physics in Medicine and Biology *56*, L1–L11, 2011. (Chapters 4, 5, 6)
8. Hariharan, V., **Provost, J.**, Shah, S., Konofagou, E.E., and Huang, H. Elevated Strain and Structural Disarray Occur at the Right Ventricular Apex, Cardiovascular Engineering and Technology, *3*, 52-61, 2012. (Chapter 5)
9. Konofagou, E.E., **Provost, J.**, Electromechanical wave imaging for noninvasive mapping of the 3D electrical activation sequence in canines and humans *in vivo*. Journal of Biomechanics, *45*, 856-864, 2012. (Chapters 5, 6)
10. **Provost, J.**, Thiébaut, S., Luo, J., and Konofagou, E. E. Single-Heartbeat Electromechanical Wave Imaging with Optimal Strain Estimation Using Temporally Unequispaced Acquisition Sequences. Physics in Medicine and Biology, *57*, 1095-1112, 2012. (Chapters 3, 4, 6)
11. **Provost, J.,** Gambhir, A., Vest, J., Garan, H., Konofagou, E.E. Electromechanical Wave Imaging of the heart during normal and abnormal rhythms in humans. Submitted. (Chapter 7)

Book Chapter

12. Konofagou, E. and **Provost, J.** (2011). Evolving concepts in measuring ventricular strain in canine and human hearts: noninvasive imaging. In Cardiac Mechano-Electric Coupling and Arrhythmias (Oxford: Oxford University Press). (Chapters 5, 7)

References

Aletras, A.H., Ding, S., Balaban, R.S., Wen, H., 1999. DENSE: Displacement Encoding with Stimulated Echoes in Cardiac Functional MRI. Journal of Magnetic Resonance 137, 247–252.

Alla, F., Zannad, F., Filippatos, G., 2007. Epidemiology of acute heart failure syndromes. Heart Failure Reviews 12, 91–95.

Ashikaga, H., Coppola, B.A., Hopenfeld, B., Leifer, E.S., McVeigh, E.R., Omens, J.H., 2007. Transmural Dispersion of Myofiber Mechanics: Implications for Electrical Heterogeneity In Vivo. Journal of the American College of Cardiology 49, 909–916.

Azar, R.Z., Baghani, A., Salcudean, S.E., Rohling, R., 2010. 2-D high-frame-rate dynamic elastography using delay compensated and angularly compounded motion vectors: Preliminary results. Ultrasonics, Ferroelectrics and Frequency Control, IEEE Transactions on 57, 2421–2436.

Badke, F.R., Boinay, P., Covell, J.W., 1980. Effects of ventricular pacing on regional left ventricular performance in the dog. Am J Physiol Heart Circ Physiol 238, H858–867.

Baghani, A., Brant, A., Salcudean, S., Rohling, R., 2010. A high-frame-rate ultrasound system for the study of tissue motions. IEEE Trans Ultrason Ferroelectr Freq Control 57, 1535–1547.

Barbato, G., Pergolini, F., Carinci, V., Di Pasquale, G., 2008. Transseptal approach for left atrial arrhythmia ablation in patients with valve prostheses. J Cardiovasc Med (Hagerstown) 9, 273–276.

Belgacem, F.B., 2007. Why is the Cauchy problem severely ill-posed? Inverse Problems 23, 823–836.

Bercoff, J., Tanter, M., Fink, M., 2004. Supersonic shear imaging: a new technique for soft tissue elasticity mapping. IEEE Transactions on Ultrasonics, Ferroelectrics and Frequency Control 51, 396–409.

Bers, D.M., 2002. Cardiac excitation-contraction coupling. Nature 415, 198–205.

Betts, T.R., 2008. Atrioventricular Junction Ablation and Pacemaker Implant for Atrial Fibrillation: Still a Valid Treatment in Appropriately Selected Patients. Europace 10, 425–432.

Bochoeyer, A., Yang, Y., Cheng, J., Lee, R.J., Keung, E.C., Marrouche, N.F., Natale, A., Scheinman, M.M., 2003. Surface Electrocardiographic Characteristics of Right and Left Atrial Flutter. Circulation 108, 60–66.

Bouchard, R.R., Hsu, S.J., Wolf, P.D., Trahey, G.E., 2009. In Vivo Cardiac, Acoustic-Radiation-Force-Driven, Shear Wave Velocimetry. Ultrason Imaging 31, 201–213.

Braunwald, E., Zipes, D.P., Libby, P., Bonow, R., 2004. Braunwald's Heart Disease: A Textbook of Cardiovascular Medicine, Single Volume, 7th ed. Saunders.

Carson, P., Anand, I., O'Connor, C., Jaski, B., Steinberg, J., Lwin, A., Lindenfeld, J., Ghali, J., Barnet, J.H., Feldman, A.M., Bristow, M.R., 2005. Mode of Death in Advanced Heart Failure: The Comparison of Medical, Pacing, and Defibrillation Therapies in Heart Failure (COMPANION) Trial. Journal of the American College of Cardiology 46, 2329–2334.

Cassidy, D., Vassallo, J., Marchlinski, F., Buxton, A., Untereker, W., Josephson, M., 1984.

Endocardial mapping in humans in sinus rhythm with normal left ventricles: activation patterns and characteristics of electrograms. Circulation 70, 37 –42.

Center for Devices and Radiological Health, 2012. Guidance Documents (Medical Devices and Radiation-Emitting Products) - Guidance for Industry and FDA Staff - Information for Manufacturers Seeking Marketing Clearance of Diagnostic Ultrasound Systems and Transducers [WWW Document]. URL http://www.fda.gov/MedicalDevices/DeviceRegulationandGuidance/GuidanceDocuments/ucm070856.htm

Céspedes, I., Huang, Y., Ophir, J., Spratt, S., 1995. Methods for estimation of subsample time delays of digitized echo signals. Ultrason Imaging 17, 142–71.

Chattipakorn, N., Fotuhi, P.C., Chattipakorn, S.C., Ideker, R.E., 2003. Three-dimensional mapping of earliest activation after near-threshold ventricular defibrillation shocks. J Cardiovasc Electrophysiol 14, 65–9.

Chung, E.S., Leon, A.R., Tavazzi, L., Sun, J.-P., Nihoyannopoulos, P., Merlino, J., Abraham, W.T., Ghio, S., Leclercq, C., Bax, J.J., Yu, C.-M., Gorcsan, J., St John Sutton, M., De Sutter, J., Murillo, J., 2008. Results of the Predictors of Response to CRT (PROSPECT) Trial. Circulation 117, 2608–2616.

Clark, A.L., Goode, K., Cleland, J.G.F., 2008. The prevalence and incidence of left bundle branch block in ambulant patients with chronic heart failure. Eur. J. Heart Fail. 10, 696–702.

Cleland, J.G.F., Daubert, J.-C., Erdmann, E., Freemantle, N., Gras, D., Kappenberger, L., Tavazzi, L., 2005. The effect of cardiac resynchronization on morbidity and mortality in heart failure. N. Engl. J. Med. 352, 1539–1549.

Cobbold, R.S.C., 2007. Foundations of Biomedical Ultrasound. Oxford University Press.

Cordeiro, J.M., Greene, L., Heilmann, C., Antzelevitch, D., Antzelevitch, C., 2004. Transmural heterogeneity of calcium activity and mechanical function in the canine left ventricle. Am J Physiol Heart Circ Physiol 286, H1471–1479.

Couade, M., Pernot, M., Messas, E., Bel, A., Ba, M., Hagege, A., Fink, M., Tanter, M., 2011. In vivo quantitative mapping of myocardial stiffening and transmural anisotropy during the cardiac cycle. IEEE Trans Med Imaging 30, 295–305.

D'hooge, J., Konofagou, E., Jamal, F., Heimdal, A., Barrios, L., Bijnens, B., Thoen, J., Van de Werf, F., Sutherland, G., Suetens, P., 2002. Two-dimensional ultrasonic strain rate measurement of the human heart in vivo. Ultrasonics, Ferroelectrics and Frequency Control, IEEE Transactions on 49, 281–286.

De Ponti, R., Cappato, R., Curnis, A., Della Bella, P., Padeletti, L., Raviele, A., Santini, M., Salerno-Uriarte, J.A., 2006. Trans-Septal Catheterization in the Electrophysiology Laboratory: Data From a Multicenter Survey Spanning 12 Years. J Am Coll Cardiol 47, 1037–1042.

Durrer, D., Van Dam, R.T., Freud, G.E., Janse, M.J., Meijler, F.L., Arzbaecher, R.C., 1970. Total Excitation of the Isolated Human Heart. Circulation 41, 899–912.

Edvardsen, T., Skulstad, H., Aakhus, S., Urheim, S., Ihlen, H., 2001. Regional myocardial systolic function during acute myocardial ischemia assessed by strain Doppler echocardiography. J Am Coll Cardiol 37, 726–730.

Ellis, R.M., Franklin, D.L., Rushmer, R.F., 1956. Left ventricular dimensions recorded by sonocardiometry. Circ. Res 4, 684–688.

Epstein, A.E., DiMarco, J.P., Ellenbogen, K.A., Estes, N.A.M., Freedman, R.A., Gettes, L.S.,

Gillinov, A.M., Gregoratos, G., Hammill, S.C., Hayes, D.L., Hlatky, M.A., Newby, L.K., Page, R.L., Schoenfeld, M.H., Silka, M.J., Stevenson, L.W., Sweeney, M.O., 2008. ACC/AHA/HRS 2008 Guidelines for Device-Based Therapy of Cardiac Rhythm Abnormalities: A Report of the American College of Cardiology/American Heart Association Task Force on Practice Guidelines (Writing Committee to Revise the ACC/AHA/NASPE 2002 Guideline Update for Implantation of Cardiac Pacemakers and Antiarrhythmia Devices) Developed in Collaboration With the American Association for Thoracic Surgery and Society of Thoracic Surgeons. J Am Coll Cardiol 51, e1–62.

Fantoni, C., Kawabata, M., Massaro, R., Regoli, F., Raffa, S., Arora, V., Salerno-uriarte, J.A., Klein, H.U., Auricchio, A., 2005. Right and Left Ventricular Activation Sequence in Patients with Heart Failure and Right Bundle Branch Block: A Detailed Analysis Using Three-Dimensional Non-Fluoroscopic Electroanatomic Mapping System. Journal of Cardiovascular Electrophysiology 16, 112–119.

Farb, A., Kolodgie, F., Jenkins, M., Virmani, R., 1993. Myocardial infarct extension during reperfusion after coronary artery occlusion: pathologic evidence. J Am Coll Cardiol 21, 1245–1253.

Faris, O.P., Evans, F.J., Ennis, D.B., Helm, P.A., Taylor, J.L., Chesnick, A.S., Guttman, M.A., Ozturk, C., McVeigh, E.R., 2003. Novel Technique for Cardiac Electromechanical Mapping with Magnetic Resonance Imaging Tagging and an Epicardial Electrode Sock. Ann Biomed Eng. 31, 430–440.

Fuster, V., O'Rourke, R.A., 2008. Hurst's the heart. McGraw-Hill Medical.

Gallagher, J.J., Svenson, R.H., Kasell, J.H., German, L.D., Bardy, G.H., Broughton, A., Critelli, G., 1982. Catheter Technique for Closed-Chest Ablation of the Atrioventricular Conduction System. New England Journal of Medicine 306, 194–200.

Garan, H., 2008. Atypical atrial flutter. Heart Rhythm 5, 618–621.

Ghosh, S., Rhee, E.K., Avari, J.N., Woodard, P.K., Rudy, Y., 2008. Cardiac Memory in Patients With Wolff-Parkinson-White Syndrome: Noninvasive Imaging of Activation and Repolarization Before and After Catheter Ablation. Circulation 118, 907–915.

Gregoratos, G., Abrams, J., Epstein, A.E., Freedman, R.A., Hayes, D.L., Hlatky, M.A., Kerber, R.E., Naccarelli, G.V., Schoenfeld, M.H., Silka, M.J., Winters, S.L., Gibbons, R.J., Antman, E.M., Alpert, J.S., Gregoratos, G., Hiratzka, L.F., Faxon, D.P., Jacobs, A.K., Fuster, V., Smith, S.C., Jr, 2002. ACC/AHA/NASPE 2002 guideline update for implantation of cardiac pacemakers and antiarrhythmia devices: summary article: a report of the American College of Cardiology/American Heart Association Task Force on Practice Guidelines (ACC/AHA/NASPE Committee to Update the 1998 Pacemaker Guidelines). Circulation 106, 2145–2161.

Gurev, V., Constantino, J., Rice, J.J., Trayanova, N., 2010. Distribution of electromechanical delay in the heart: insights from a three-dimensional electromechanical model. Biophys. J 99, 745–754.

Gurev, V., Lee, T., Constantino, J., Arevalo, H., Trayanova, N.A., 2010. Models of cardiac electromechanics based on individual hearts imaging data : Image-based electromechanical models of the heart. Biomech Model Mechanobiol.

Harrigan, R.A., Perron, A.D., Brady, W.J., 2001. Atrioventricular dissociation. The American Journal of Emergency Medicine 19, 218–222.

Heimdal, A., Støylen, A., Torp, H., Skjærpe, T., 1998. Real-Time Strain Rate Imaging of the Left Ventricle by Ultrasound. Journal of the American Society of Echocardiography 11, 1013–1019.

Henry, W.L., DeMaria, A., Gramiak, R., King, D.L., Kisslo, J.A., Popp, R.L., Sahn, D.J., Schiller, N.B., Tajik, A., Teichholz, L.E., Weyman, A.E., 1980. Report of the American Society of Echocardiography Committee on Nomenclature and Standards in Two-dimensional Echocardiography. Circulation 62, 212–217.

Hillman, E.M.C., Bernus, O., Pease, E., Bouchard, M.B., Pertsov, A., 2007. Depth-resolved optical imaging of transmural electrical propagation in perfused heart. Opt Express 15, 17827–17841.

Hlaing, T., DiMino, T., Kowey, P.R., Yan, G.-X., 2005. ECG Repolarization Waves: Their Genesis and Clinical Implications. Annals of Noninvasive Electrocardiology 10, 211–223.

Hodgkin, A.L., Huxley, A.F., 1952. A quantitative description of membrane current and its application to conduction and excitation in nerve. J. Physiol. (Lond.) 117, 500–544.

Holmes, J.W., Borg, T.K., Covell, J.W., 2005. Structure and mechanics of healing myocardial infarcts. Annu Rev Biomed Eng 7, 223–253.

Honjo, Y., Hasegawa, H., Kanai, H., 2010. Two-Dimensional Tracking of Heart Wall for Detailed Analysis of Heart Function at High Temporal and Spatial Resolutions. Japanese Journal of Applied Physics 49.

Hooks, D.A., LeGrice, I.J., Harvey, J.D., Smaill, B.H., 2001. Intramural multisite recording of transmembrane potential in the heart. Biophys. J 81, 2671–2680.

Hsing, J.M., Selzman, K.A., Leclercq, C., Pires, L.A., McLaughlin, M.G., McRae, S.E., Peterson, B.J., Zimetbaum, P.J., 2011. Paced Left Ventricular QRS Width and ECG Parameters Predict Outcomes After Cardiac Resynchronization TherapyClinical Perspective PROSPECT-ECG Substudy. Circ Arrhythm Electrophysiol 4, 851–857.

Hunter, P.J., Smaill, B.H., 1988. The analysis of cardiac function: A continuum approach. Progress in Biophysics and Molecular Biology 52, 101–164.

Jie, X., Gurev, V., Trayanova, N., 2010. Mechanisms of Mechanically Induced Spontaneous Arrhythmias in Acute Regional Ischemia. Circ Res 106, 185–192.

Kallel, F., Ophir, J., 1997. A least-squares strain estimator for elastography. Ultrason Imaging 19, 195–208.

Kanai, H., 2009. Propagation of Vibration Caused by Electrical Excitation in the Normal Human Heart. Ultrasound in Medicine & Biology 35, 936–948.

Kanai, H., Satoh, H., Hirose, K., Chubachi, N., 1993. A new method for measuring small local vibrations in the heart using ultrasound. Biomedical Engineering, IEEE Transactions on 40, 1233–1242.

Kay, M.W., Amison, P.M., Rogers, J.M., 2004. Three-dimensional surface reconstruction and panoramic optical mapping of large hearts. IEEE Trans Biomed Eng 51, 1219–1229.

Kimber, S., Downar, E., Masse, S., Sevaptsidis, E., Chen, T., Mickleborough, L., Parsons, I., 1996. A Comparison of Unipolar and Bipolar Electrodes During Cardiac Mapping Studies. Pacing Clin Electro 19, 1196–1204.

Koch, W., 1909. Weitere Mitteilungen über den Sinusknoten des Herzens. Verhandlungen der Dt. Pathologischen Anatomie 13, 85–92.

Kojodjojo, P., Kanagaratnam, P., Markides, V., Davies, D.W., Peters, N., 2006. Age-related

changes in human left and right atrial conduction. J. Cardiovasc. Electrophysiol. 17, 120–127.

Kong, W., Ideker, R.E., Fast, V.G., 2009. Transmural optical measurements of Vm dynamics during long-duration ventricular fibrillation in canine hearts. Heart Rhythm 6, 796–802.

Konofagou, E., Lee, W.-N., Luo, J., Provost, J., Vappou, J., 2011. Physiologic Cardiovascular Strain and Intrinsic Wave Imaging. Annu. Rev. Biomed. Eng. 13, 477–505.

Konofagou, E., Ophir, J., 1998. A new elastographic method for estimation and imaging of lateral displacements, lateral strains, corrected axial strains and Poisson's ratios in tissues. Ultrasound Med Biol 24, 1183–1199.

Konofagou, E., Provost, J., 2011. Evolving concepts in measuring ventricular strain in canine and human hearts: non-invasive imaging, in: Cardiac Mechano-Electric Coupling and Arrhythmias. Oxford University Press, Oxford.

Konofagou, E.E., D'hooge, J., Ophir, J., 2002. Myocardial elastography--a feasibility study in vivo. Ultrasound in Medicine & Biology 28, 475–482.

Konofagou, E.E., Luo, J., Saluja, D., Cervantes, D.O., Coromilas, J., Fujikura, K., 2010. Noninvasive electromechanical wave imaging and conduction-relevant velocity estimation in vivo. Ultrasonics 50, 208–215.

Konofagou, E.E., Provost, J., 2012. Electromechanical wave imaging for noninvasive mapping of the 3D electrical activation sequence in canines and humans in vivo. Journal of Biomechanics 45, 856–864.

Lee, W.-N., Ingrassia, C.M., Fung-Kee-Fung, S.D., Costa, K.D., Holmes, J.W., Konofagou, E.E., 2007. Theoretical Quality Assessment of Myocardial Elastography with In Vivo Validation. Ultrasonics, Ferroelectrics and Frequency Control, IEEE Transactions on 54, 2233–2245.

Lee, W.-N., Pernot, M., Couade, M., Messas, E., Bruneval, P., Bel, A., Hagege, A.A., Fink, M., Tanter, M., 2012. Mapping Myocardial Fiber Orientation Using Echocardiography-Based Shear Wave Imaging. Medical Imaging, IEEE Transactions on 31, 554 –562.

Lee, W.-N., Provost, J., Fujikura, K., Wang, J., Konofagou, E.E., 2011. In vivo study of myocardial elastography under graded ischemia conditions. Phys Med Biol 56, 1155–1172.

Liu, Z., Kastis, G.A., Stevenson, G.D., Barrett, H.H., Furenlid, L.R., Kupinski, M.A., Patton, D.D., Wilson, D.W., 2002. Quantitative Analysis of Acute Myocardial Infarct in Rat Hearts with Ischemia-Reperfusion Using a High-Resolution Stationary SPECT System. J Nucl Med 43, 933–939.

Luna, A.B. de, 2011. Clinical Arrhythmology.

Luo, J., Bai, J., He, P., Ying, K., 2004. Axial strain calculation using a low-pass digital differentiator in ultrasound elastography. IEEE Trans Ultrason Ferroelectr Freq Control 51, 1119–1127.

Luo, J., Konofagou, E., 2010. A fast normalized cross-correlation calculation method for motion estimation. IEEE Trans Ultrason Ferroelectr Freq Control 57, 1347–1357.

Luo, J., Konofagou, E.E., 2008. High-frame rate, full-view myocardial elastography with automated contour tracking in murine left ventricles in vivo. Ultrasonics, Ferroelectrics and Frequency Control, IEEE Transactions on 55, 240–248.

Lux, R.L., 2008. Noninvasive Assessment of Cardiac Electrophysiology for Predicting Arrhythmogenic Risk: Are We Getting Closer? Circulation 118, 899–900.

Madore, B., White, P.J., Thomenius, K., Clement, G.T., 2009. Accelerated focused ultrasound

imaging. IEEE Trans Ultrason Ferroelectr Freq Control 56, 2612–2623.

Messinger-Rapport, B.J., Rudy, Y., 1989. Computational issues of importance to the inverse recovery of epicardial potentials in a realistic heart-torso geometry. Mathematical Biosciences 97, 85–120.

Meunier, J., Bertrand, M., 1995. Ultrasonic texture motion analysis: theory and simulation. IEEE Trans Med Imaging 14, 293–300.

Misaridis, T., Jensen, J.A., 2005. Use of modulated excitation signals in medical ultrasound. Part III: high frame rate imaging. Ultrasonics, Ferroelectrics and Frequency Control, IEEE Transactions on 52, 208–219.

Modre, R., Tilg, B., Fischer, G., Hanser, F., Messnarz, B., Seger, M., Schocke, M.F.H., Berger, T., Hintringer, F., Roithinger, F.X., 2003. Atrial Noninvasive Activation Mapping of Paced Rhythm Data. Journal of Cardiovascular Electrophysiology 14, 712–719.

Montaldo, G., Tanter, M., Bercoff, J., Benech, N., Fink, M., 2009. Coherent plane-wave compounding for very high frame rate ultrasonography and transient elastography. IEEE Trans Ultrason Ferroelectr Freq Control 56, 489–506.

Mosterd, A., Hoes, A.W., De Bruyne, M.C., Deckers, J.W., Linker, D.T., Hofman, A., Grobbee, D.E., 1999. Prevalence of Heart Failure and Left Ventricular Dysfunction in the General Population; The Rotterdam Study. Eur Heart J 20, 447–455.

Nash, M.P., Pullan, A.J., 2005. Challenges Facing Validation of Noninvasive Electrical Imaging of the Heart. The Annals of Noninvasive Electrocardiology 10, 73–82.

Noble, D., 1960. Cardiac Action and Pacemaker Potentials based on the Hodgkin-Huxley Equations. , Published online: 05 November 1960; | doi:10.1038/188495b0 188, 495–497.

O'Donnell, M., Skovoroda, A.R., Shapo, B.M., Emelianov, S.Y., 1994. Internal displacement and strain imaging using ultrasonic speckle tracking. Ultrasonics, Ferroelectrics and Frequency Control, IEEE Transactions on 41, 314–325.

Olshansky, B., 2011. Electrocardiographic imaging: Back to the drawing board? Heart Rhythm 8, 700–701.

Ophir, J., Céspedes, I., Ponnekanti, H., Yazdi, Y., Li, X., 1991. Elastography: a quantitative method for imaging the elasticity of biological tissues. Ultrason Imaging 13, 111–134.

Osman, N.F., Kerwin, W.S., McVeigh, E.R., Prince, J.L., 1999. Cardiac motion tracking using CINE harmonic phase (HARP) magnetic resonance imaging. Magnetic Resonance in Medicine 42, 1048–1060.

Otsuji, Y., Handschumacher, M.D., Schwammenthal, E., Jiang, L., Song, J.-K., Guerrero, J.L., Vlahakes, G.J., Levine, R.A., 1997. Insights From Three-Dimensional Echocardiography Into the Mechanism of Functional Mitral Regurgitation : Direct In Vivo Demonstration of Altered Leaflet Tethering Geometry. Circulation 96, 1999–2008.

Pai, V., Axel, L., 2006. Advances in MRI tagging techniques for determining regional myocardial strain. Current Cardiology Reports 8, 53–58.

Parker, K.J., Huang, S.R., Musulin, R.A., Lerner, R.M., 1990. Tissue response to mechanical vibrations for "sonoelasticity imaging". Ultrasound Med Biol 16, 241–246.

Pernot, M., Couade, M., Mateo, P., Crozatier, B., Fischmeister, R., Tanter, M., 2011. Real-time assessment of myocardial contractility using shear wave imaging. Journal of the American College of Cardiology 58, 65–72.

Pernot, M., Fujikura, K., Fung-Kee-Fung, S.D., Konofagou, E.E., 2007. ECG-gated, Mechanical and Electromechanical Wave Imaging of Cardiovascular Tissues In Vivo. Ultrasound in Medicine & Biology 33, 1075–1085.

Pernot, M., Konofagou, E.E., 2005. Electromechanical imaging of the myocardium at normal and pathological states, in: Ultrasonics Symposium, 2005 IEEE. Presented at the Ultrasonics Symposium, 2005 IEEE, pp. 1091–1094.

Ponti, R., Ho, S.Y., Salerno-uriarte, J.A., Tritto, M., Spadacini, G., 2002. Electroanatomic Analysis of Sinus Impulse Propagation in Normal Human Atria. Journal of Cardiovascular Electrophysiology 13, 1–10.

Prinzen, F.W., Augustijn, C.H., Allessie, M.A., Arts, T., Delhass, T., Reneman, R.S., 1992. The time sequence of electrical and mechanical activation during spontaneous beating and ectopic stimulation. Eur Heart J 13, 535–543.

Provost, J., Gurev, V., Trayanova, N., Konofagou, E.E., 2011. Mapping of cardiac electrical activation with electromechanical wave imaging: An in silico-in vivo reciprocity study. Heart Rhythm 8, 752–759.

Provost, J., Lee, W.-N., Fujikura, K., Konofagou, E.E., 2010. Electromechanical Wave Imaging of Normal and Ischemic Hearts in Vivo. IEEE Trans. Med. Imaging 29, 625–635.

Provost, J., Lee, W.-N., Fujikura, K., Konofagou, E.E., 2011a. Imaging the electromechanical activity of the heart in vivo. Proceedings of the National Academy of Sciences 108, 8565–8570.

Provost, J., Lee, W.-N., Fujikura, K., Konofagou, E.E., 2011b. Abstract 21142: Electromechanical Wave Imaging for Noninvasive Mapping of the 3D Electrical Activation Sequence in vivo. Circulation 122, A21142.

Provost, J., Nguyen, V.T.-H., Legrand, D., Okrasinski, S., Costet, A., Gambhir, A., Garan, H., Konofagou, E.E., 2011. Electromechanical wave imaging for arrhythmias. Physics in Medicine and Biology 56, L1–L11.

Provost, J., Thiébaut, S., Luo, J., Konofagou, E.E., 2012. Single-Heartbeat Electromechanical Wave Imaging with Optimal Strain Estimation Using Temporally-Unequispaced Acquisition Sequences. Physics in Medicine and Biology 57, 1095–1112.

Qu, F., Ripplinger, C.M., Nikolski, V.P., Grimm, C., Efimov, I.R., 2007. Three-dimensional panoramic imaging of cardiac arrhythmias in rabbit heart. J Biomed Opt 12, 044019.

Ramanathan, C., Ghanem, R.N., Jia, P., Ryu, K., Rudy, Y., 2004. Noninvasive electrocardiographic imaging for cardiac electrophysiology and arrhythmia. Nat Med 10, 422–428.

Ramanathan, C., Jia, P., Ghanem, R., Ryu, K., Rudy, Y., 2006. Activation and repolarization of the normal human heart under complete physiological conditions. Proceedings of the National Academy of Sciences 103, 6309 –6314.

Remme, E.W., Lyseggen, E., Helle-Valle, T., Opdahl, A., Pettersen, E., Vartdal, T., Ragnarsson, A., Ljosland, M., Ihlen, H., Edvardsen, T., Smiseth, O.A., 2008. Mechanisms of Preejection and Postejection Velocity Spikes in Left Ventricular Myocardium: Interaction Between Wall Deformation and Valve Events. Circulation 118, 373–380.

Ripplinger, C.M., Lou, Q., Li, W., Hadley, J., Efimov, I.R., 2009. Panoramic imaging reveals basic mechanisms of induction and termination of ventricular tachycardia in rabbit heart with chronic infarction: implications for low-voltage cardioversion. Heart Rhythm 6, 87–97.

Roger, V.L., Go, A.S., Lloyd-Jones, D.M., Adams, R.J., Berry, J.D., Brown, T.M., Carnethon, M.R.,

Dai, S., de Simone, G., Ford, E.S., Fox, C.S., Fullerton, H.J., Gillespie, C., Greenlund, K.J., Hailpern, S.M., Heit, J.A., Ho, P.M., Howard, V.J., Kissela, B.M., Kittner, S.J., Lackland, D.T., Lichtman, J.H., Lisabeth, L.D., Makuc, D.M., Marcus, G.M., Marelli, A., Matchar, D.B., McDermott, M.M., Meigs, J.B., Moy, C.S., Mozaffarian, D., Mussolino, M.E., Nichol, G., Paynter, N.P., Rosamond, W.D., Sorlie, P.D., Stafford, R.S., Turan, T.N., Turner, M.B., Wong, N.D., Wylie-Rosett, J., 2011. Heart disease and stroke statistics--2011 update: a report from the American Heart Association. Circulation 123, e18–e209.

Rudy, Y., Burnes, J.E., 1999. Noninvasive Electrocardiographic Imaging. Ann Noninv Electrocard 4, 340–359.

Sacher, F., Roberts-Thomson, K., Maury, P., Tedrow, U., Nault, I., Steven, D., Hocini, M., Koplan, B., Leroux, L., Derval, N., Seiler, J., Wright, M.J., Epstein, L., Haissaguerre, M., Jais, P., Stevenson, W.G., 2010. Epicardial Ventricular Tachycardia Ablation: A Multicenter Safety Study. J Am Coll Cardiol 55, 2366–2372.

Sachse, F.B., 2004. Computational Cardiology: Modeling Of Anatomy, Electrophysiology, And Mechanics. Springer.

Sanders, P., Berenfeld, O., Hocini, M., Jaïs, P., Vaidyanathan, R., Hsu, L.-F., Garrigue, S., Takahashi, Y., Rotter, M., Sacher, F., Scavée, C., Ploutz-Snyder, R., Jalife, J., Haïssaguerre, M., 2005. Spectral analysis identifies sites of high-frequency activity maintaining atrial fibrillation in humans. Circulation 112, 789–797.

Scher, A.M., Young, A.C., 1956. The pathway of ventricular depolarization in the dog. Circ Res 4, 461–9.

Schilling, R.J., Peters, N.S., Davies, D.W., 1998. Simultaneous endocardial mapping in the human left ventricle using a noncontact catheter: comparison of contact and reconstructed electrograms during sinus rhythm. Circulation 98, 887–98.

Sengupta, P.P., Khandheria, B.K., Korinek, J., Jahangir, A., Yoshifuku, S., Milosevic, I., Belohlavek, M., 2007. Left ventricular isovolumic flow sequence during sinus and paced rhythms: new insights from use of high-resolution Doppler and ultrasonic digital particle imaging velocimetry. J. Am. Coll. Cardiol 49, 899–908.

Sengupta, P.P., Tondato, F., Khandheria, B.K., Belohlavek, M., Jahangir, A., 2008. Electromechanical activation sequence in normal heart. Heart Fail Clin 4, 303–14.

Sevaptsidis, E., Massé, S., Parson, I.D., Downar, E., Kimber, S., 1992. Simultaneous unipolar and bipolar recording of cardiac electrical activity. Pacing Clin Electrophysiol 15, 45–51.

Shah, D., Haïssaguerre, M., Jaïs, P., Takahashi, A., Hocini, M., Clémenty, J., 1999. High-Density Mapping of Activation Through an Incomplete Isthmus Ablation Line. Circulation 99, 211–215.

Shattuck, D.P., Weinshenker, M.D., Smith, S.W., von Ramm, O.T., 1984. Explososcan: a parallel processing technique for high speed ultrasound imaging with linear phased arrays. J. Acoust. Soc. Am 75, 1273–1282.

Shehata, M., Cheng, S., Osman, N., Bluemke, D., Lima, J., 2009. Myocardial tissue tagging with cardiovascular magnetic resonance. Journal of Cardiovascular Magnetic Resonance 11, 55.

Sicari, R., Nihoyannopoulos, P., Evangelista, A., Kasprzak, J., Lancellotti, P., Poldermans, D., Voigt, J.-U., Zamorano, J.L., 2008. Stress echocardiography expert consensus statement: European Association of Echocardiography (EAE) (a registered branch of the ESC). Eur J

Echocardiogr 9, 415–437.

Støylen, A., Slørdahl, S., Skjelvan, G.K., Heimdal, A., Skjaerpe, T., 2001. Strain rate imaging in normal and reduced diastolic function: Comparison with pulsed Doppler tissue imaging of the mitral annulus. Journal of the American Society of Echocardiography 14, 264–274.

Sutherland, D.R., Ni, Q., MacLeod, R.S., Lux, R.L., Punske, B.B., 2008. Experimental measures of ventricular activation and synchrony. Pacing Clin Electrophysiol 31, 1560–1570.

Taccardi, B., Arisi, G., Macchi, E., Baruffi, S., Spaggiari, S., 1987. A new intracavitary probe for detecting the site of origin of ectopic ventricular beats during one cardiac cycle. Circulation 75, 272–281.

Tai, C.-T., Liu, T.-Y., Lee, P.-C., Lin, Y.-J., Chang, M.-S., Chen, S.-A., 2004. Non-contact mapping to guide radiofrequency ablation of atypical right atrial flutter. J. Am. Coll. Cardiol 44, 1080–1086.

Tanter, M., Bercoff, J., Sandrin, L., Fink, M., 2002. Ultrafast compound imaging for 2-D motion vector estimation: application to transient elastography. IEEE Transactions on Ultrasonics, Ferroelectrics and Frequency Control 49, 1363–1374.

Tawara, S., 1906. Das Reizleitungssystem des Säugetierherzens. Fischer.

Turcott, R.G., Witteles, R.M., Wang, P.J., Vagelos, R.H., Fowler, M.B., Ashley, E.A., 2010. Measurement Precision in the Optimization of Cardiac Resynchronization TherapyClinical Perspective. Circ Heart Fail 3, 395–404.

Varghese, T., Ophir, J., 1997. A theoretical framework for performance characterization of elastography: the strain filter. IEEE Trans Ultrason Ferroelectr Freq Control 44, 164–172.

Vassallo, J.A., Cassidy, D.M., Marchlinski, F.E., Buxton, A.E., Waxman, H.L., Doherty, J.U., Josephson, M.E., 1984. Endocardial activation of left bundle branch block. Circulation 69, 914–923.

Vatner, S.F., 1980. Correlation between acute reductions in myocardial blood flow and function in conscious dogs. Circ Res 47, 201–7.

Villarreal, F.J., Lew, W.Y., Waldman, L.K., Covell, J.W., 1991. Transmural myocardial deformation in the ischemic canine left ventricle. Circ Res 68, 368–81.

Waldman, L., Fung, Y., Covell, J., 1985. Transmural myocardial deformation in the canine left ventricle. Normal in vivo three-dimensional finite strains. Circ Res 57, 152–163.

Walker, W.F., Trahey, G.E., 1994. A fundamental limit on the performance of correlation based phase correction and flow estimation techniques. Ultrasonics, Ferroelectrics and Frequency Control, IEEE Transactions on 41, 644–654.

Wang, S., Lee, W.-N., Provost, J., Luo, J., Konofagou, E.E., 2008. A composite high-frame-rate system for clinical cardiovascular imaging. Ultrasonics, Ferroelectrics and Frequency Control, IEEE Transactions on 55, 2221–2233.

Wang, Y., Schuessler, R.B., Damiano, R.J., Woodard, P.K., Rudy, Y., 2007. Noninvasive electrocardiographic imaging (ECGI) of scar-related atypical atrial flutter. Heart Rhythm 4, 1565–1567.

Weinstein, E., Weiss, A., 1984. Fundamental limitations in passive time-delay estimation--Part II: Wide-band systems. Acoustics, Speech and Signal Processing, IEEE Transactions on 32, 1064–1078.

Wolf, P., Abbott, R., Kannel, W., 1991. Atrial fibrillation as an independent risk factor for stroke: the Framingham Study. Stroke 22, 983 –988.

Wright, J., 1997. Image formation in diagnostic ultrasound. Presented at the IEEE International Ultrasonic Symposium.

Wyman, B.T., Hunter, W.C., Prinzen, F.W., McVeigh, E.R., 1999. Mapping propagation of mechanical activation in the paced heart with MRI tagging. Am J Physiol Heart Circ Physiol 276, H881–891.

Zhang, X., Ramachandra, I., Liu, Z., Muneer, B., Pogwizd, S.M., He, B., 2005. Noninvasive three-dimensional electrocardiographic imaging of ventricular activation sequence. Am J Physiol Heart Circ Physiol 289, H2724–32.

Zheng, Z.-J., Croft, J.B., Giles, W.H., Mensah, G.A., 2001. Sudden Cardiac Death in the United States, 1989 to 1998. Circulation 104, 2158 –2163.

Zlochiver, S., 2011. Ultrasonic measurements of local activation times: toward the realization of a clinical intramural cardiac electrical mapping? Heart Rhythm 8, 760–761.

Zwanenburg, J.J.M., Gotte, M.J.W., Kuijer, J.P.A., Heethaar, R.M., van Rossum, A.C., Marcus, J.T., 2004. Timing of cardiac contraction in humans mapped by high-temporal-resolution MRI tagging: early onset and late peak of shortening in lateral wall. Am J Physiol Heart Circ Physiol 286, H1872–1880.